Coherent Association of Single Molecules from Single Atoms

A DISSERTATION PRESENTED
BY
YICHAO YU
TO
THE DEPARTMENT OF PHYSICS

IN PARTIAL FULFILLMENT OF THE REQUIREMENTS
FOR THE DEGREE OF
DOCTOR OF PHILOSOPHY
IN THE SUBJECT OF
PHYSICS

HARVARD UNIVERSITY
CAMBRIDGE, MASSACHUSETTS
MARCH 2021

Thesis advisor: Professor Kang-Kuen Ni   Yichao Yu

Coherent Association of Single Molecules from Single Atoms

ABSTRACT

Neutral molecules, with their rich spectrum of internal states as well as strong and tunable dipolar interactions, are promising candidates for a broad range of experiments including quantum information, quantum chemistry, precision measurement and probing of beyond-Standard-Model physics, and quantum simulation of interacting many-body systems. At the same time, the complexity that made them attractive also poses a significant challenge to achieve a high level of quantum control that is required in many of their potential applications. Multiple approaches are being pursued for full quantum control of molecules including association of atomic gases and direct cooling of molecules, yet it remains challenging to control molecules at single particle level due to the difficulty in tuning the atom-atom interaction and laser cooling of molecules.

In this thesis, we successfully achieved coherent association of weakly bound ground state molecules. By combining the mature techniques for quantum control of atoms and the resolution and flexibility of optical tweezers, we developed a versatile platform to study interactions between single atoms and properties of single molecules. Based on these study, we proposed a promising pathway for coherent all-optical creation of molecules and demostrated full control on the molecule including all degrees of freedoms.

Contents

Listing of figures

Acknowledgments

,

0

Introduction

0.1 ULTRACOLD MOLECULES

Started with precise optical spectroscopy and the development of laser cooling and trapping tech-

nologies, the increasing measurement precision and high level of control has been one of the the

primary driving forces in the field of atomic physics in the past decades. Systems based on cooling

and controlling of neutral atoms have been used in a wide range of applications including quantum

computing, quantum communication, precision measurement, quantum simulation and the study of many other many body effects.

Despite these great successes, the utility of atom based systems are limited by their simple internal structure and weak interactions. Molecules, on the other hand, with its richer internal degrees of freedom including electronic orbital, electron spin, neuclear vibration, rotation and spin, the potential of stronger interaction and more variance of symmetry classes, are better candidates for more applications especially in quantum computing, precision measurement and quantum simulation. Moreover, comparing to other systems with stronger interaction like ions and Rydberg atoms, the interacting states in molecules are long lived and tunable thanks to the abundance of low energy excitations, which can offer better isolation from the environment giving rise to longer coherence time.

Many applications of molecules requires cooling and high level of control on the quantum state of the molecules. Unfortunately, the properties that makes molecules attractive also makes controlling them harder. The enabling technique for most ultracold atom experiment, laser cooling, typically requires scattering of a large number of photons ($\approx 10^4 \sim 10^7$). This is possible in atomic system due to the existence of cycling transition or near cycling ones that can be completely closed with one or two spin states repumping lasers. However, the lack of selection rules for vibrational states means that such transition generally does not exist in molecules. As a result, experiments aiming to achieve control of molecule on a similar level with atoms usually take one of the two approaches,

1. Direct laser cooling of special molecules with approximate cycling transitions. These are molecules that have optical transitions that has a high probability of decaying down to the same vibrational states. With the help of a few vibrational repumping lasers,

scattering of $\approx 10^3 \sim 10^5$ photons can be achieved. Significant progress has been made using this approach in recent years including sub-doppler cooling and trapping of molecules in optical tweezers. The main challenge with this approach is to achieve a better cooling performance given the still limitted photon scattering budget.

2. Creating of molecules from ultracold atoms.
   First realized a decade ago[1], this approach takes advantage of the mature cooling and trapping techniques developped for atoms and creates molecules from atoms that are cooled to ultracold temperature. The difficulty with this approach is understandably in the creation of the molecule, which must be done with acceptable efficiency and coherence in order to maintain the cooling and controling done on the atoms. This approach currently allows a lower temperature to be achieved and this is the approach used in our experiment.

0.2 ASSEMBLY OF MOLECULES IN OPTICAL TWEEZERS

Previous experiments that takes the approach to create ultracold molecules from ultracold atoms do so either in a bulk gases or an optical lattice. In these systems, however, the transfer efficiency and the density of the created molecules are limited by the overlap between the distribution of the two atomic speices. Such overlap is controlled by the combination of the trapping potential and the intra- and inter-species interactions. Thus, a perfect overlap for molecule formation can only be achieved by fine tuning the delicate balance between these parameters and may not always be possible. Additionally, the molecules created in such matter may collide with residue atoms or other molecules causing rapid loss either through chemical reactions or by forming long-lived sticky complex.

Since these issues are essentially all caused by the lack of direct control on the position and mo-

tion of individual atoms and molecules, we propose a general solution using optical tweezers. Created by focusing the trap light through a high numerical aperture (NA) objective, optical tweezers can trap single atoms in flexible geometry and the setup naturally provides the high resolution required for detection and manipulation of individual atoms. Taking advantage of these properties, full quantum control on atoms has been demostrated by cooling and rearranging the tweezer based on the loading result. This gives us a good starting point to deterministically create molecules by directly merging pairs of atoms instead of relying on stochastic process or the fine tuning of parameters in previous experiments. The molecules created using this approach are also well isolated from each other, preventing loss due to collisions.

0.2.1 TWO-STEP ALL OPTICAL CREATION OF MOLECULES

In order to create the rovibronic ground state molecules from atoms, the $\approx$ 100 THz binding energy must be removed coherently from the system, which is may be done using a two-photon optical transition. However, due to the significant mismatch in the wavefunction size between the atomic motional ground state ($\approx$ 1000Å) and the rovibronic ground state of the molecule ($\approx$ 4Å), it is challenging to achieve a high Rabi frequency or short transition time, causing technical difficulties in maintaining the laser coherence during the transition. Because of this, the transfer to rovibronic ground state is typically done in two steps. The atoms are first associated to a weakly bound molecule where the coherence is easier to achieve due to the smaller energy difference. After that the molecule can be driven to the rovibronic ground state more quickly, relaxing the coherence requirement.

So far, most experiments implemented the first step by magnetoassociation using a magnetic Feshbach scattering resonance. The only exceptions are Sr_2, where narrow-linewidth ($\sim$ 20 kHz) excited states are available and optical association can be driven coherently and $^{87}Rb^{85}Rb$, where there are molecular states bound by 1 $\sim$ 2 MHz. With these requirements, molecules involving non-magnetic atoms or atoms without narrow intercombination lines remain difficult to associate.

In our experiment, we propose a different method using only optical transitions and does not rely on an narrow excited state linewidth. This is enabled by the confinement of the optical tweezer and careful selection of the transition pathway, which will be covered in more detail in later chapters. We believe the approach we demostrate in our experiment is more general than the previous ones, and can be applied to most other molecules created from laser-coolable atoms.

0.2.2 EXPERIMENT PLAN

The molecule we use to implement this approach is NaCs. We selected a bialkali molecule in order to take advantage of the wide range of existing techniques developped to cool and manipulate alkali atoms. The molecule is also predicted to have a large molecular fixed-frame dipole moments (4.6 Debye) in the singlet rovibronic ground state, making it a good candidate to demostrate interaction and entanglement after created in the tweezers.

The steps we propose to create the molecules in the tweezer are as follows,

1. Loading and cooling of single atoms in the tweezers.
   This is the step that give us the full quantum control on the atoms which will be translated to the control on the molecules later. Image of the atoms taken in this step can be used to rearrange the tweezers to acheive high filling fraction.

2. Merging of the atoms into a single tweezer.

    Using the precise control of the atoms from optical tweezers, we can merge a single Na and Cs that is trapped and cooled in separate tweezers into a single one deterministically.

3. Creation of weakly bound molecule.

    The pair of atoms in a single tweezer will be coherently associated to a weakly bound molecule using a Raman transition detuned from an excited molecular state. This is the critical step that transfers the control we achieved on the atoms to molecules and will be the main result of this thesis.

4. Creation of rovibronic ground state molecule.

    Finally, the weakly bound molecule will be driven to the rovibronic ground state using another two-photon transition. This prepare the molecule in a state with strong dipole interaction and can be used for many previously mentioned applications.

0.3   Contents of this Thesis

In this thesis, we describe the method we use to create a weakly bound ground state molecule in the optical tweezer and the results leading up to it including the control of atoms and the measurement on the interaction between the atoms and the molecular potential.

We start with chapter 1 by giving a high level description of the custom computer control system we use. This system controls the timing of all the hardware outputs in the experiment and is used to perform all the measurements in the rest of this thesis.

Chapter 2 discusses the loading of the single atoms into the optical tweezer. The discussion includes the preparation steps needed before the loading, e.g. freespace cooling of atoms, and the imaging of the atom in the tweezer, which is the primary detection method used in our experiment. All

the experiments in the following chapters are performed using the atoms and molecules in the optical tweezers.

Chapter 3 describes the Raman sideband cooling (RSC) process we used to cool single Na atom in the optical tweezer. As the lighter atom with a broader optical linewidth, the RSC of Na atom faces additional challenges compared to atoms that were cooled using similar method previously and the tool we developed to overcome these challenges can be applied to other systems as well.

After preparation of the atomic state, chapter 4 starts our investigation of the interaction between atoms by measuring the s-wave scattering length using interaction shift spectroscopy. The measurement result is used to refine the prediction for Feshbach resonance between Na and Cs atoms and also to improve the atomic state preparation.

Chapter 5 discusses the measurement of the molecular excited states by photoassociation spectroscopy. We also study the effect of the tweezer beam on the molecular states and transitions. The states mapped out in this measurement are used as intermediate states to study the groud molecular states via two-photon transitions.

Following the previous chapter, chapter 6 discusses the properties of the weakly bound ground molecular states using Raman spectroscopy. We demostrated the ability to control the rotational states of the molecule and studies the coupling of the molecule with external field and the their hyperfine structure in the weakly bound regime. The measurement identifies candidate target states for our coherent molecule creation.

Chapter 7 combines the preparation and characterization in the previous chapters and describes our all-optical coherent molecule formation process. A detailed comparison between different ap-

proaches and states selection is given to support our choice of experimental parameters. We show our result on the coherent transfer and characterizes the molecule we create as well as the transfer process. We study the limit on the transfer efficiency and list open questions in the transfer process as well as possible future improvements.

1

Computer Control of the Experiment

1.1   Introduction

The experiment sequence and data taking is managed by computers. In additional to controlling

the timing and the actions during a sequence, the computer control system is also the main interface

between the people running the experiment (the user), the data and the hardware performing the

manipulation and measurements. Because of its central role in the experiment, it has to satisfy many

requirements so that the daily operation of the lab can be performed smoothly and reliably.

1. Full control and utilization of hardware.
   The control system is a layer in between the the user and the hardware and will abstract and manage the hardware on behave of the user. However, the abstraction must still allow the user to take advantage of the full capability of the hardware, e.g. output resolution, timing accuracy etc.. This is because there is usually little margin between the capability of the hardware and the requirement in the experiment as the specification of the hardware is often selected based on the requirement to begin with.

2. Usability for all lab members.
   The lab is operated by users with specialty in physics rather than computer science. Although some basic knowledge of computer programming is required for operating the experiment as well as analysing data, the computer control system must be fully usable for people without any experience in building complex software systems.
   The inevitable complexity of the system must be fully hidden from the user for normal operations although more direct control may still be allowed in certain cases.

3. Modeling of the sequence and scan.
   As an important special case of usability, the computer control system must provide a model for each tasks closed to the users' mental model. More concretely, this means creating abstraction for concepts typically used to describe the task and allow operation on these abstractions matching the users' expectation. We will talk about concrete examples of this requirements in section 1.2 regarding the sequence frontend and section 1.4 regarding scan automation.

4. Reproducibility.
   When exploring something new in the experiment, trial and error is the standard method and troubleshooting is a major part of the process. The ability to do this effectively requires a high degree of reproducibility of all the result. While it is impossible and also not the job of the computer control system to eliminate all the fluctuation and noise in the experiment, it should not add to the randomness of the system. With few exceptions, identical user input should produce identical output from the control system.

5. Version control.
   As a variation of the reproducibility requirement and also built on top of it, we must be able to revert to a previous software configuration at a later time in order to reproduce and

double-check an earlier result. The use of a proper version control system on the settings and code for the computer control system can allow this with additional features including easy visualization of setting change and parallel development of code by multiple users.

The design of the computer control system is mainly guided by these requirements and we will go into more detail as we describe each part of the system. The application programming interface (API) provided for sequence and scan programming are mostly text based due to the flexibility and version control requirement. Some graphic user interface (GUI) are also included for specific tasks built on top of the text interface but will not be covered in this chapter. Section 1.2 will cover the frontend of the system which is used by the user directly to specify an experimental sequence. Section 1.3 will discuss the support for various hardware backends used to run a sequence. After that, section 1.4 describes how multiple sequences can be put together to form a scan and we will talk about some planned update to the system in section 1.5.

1.2 FRONTEND

The frontend is the main user interface of the system to specify a sequence. Its API is designed around the a few concepts that can be divided into two categories,

1. Timing

   (a) (Sub-)sequence
   This represent a series of events that has fixed relative timing. Sequences can be nested in other sequences at a specific time offset and are called subsequences. Each sequence can only have at most one parent sequence (the top level one has none) and zero or more subsequences so all the subsequences in a top level sequence forms a tree.

   (b) Time step

The time or time period in the sequence when one or more event may happen is called a time step. Each time step has a length and a position within a unique parent sequence and are always the leaves on the sequence tree.

2. Output

   (a) Channel
   Each device that can generate an output are abstracted into one or multiple channels that each output a single number. The abstraction depends on the type of the device, e.g. voltage value for a digital to analog converter, or frequency and amplitude for an computer-controlled sine-wave generator.

   (b) Pulse
   This represents the actual output for a particular channel. The pulse itself does not contain the timing information within the sequence, i.e. start and end time. Instead, each pulse belongs to a unique time step that specifies the timing.

Operations on concepts in one category are usually independent of the other which allows most common modifications to the sequence to be done with minimum code change, including,

1. Adding/removing/changing the length of time step or subsequences without affecting the relative timing or output in other part of the sequence.

2. Enabling/disabling output or changing output values without changing the time and length of the output.

The sequence programming uses MATLAB as the host language. Despite not the best choice from the feature or performance aspect, it offers the following desired properties,

1. Text based language and therefore easier for version control.

2. Familiarity for physics student.
   MATLAB is often used for simulation and data processing. It is one of the few languages that most new students will be familiar with.

3. Builtin feature-rich integrated development environment (IDE).

4. Foreign function interface (FFI).
   Other parts of the system needs to be implemented in other languages for various reasons including higher performance. It is important that we can call into other languages to allow such a hybrid implementation.

5. Good enough feature set.
   MATLAB provides data structures like arrays and hash table as well as handle classes with object identity which are important to handle the representation of the sequence. It also has an good enough object-oriented programming (OOP) model and operator overloads which can simplify the API syntax for the user.

1.2.1 Channel Naming

Each output channel has a unique name attached for identification. This name is always a string of the format `<device_id>/<channel>` where `<device_id>` is an name for the (physical) device and `<channel>` is an identification of the channel within the device. The `<device_id>` may not contain `/` but other than this neither `<device_id>` nor `<channel>` has globally predefined meaning and are completely up to the backend to define. This format allows maximum freedom for the backend to abstract its function into multiple channels in the most fitting way, while allowing the generic code to identify the device, and therefore backend, needed without fully interpreting the channel name.

Class `TimeSeq`

Methods:

- `setTime(time_point, time_ratio=0, offset=0)`
  Set the time for a `TimeSeq` with unspecified time
  (added with `addFloating`).

Class `ExpSeqBase`

Properties:

- `curTime`
  The time within the sequence where
  the next step will be added by
  "default".

Methods:

- `addStep(<time_params>)`
  Add a step or subsequence at `curTime`
  and forward `curTime`. Returns
  `TimeSeq`.

- `addBackground(<time_params>)`
  Add a step or subsequence at `curTime`
  without forward `curTime`. Returns
  `TimeSeq`.

- `addAt(time_point, <time_params>)`
  Add a step or subsequence at
  `time_point` without updating
  `curTime`. Returns `TimeSeq`.

- `addFloating(<time_params>)`
  Add a step or subsequence at
  unspecified time without updating
  `curTime`. Returns `TimeSeq`.

- `wait(t)`
  Wait for time `t`.

- `waitAll()`
  Wait for all children `TimeSeq` to finish.

- `waitBackground()`
  Wait for all `TimeSeq` added directly via
  `addBackground` to finish.

- `waitFor(seqs, offset=0)`
  Wait for `seqs` to finish.

Class `TimeStep`

Methods:

- `add(channel_name, output)`
  Generate `output` on
  `channel_name`.

Class `TimePoint`

Constructor:

- `TimePoint(seq, time_ratio, offset)`
  Create a `TimePoint` corresponding to a time
  within `seq` (class `TimeSeq`).

Figure 1.1: Frontend class inherit diagram and API lists.

14

1.2.2 APIs

The system provides the following APIs for sequence creation that are subject to strict backward compatibility requirements. The most important APIs are listed in this section. Fig. 1.1 provides a short summary of all the classes and methods mentioned in this section.

1.2.2.1 TIMING

Subsequences are represented by the `ExpSeqBase` class and time steps are represented by the `TimeStep` class. Both `ExpSeqBase` and `TimeStep` are subclasses of `TimeSeq`, which represent an arbitrary node on the sequence tree.

Most timing related APIs are methods on `ExpSeqBase`. The most important ones are the ones creating new branches in the subsequence tree, i.e. `TimeSeq`. The type of the branch created is determined by the parameters passed in (`<time_params>`), which can be either,

1. `length, offset=0`
   This creates a new `TimeStep` with a numerical `length` and an optional time `offset` from a API dependent time reference point (see list of APIs below).

2. `offset=0, callback, <callback parameters>`
   This creates a new `ExpSeqBase` with an optional time `offset` the time reference point. The new subsequence will be populated by calling `callback` with the new sequence followed by `<callback parameters>`.

Since most sequences are built in series, `ExpSeqBase` maintains a current time (`curTime`) of the sequence. Various methods are provided that acts differently with respect to `curTime`.

1. `addStep(<time_params>)` method

This is the most used method to construct the sequence in series. The time reference point is `curTime` and `curTime` will be set to the end of the time step or subsequence created. A check is make sure the `curTime` only moves forward and errors if a too negative `offset` is specified. This ensures that what added with `addStep` always appears in the final sequence in the same order as program execution order which makes the code easier to reason about.

2. `addBackground(<time_params>)` method
   The time reference point is `curTime` and no change to `curTime` is made.

3. `addAt(time_point, <time_params>)` method
   The time reference point is specified by `time_point` which is of type `TimePoint`. See below about `TimePoint`.

4. `addFloating(<time_params>)` method
   The time reference point is unspecified. The optional `offset` parameter cannot be specified in `<time_params>`. The time reference point, however, must be specified before the sequence can run. This can be done by calling the `setTime(time_point, time_ratio=0, offset=0)` method on the `TimeSeq` object returned, where `time_point` is also of type of type `TimePoint` described below. The optional `time_ratio` specifies the relative time within the subsequence or time step to set the time for where a value of 0 set the start time and a value of 1 set the end time.

All methods return the new `TimeSeq` constructed so that they can be operated on.

The `TimePoint` object used in `addAt` and `setTime` can be constructed via `TimePoint(seq, time_ratio, offset)` which represent the time within the sequence or step `seq` with a time `offset`. `time_ratio` specifies the time within the `seq` where 0 is the start time and 1 is the end time.

Additional continence methods for `ExpSeqBase` are also provided to manipulate `curTime`,

1. `wait(t)` method
   Add `t` to `curTime`. This is the only method that can change `curTime` backwards.

2. `waitAll()` method
   Forward `curTime` to the end of all (nested) subsequences and time steps within the current subsequence.

3. `waitBackground()` method
   Similar to `waitAll()` but only wait for the subsequences and time steps directly added to the current subsequence.

4. `waitFor(seqs, offset=0)` method
   Forward `curTime` to the end of subsequences and time steps specified within the array `seqs`. An optional `offset` may be added to the latest end time.

1.2.2.2 OUTPUT

As mentioned before, all the output are specified on time steps which are represented by class `TimeStep`.

This is done via a single method `add(channel_name, output)` on `TimeStep`. The `channel_name`

is the channel name described above and `output` specifies the output in one of the following way,

1. A number
   This represent setting the channel to the specified value at the start time of the pulse.

2. A function or callable object
   The function will be used to compute the value to output over the whole duration of the pulse. It will be called with arguments (`t, len, old_val`) where `t` is the time within the pulse, `len` is the length of the pulse and `old_val` is the previous value of the channel before the current pulse.

1.3 BACKENDS

As discussed in section 1.2, the frontend provides an API to program all the output channels in the

same way no matter the type of the channel or device used. However, this is not the case for the de-

vices generating for the output which often have an API specifically designed for the device that may

be very different from one another. Moreover, the frontend represent the sequence as a tree structure that is convinient for manipulation whereas the device API typically uses a flat data structure like an array of numbers or a series of commands. It is therefore the job of the backend to bridge this gap and convert the between the multiple representations of the sequence. The conversion is done in a "generate" step and the result is cached for each sequence to allow running the sequence multiple times with minimum overhead.

The specific requirements and implementations for each backends are very different. Nevertheless, there are a few important features or components that are shared among different backends.

1.3.1 Network Communication

With one current exception, the output device is not directly connected to the computer running the frontend but is only connected to another computer on the same network. This requires network communication between the frontend machine and a service running on the device computer for running the sequence.

We use ZeroMQ Message Transport Protocol (ZMTP) as the main protocol for network communication which offers the following advantages,

1. Binary protocol
   The protocol allows us to send and recieve arbitrary data without having to encode it in text first. This saves encoding and decoding time as well as network bandwidth which allows higher performance.

2. Feature rich and flexible
   Compared to using sockets for network communication directly, the message oriented protocol allows easy implementation of remote procedure call (RPC). The ZeroMQ library

18

also provides flexible interface to process the messages which is useful to implement robust handling of failure and parallel processing of requests.

3. Light weight
   Despite the rich feature set, the library is relatively light weight. This is important because part of the computer control system need to be executed in environment with limited resources.

4. Cross platform
   The library is cross platform and provide identical API on different environment. Windows support is particularly important since most of the development is done on Linux machines.

5. Stable
   Both the protocol and the library are stable. The library version available on different machines are not always the same and it is important that the same version of code can work on different machines and can communicate with each other in all cases.

1.3.2   Sorting of Pulses

The tree representation of the sequence is useful for construction and manipulation but contains unnecessary information for generating output, for which only the pulses and their start and end time within the top-level sequence is important but not the subsequence structure. Because of this, all the backends starts the generation step by flattening the tree to obtain a list of all pulses sorted by their start time. After the sorting of the pulses, the tree structure is discarded by default [*] to reduce memory usage.

---

[*]This behavior can be disabled for debugging purpose

1.3.3 REPRESENTATION OF PULSES

Several backends require accessing the exact representation of the pulses outside MATLAB code and even on a different computer. Since the pulses can be arbitrary functions, this requires the ability to serialize and deserialize code.

In order to do this, we developed a simple intermediate representation (IR) of code that runs on a register-based virtual machine. The IR supports three different data types, `Bool`, `Int32` and `Float64` and basic arithmetic, control flow and math functions that are sufficient for specifying pulse shapes. The IR can be interpreted by an interpreter written in C++ or be compiled and optimized to native code for faster execution using an LLVM based compiler.

In order to convert MATLAB functions specified in the sequence to the IR, we pass in a special object as the input argument to the MATLAB function. Supported operations on this object will return a new object that records the operation as well as input arguments. The value returned from the function is therefore an object representing all the operations needed to compute the result as a directed acyclic graph (DAG). We then convert each node in the DAG to an IR instruction to finish the convertion. This process only support pure functions. Conditional branch is supported via an `ifelse` function that returnes one of the input argument based on an condition. Loops are not currently supported.

Figure 1.2: FPGA hardware block diagram. The sequence data is sent to the server program running on the CPU via network. The program then push the commands to the pulse controller implemented in the programming logics. The pulse controller executes the commands and genenerates or changes outputs for clock/trigger, DDS or logical outputs.

The timing of the experiment is controlled by a Xilinx ZC702 FPGA which contains both a processing system (PS) part, i.e. CPU, and a programmable logic (PL) part, i.e. FPGA (Fig. 1.2). The PL creates digital control signals for various peripheral devices which generate output for the experiment, including direct digital synthesizers (DDS), logical switching signal and clock or trigger signal for other devices. The PS consists of a dual core Cortex-A9 CPU which runs an Arch Linux ARMv7 distribution. The server software that runs on the PS communicates with the main control computer via ZeroMQ (section 1.3.1) and generates a custom command stream to control the PL output. Each command corresponds to making one change to the final output, e.g. logical values, DDS output amplitude or frequencies, etc. The main job of the FPGA backend is therefore to convert the sorted pulses to the command stream.

Due to performance concern, this conversion is done in C++ code[*]. The main design considerations and features are,

1. The sequence supports changing and ramping multiple channels at the same time. This is not supported by the hardware due to the limit on the number of I/O ports connecting the PL to the output devices requiring multiplexing of the control signal. The backend manages this by interleaving the commands for different channels when more than one are changed at the same time. A set of active pulses are maintained as the conversion proceed through sequence time. Pulses are added to the active set when the start time is reached and retired from the set when the end time is reached.

2. For a continuous ramp of a channel, since the output changes are discrete, it may not happen at exactly the end time of the pulse which requires special care to ensure the correctness of

---

[*]https://github.com/nacs-lab/libnacs/blob/0076e347ff3ba674fbf74872883b40feefd82ce0/lib/seq/bytecode.cpp#L528

the channel value after a pulse. For example, a linear ramp from 0 to 0.5 on a channel from time 0 μs to 5 μs may only receive update at time 0, 2, 4 μs with values 0.0, 0.2, 0.4 respectively due to discretization. However, the user should expect the value of the channel (absence of other pulses) long after the pulse to be 0.5 instead. This is handled in the backend by checking the last update from the pulse against its expected ending value before retiring it. A final update to the ending value is generated if the two values are different.

3. The output has finite resolution. If an update changes the value that is unresolved by the hardware (typical during a slow ramp), the update will be omitted.

4. Some commands correspond to more than one action/pulse in the sequence. For example, more than one logical outputs can be updated at the same time and some commands also accept a variable wait time afterwards (in additional to a special purpose wait command). The backend examines neighboring operations and may merge multiple commands into one. This is especially useful for logical outputs. In fact, logical outputs changes that is specified to happen at the same time in the sequence are guaranteed to happen at the same time in the experiment as well.

5. The PL commands are fixed length to allow a simpler implementation of command parsing in the PL. However, since not all commands contain the same amount of information, some include padding for alignment. In order to save network bandwidth, a compressed format with variable command length and no padding is used to transfer the commands through the network. The decompression is done when running the sequence on the CPU right before sending to the PL for execution.

1.3.5 NiDAQ Backend

For outputing slowly varying voltage signal, we use an DAQ PCI card. The software driver for the card accepts an array of numbers as the voltages to output at each cycle for each channels. Since the values in these arrays can be computed for each channels independently, the logic for generating is relatively straightforward.

The API for the card is designed for updating the outputs at regular interval. However, there are a few issues when it is used this way,

1. The same sampling rate is used when frequent update to the output is needed and when the output are held at a constant value.
   Since output voltages are usually only being varied for a short time compared to the length of the sequence, this cause significant duplication in the data causing a waste of memory.

2. We measured voltage noice at the refresh rate when the output is held constant by outputting samples at the same value.
   While this is a hardware limit that cannot easily be fixed when the value are changing, being able to turn off the refreshing gives us control to minimize its effect on the experiment.

Because of these, we control the refresh by gating the clock input to the output card. When there are channels to be updated, the clock is turned to the maximum speed. Otherwise, the clock is kept off so no refreshing is happening. Since the clock signal is generated by the FPGA, the gating is done by passing the clock on/off intervals computed by the NiDAQ backend to the FPGA backend. Since an extra or missing clock cycle may cause the output value during hold time to be significantly different from the desired value, the FPGA backend guarantees that the clock control command are always scheduled at the exactly time so that exact number of clock cycles can be sent to the output card.

We also observed that the driver of the card may timeout if not enough clock signals are recieved at the beginning of the sequence. We therefore always send 1 ms of clock signals to the card at the beginning of the sequence to work around this issue.

24

1.3.6 USRP Backend

In additional to the DDSs attached to the FPGA, we also support generation of radio frequency (RF) signals using universal software radio peripheral (USRP). Compared to the DDS, which can only output a single frequency at at time, USRP support output of arbitrary spectrum within a certain range. This can be useful when more than one frequency is needed on a single channel, e.g. for fast modulation of the amplitude using beating, or to generate multiple diffraction orders on an acousto optical beam deflector (AOBD).

Since most usage of the USRP output involves creating multiple discrete frequencies, the hardware is modelled in our system accordingly. Instead of mapping the physical output channel to a fixed number of parameters similar to all the previously mentioned backends, a "virtual" output channel is created for each tone in the output, and can be controlled independently similar to all other channels. The `<device_id>` component of the channel name has format `CH<n>/<param>` where `<n>` is a number identifying the virtual channel and `<param>` is the parameter controlling the virtual channel, e.g. `FREQ` for frequency or `AMP` for amplitude.

The driver API for USRP is very similar to that of the NI output card and requires the output value to be provided at regular time interval. However, due to the constant changing nature of the RF output and the higher sampling rate, the memory requirement would be too high if we take the same approach as the NiDAQ backend and compute all the output values before the sequences start. Instead, the backend uses a command stream similar to the one used by the FPGA backend to encode the change to the output spectrum. Unlike the FPGA backend, however, commands

can be issued for all the virtual channels simultaneously, removing the need to interleave update for different channels.

From the command stream, we generate the output at a sampling rate of 50 MS/s. The samples are computed on the fly which allows maximum flexibility and minimizes the time needed to generate the data before each sequence. The data throughput necessary to generate samples at the high rate is achieved thanks to the AVX2 instructions, which allows computation of multiple sine and cosine functions simultaneously[*]. In order not to interfere with the user interface tasks and to achieve more reliable performance for the sample generation, the program directly managing the USRP device runs on a separate computer running Linux. The communication with the main computer is done via ZMTP.

The USRP device does not have builtin support for triggering, which is necessary to synchronize its output with other devices. We implement this in software by converting the trigger signal to a COM port signal using an Arduino board and monitoring the COM port in the USRP server program. The trigger has a timing accuracy of 1 ms which is limited either by the timing of on the Arduino or the reading of the COM port on the server computer.

1.4 Automation of Scans

The core of the control system, as described in the previous sections, deals with the specification and realization of experimental sequences, which are the building block for all measurements we

---

[*]The AVX2 implementation of the math functions used is based on work by Yu Yang at `https://github.com/reyoung/avx_mathfun` which is based on work at `http://software-lisc.fbk.eu/avx_mathfun/` by garberoglio@fbk.eu.

do. However, most experiments require running multiple sequences to reduce statistical uncertainty and measure the effect of varying certain parameters. We add the concept of scans to the system in order to satisfy this requirement. A scan is a set of sequences where one or more experimental parameters are varied across the sequences. When running the scan, the system automatically selects sequences from the scan to run in random order in order to reduce potential systematic effects due to interference between sequences. The scan can be configured to run for a set number of times or until some pre-determined conditions are satisfied, which in our experiment typically happens when a certain number of single atom loading events happens.

The scan interacts with the sequence constructing code by storing the parameters for the scan in the sequence object `s` as a nested structure, which is accessed as `s.C`. Each substructures within the parameters can be accessed and passed independently which allows multiple instances of a common subsequence to store their parameters in the same way within the parent structure. As an example, a subsequence construction function may be implemented as

```
function subseq(s, p)
  % Access parameter1, with default value 0
  parameter1 = p.parameter1(0);
  % Access parameter2, which must be pre-defined
  parameter2 = p.parameter2();
  % ... Use parameter1 and parameter2 to construct s.
end
```

which may be used in the parent sequence as

```
% Construct one instance of the subsequence
% using substructure under Instance1
s.addStep(@subseq, s.C.Instance1);
% ...
% Construct another instance of the subsequence
% using substructure under Instance2
```

```
s.addStep(@subseq, s.C.Instance2);
```

The scan is represented by a `ScanGroup` object, which provides the following functions to construct a scan.

- A `ScanGroup` can store multiple basic scans each containing a multiple dimensional scan (see below) of parameters. The basic scans within a `ScanGroup` `sg` can be accessed through indexing, e.g. `sg(1)`.

- Multiple `ScanGroup` `sg1`, `sg2`, `sg3`, or the basic scans included can be concatenated into a single `ScanGroup` via the concatination syntax, e.g.

  ```
  [sg1, sg2, sg3(1), sg3(4)]
  ```

  This allows multiple different scans to run simultaneously, which is useful when running the experiment unattended for a long time, e.g. overnight.

- Within a basic scan, the parameter can be set to a fixed value via assignment, e.g.

  ```
  sg(2).Instance1.parameter1 = 2;
  ```

- Each basic scan allow multiple parameters to be scanned simultaneously forming a multidimensional array of parameters. A scan of the parameter along dimension `i` can be configured by assigning to `.scan(i)` for the parameter, e.g.

  ```
  sg(1).Instance1.parameter2.scan(2) = [1, 2, 3, 4];
  ```

- Multiple parameters can also be scanned along the same dimension in which case the length of the parameter values must be the same. E.g.

  ```
  sg(1).Instance1.parameter2.scan(2) = [1, 2, 3, 4];
  sg(1).Instance2.parameter2.scan(2) = [2, 3, 4, 5];
  ```

  is supported whereas

  ```
  sg(1).Instance1.parameter2.scan(2) = [1, 2, 3, 4];
  sg(1).Instance2.parameter1.scan(2) = [2, 3, 4];
  ```

  will raise an error.

28

- Parameters, fixed or scanned, can be set for all the basic scans in the `ScanGroup` by assigning to the emtpy index, e.g.

```
sg().Instance1.parameter1 = 3;
sg().Instance1.parameter2.scan(1) = [2, 3, 4];
```

1.5 Summary and Outlook

We have designed a computer control system for the experiment that is power and flexible yet requires minimum low level knowledge from the user. All the measurements done in this thesis are implemented using this system.

The design of the system, especially the user API, guarantees that continuous improvement can be made without major changes to existing user code. Examples of further improvements that could be made to the system includes,

1. Unlike other backends, the FPGA determines the timing of the experiment and only one instance of such device is allowed per experiment. This limits the number of output channels we can use that is attached to the FPGA (i.e., DDS and logical outputs). Allowing the FPGA to use an external clock could make it possible to use more than one FPGA in the experiment and thus increase the number of channels available.

2. Support for more devices can be added to the system.
   One such updated in progress uses the arbitrary waveform generator (AWG) boards from Spectrum Instrumentation. These are very similar to the USRP devices but the output have higher bandwidth and significantly lower noise.

3. The IR execution is one of the main factors affecting the performance of the sequence compilation. In additional to the compilation to native code mentioned previously, the function can also be vectorized to take advantage of SIMD instructions in order to further improve the performance.

4. The sequence is currently static and cannot depend on measured value during the experiment as feedback. Dynamic or runtime logic can be added to the sequence by recording and encoding the necessary logic that needs to be happened at runtime in a similar way we convert MATLAB code to the IR. Such capability will be important for implement rearrangement of tweezers in order to achieve high filling fractions.

2

Loading of Single Atoms in Optical

Tweezer

2.1 Introduction

The atoms we use in the experiment comes from alkali metal dispensers heated using an electric

current which have a starting temperature of $\approx 400 \sim 800\,\mathrm{K}$ and must be cooled to $< 0.1\,\mathrm{K}$ before

they can be captured by the optical tweezer. In this chapter, we will breifly discuss the cooling steps that bridge this temperature gap. In section 2.2, we will focus on the free space cooling on the atoms without involving the optical tweezer. Since most of the cooling techniques used in our experiment are quite standard, they will not be reviewed in detail here. Instead, we will mainly highlight the important specific design choices and their performance in our experiment as reference. Section 2.3 will discuss the loading and detection of the atom in the tweezer including a short summary of the unique challenge we face with Na atoms.

2.2 Free Spacing Cooling of Atoms

Our experiment begins with the loading of a Na Cs dual species magneto-optical trap (MOT) from the background pressure created by the dispensers. It is created using six cooling beams of $\approx$ mm diameter with $\approx$ mW (Na) and $\approx$ mW (Cs) power in each beams. The resulting MOT has a diameter of $\approx$ mm with $\approx$ (Na) and $\approx$ (Cs) atoms being trapped and cooled to to a temperature of $\approx$ mK (Na) and $\approx$ mK (Cs). The atom numbers are significantly smaller than the ones typically seen in a bulk gas experiment since the goal of the free-space laser cooling is to load atoms into the tweezers which does not require large atom numbers. The small size of the MOT requires a tigher tolerance on the MOT position in order to overlap with the optical tweezer for the loading of single atoms, which in turns increased the sensitivity to to the alignment and power balance of the cooling beams that determines the MOT position. Because of this, we use four independent fibers to deliver the power for the four horizontal cooling beams which allows independent control of the power

Figure 2.1: Beampath for generating the frequencies for Na MOT and optical pumping (OP). (Beampath for fiber coupling and frequency locking is not shown. The power control for the D1 laser is also omitted.) The D2 laser is locked on the F1/F2 crossover line using saturated absorption locking. It is shifted down by the two F2 double-pass (DP) AOMs to generate the frequency for the Na $F = 2$ state and shifted up by the F1 DP AOM to address the Na $F = 1$ state. The frequencies of the F1/F2 light are controlled by the F1 DP AOM and F2 DP AOM 2 respectively. This set up makes sure that when the F1/F2 DP AOMs are off, the closest frequency in the leaked light is at least detuned by half the F1/F2 separation ($\approx 880 \,\mathrm{MHz}$) [2] and will have minimum effect on the atom. The F1 and F2 light are combined on F1/F2 PBS 1 and their power ratio after the F1/F2 PBS 2 is controlled by the half waveplate between the two PBSs. A similar setup is used to combine the D1 and D2 light in the OP output using D1/D2 PBS 1 and the rotating D1/D2 PBS 2. Since we need to switch the Na MOT light on and off out-of-phase with the Na tweezer [3] at a high frequency, the sharpness of the turn on/off edge in the MOT AOM is important. We focus the beam through the AOM using lens L1 to optimize the switching time. This is then collimated by lens L2 for the downstream beampath.

Figure 2.2: Beampath for generating the frequencies for Cs MOT and optical pumping (OP). (Beampath for fiber coupling and frequency locking is not shown.) The F3 laser is locked using saturated absorption locking to the F3 atomic transition. The F4 laser is beat-locked to the F3 laser, which also controls its frequency. The F3 and F4 light are combined on MOT PBS 1 and OP PBS 1 and their power ratio in the MOT and OP output are controlled by the rotating MOT PBS 2 and OP PBS 2 respectively. The frequency of the F3 light in the MOT is fixed whereas the frequency of the F3 light in the OP is can be changed by the F3 OP DP AOM.

and alignment. We observed a more robust MOT and, as a result, single atom loading compared to using retro-reflectors to create conterpropagating horizontal cooling beams. Due to the geometric constraints in the experiment, retro-reflector is used for verticle cooling beams.

The MOT is followed by a compressed-MOT (CMOT) stage for Na which uses light closer to resonant to push the Na atoms closer to the center as well as reducing their temperature to $\approx$ mK. After this, the magnetic field is turned off and a polarization gradient cooling (PGC) step is applied on the atoms which cools the atoms to $\approx$ mK (Na) and $\approx$ mK (Cs).

The beampaths for generating all the necessary frequencies are shown in Fig. 2.1 (Na) and Fig. 2.2 (Cs). The same beampaths are also used for generating the light for cooling and imaging of single atoms as well as optical pumping for state preparation that will be discussed in later chapters.

2.3 Loading and Imaging in the Tweezer

We load the tweezer from a laser-cooled cloud of atoms. Since the tweezer provides a conservative potential, trapping of the atom requires its energy to be reduced. This can be done either by changing the trap depth, e.g. turning on the trap when an atom is at the focus to reduce its potential energy, or by a dissipative cooling process. However, due to the low trap volume of the tweezer and the density of the MOT, there is less than atom from the MOT in the tweezer, and the only method that works for loading tweezer in our experiment is by cooling the atoms into the tweezer. This cooling process also ensure that at most one atom can be loaded into the tweezer due to pair-wise loss from light-assisted collision.

Cooling in tweezer and loading using the free-space cooling beams works well for Cs. However, the cooling of Na atoms in the tweezer is more challenging due to the light shift from the tweezer. The higher trap depth necessary to trap the hotter Na atom after freespace cooling and the absense of an accessible magic wavelength causes a large () light shift on the cooling transition when the Na atom is in the tweezer. This shift significantly changes the cooling detuning making it ineffective in the tweezer. We fix this issue by alternating the cooling and the tweezer light at 2.5 MHz. The frequency is low enough to allow a few photon to be scattered when the cooling light is on to perform cooling on the atom, yet high enough compared to the highest trapping frequency in the tweezer to prevent parametric heating of the trapped atom.

We use florescence imaging to detect the atoms in the tweezer which requires cooling to prevent the photon recoil from heating the atom out of the tweezer before enough photons can be collect. This is done using the free-space cooling beams previously used for the MOT and the PGC. The photon scatterred from the atom in the tweezer is collected by the objective which is then focused onto a EMCCD camera for detection. We achieve a overall photon collection efficiency of 8 % and 5 % for Na and Cs respectively. The difference between the efficiency for the two atoms is mainly caused by the quantum efficiency of the camera.

In our experiment, the tweezer is generated by focusing trap light through an objective with a numerical aperture (NA) of 0.55. The wavelengths used for the tweezers are 700 nm (Na) and 1038 nm (Cs), which give diffraction limited beam waists of 0.6 μm and 0.9 μm respectively. The selection of the wavelength ensures that each atom can only trapped by their respective tweezer since,

1. The Na trap wavelength of 700 nm generates a repulsive potential for the Cs atom and there-
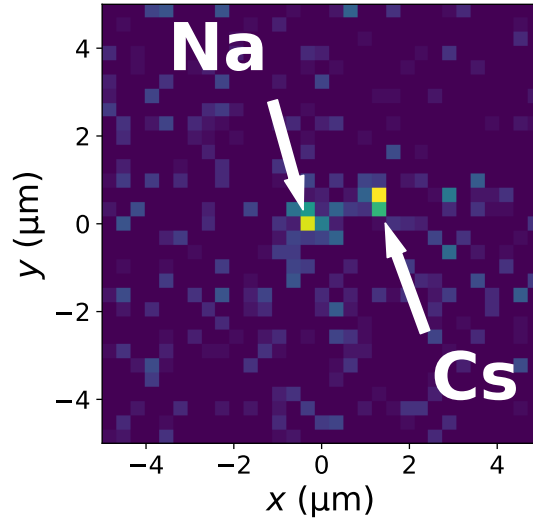
Figure 2.3: Image of a single Na and Cs atoms in their respective tweezers showing a simultaneous loading event.

fore cannot trap Cs.

2. The Cs trap can attract Na. However, the Cs trap is not being toggled out of phase with the Na cooling light and therefore cannot trap Na due to the light shift.

Due to technical limitations, we cannot measure the tweezer power directly. Instead we measure the power upstream in the tweezer beampath where the beam is accessible and correct for the known total transmission efficiency of $23(2)\%$ from the optics. The tweezer powers quoted in this thesis are directly measured power and must be multiplied by the factor 0.23 to obtain the best estimate of the total power at the focus of the tweezer.

The single atom can be observed on the EMCCD camera if the tweezer beam is turned on during MOT loading and the loading efficiency is improved by the additional free-space cooling steps including CMOT and PGC. Fig. 2.3 shows a image of both the Na and Cs atoms. In most experiments, however, the two species are imaged separately in order to reduce the background and to

improve the detection fidelity. We take a image for each atoms right after the loading step in order to determine which atoms (if any) are loaded and this is repeated at the end of each experimental sequences to determine if the atoms have survived. By repeating the experiment and sorting the events according to the loading result, we can accurately identify the case where a single (Na or Cs) or a pair of atoms are loaded and estimate the corresponding single- and two-body survival probability. Most of the measurements in this thesis are based on this probability.

2.4 Summary and Outlook

In this chapter we discussed the trapping and imaging of the single atoms in the optical tweezers and the steps leading up to it. We take advantage of many techniques developped and used in previous experiments to boost our control on the atoms in preparation for the control on the molecules.

The atoms trapped in the tweezers and the high fidelity detection of them form the fundation of our experiment. The utility of such system and the possibility it opens up will be discussed in more detail in the coming chapters.

3

Raman Sideband Cooling

3.1 Introduction

The trapping of the single atoms in the optical tweezers in section 2.3 improves our control on the

motional degrees of freedom of the atoms by confining it to the focus of the tweezer. However, the

temperature of the atoms directly after loading is still relatively high (mK for Na and mK for Cs)

compared to the trapping frequencies (80 $\sim$ 600 kHz or 4 $\sim$ 150 mK for Na and 20 $\sim$ 160 kHz

39

or $1 \sim 8$ mK for Cs) of the tweazer causing a large number of motional states to be occupied ($\approx$ for Na and $\approx$ for Cs). Further cooling into the motional ground state of the tweezer for both atoms are required in our experiment for two reasons,

1. Our assembly approach relies on the preparation of atomic quantum states to realize full control of the molecule. More concretely, the temperature and motional states of the molecule we create is directly related to the cooling of the atoms in the tweezer.

2. Cooling to the motional ground state reduces the size of the atomic wavefunction. This increases the interaction between the atoms and improves the coupling to the molecular states as will be shown in later chapters.

The confinement provided by the optical tweezer and the relatively high trapping frequencies enables the potential the use of Raman sideband cooling (RSC) in our experiment to reach the motional ground state. Originally developed for ion systems to take advantage of the tight confinement from ion traps, resolved sideband cooling has been later implemented for neutral atomic systems using Raman transitions using both optical lattices and optical tweezers on multiple species. Still, the application of RSC requires a favorable initial cooling and very tight confinement from the trap and remains challenging and underexplored outside this regime (formally known as the Lamb-Dicke regime, which is defined later in section 3.2.1). The efficient polarization gradient cooling for Cs atoms allows RSC to be implemented in a similar fashion as previous experiments achiving a ground state probability of %.

Unfortunately, the parameter achievable for Na lands outside the Lamb-Dicke regime making the implementation of RSC much more challenging. In this chapter, we will discuss how we overcome these challanges and achieved ground state cooling using RSC in our experiment. We will start in
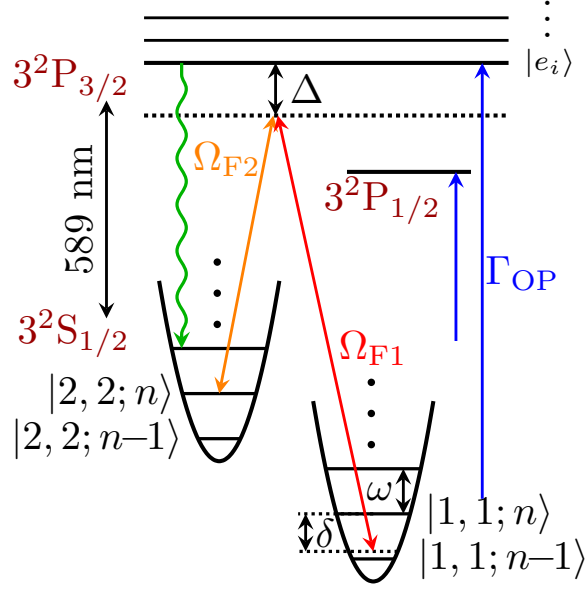
Figure 3.1: Single Na atom Raman sideband cooling scheme. The Raman transitions couples $|2, 2; n\rangle$ and $|1, 1; n + \Delta n\rangle$ through the intermediate states $|e_i\rangle$ in the $3^2P_{3/2}$ electronic states. The transitions have a one-photon detuning $\Delta_i \approx$ 75 GHz. Two-photon detuning, δ, is defined relative to the $\Delta n = 0$ carrier transition. For optical pumping, we use two σ^+ polarized transitions, one to pump the atom state out of $|1, 1\rangle$ via $3^2P_{3/2}$ and one to pump atoms out of $|2, 1\rangle$ via $3^2P_{1/2}$ to minimize heating of the $|2, 2\rangle$ state.

section 3.2 and 3.3 with a description of the theory for RSC and the related thermometry technique.

Section 3.4 describes the experimental setup for RSC. The challenges related to cooling outside the

Lambd-Dicke regime are analyzed in detail in section 3.5 followed by section 3.6 and 3.7 listing the

solution we developed to overcome these challenges. The experimental realization and result of the

cooling sequence are discussed in section 3.8, 3.9 and 3.10 before the summary in section 3.11.

3.2 Basic Theory

The relevant energy diagram and the laser frequencies for RSC are shown in Fig. 3.1. We approximate the trapping potential using a harmonic oscillator. Since this is a separable potential, we can use only the 1D motional state $|n\rangle$ and the result can be easily generalized to the full 3D system.

The cooling sequence consists of two types of pulses. First, a Raman pulse drives the atom to a different hyperfine state while simultaneously reduces the motional energy of the atom. The optical pumping (OP) pulse afterwards then reset the hyperfine state of the atom and reduce the entropy of the system. This sequence is then repeated until the system reaches the ground motional state where there is no more motional energy to be taken out of the system via the Raman pulse. In this section, we will discuss the theory of each types of pulses individually. We will cover how the pulses affect cooling performance in section 3.5.

3.2.1 Raman Transition

As shown in Fig. 3.1, the cooling sequence starts with the sodium atom in the $|s_1\rangle \equiv |2, 2\rangle$ hyperfine state, and a Raman transition is used to drive the atom to the $|s_2\rangle \equiv |1, 1\rangle$ state, where $|F, m_F\rangle$ denotes the F and m_F quantum number for the sodium atom. The full Rabi frequency for such a transition is given by

$$\Omega_R^0 = \sum_i \frac{\Omega_{1i}\Omega_{2i}^*}{2\Delta_i} \tag{3.1}$$

where the sum is over all the coupled excited states, $\Omega_{ai} \equiv \langle a | \mathbf{d} \cdot \mathbf{E}_a | e_i \rangle$ is the single photon Rabi frequency between $|a\rangle$ and $|e_i\rangle$ and Δ_i is the single photon detuning from excited state $|e_i\rangle$.

In order to account for the motional degrees of freedom, we need to include the spatial wavefunction of the atom and light into account. As mentioned above, we approximate the atomic motional wavefunction by the harmonic oscillator eigenstates $|n\rangle$. Coupling between states different n states from the Raman transition is allowed due to the recoil from the Raman lasers, which corresponds to a spacial phase imprinting of $e^{i\Delta\mathbf{k}\cdot\hat{\mathbf{x}}}$ where $\Delta\mathbf{k}$ is the wavevector difference between the two Raman beams. Using the creation ($\hat{a}^\dagger$) and annihilation ($\hat{a}$) operators and the relation $\hat{\mathbf{x}} = \mathbf{x}_0 (\hat{a} + \hat{a}^\dagger)$ where $x_0 = \sqrt{\hbar/2m\omega}$ is the harmonic oscillator length, the phase factor can be expressed as $e^{i\eta^R(\hat{a}+\hat{a}^\dagger)}$ where $\eta^R \equiv \Delta\mathbf{k} \cdot \mathbf{x}_0$ is the Lamb-Dicke parameter for the Raman transition. The matrix element between motional state $|n\rangle$ and $|n'\rangle$ is therefore,

$$M_{n,n'} = \langle n | e^{i\eta^R(\hat{a}+\hat{a}^\dagger)} | n' \rangle$$

and the final Raman Rabi frequency between motional states n and n' is given by,

$$\Omega_R^{n,n'} = M_{n,n'} \Omega_R^0$$

For $n = n'$, this is called a carrier transition and the others are called sideband transitions. If the final state is higher than the initial one, i.e. $n' > n$, it is a heating sideband. Likewise, transitions with $n' < n$ are cooling sidebands.

A closed form result for $M_{n,n'}$ is given in Ref. [4],

$$M_{n,n'} = e^{\left(\eta^{\mathrm{R}}\right)^2/2} \sqrt{\frac{n_<!}{n_>!}} \left(\eta^{\mathrm{R}}\right)^{|n-n'|} L_{n_<}^{|n-n'|} \left(\left(\eta^{\mathrm{R}}\right)^2\right)$$

where $n_<$ and $n_>$ are the lesser and greater, respectively, of n and n', and L_n^α is the generalized Laguerre polynomial,

$$L_n^\alpha(x) \equiv \sum_{m=0}^{n} (-1)^m \begin{pmatrix} n+\alpha \\ n-m \end{pmatrix} \frac{x^m}{m!}$$

An important limit is the so-called Lamb-Dicke (LD) regime defined as $\left(\eta^{\mathrm{R}}\right)^2(2n+1) \ll 1$. In this case, we can approximate the phase factor in leading order of η^{R},

$$e^{i\eta^{\mathrm{R}}\left(\hat{a}+\hat{a}^\dagger\right)} \approx 1 + i\eta^{\mathrm{R}}\left(\hat{a}+\hat{a}^\dagger\right)$$

and the matrix element

$$M_{n,n'} \approx \delta_{n,n'} + i\eta^{\mathrm{R}}\sqrt{n+1}\delta_{n+1,n'} + i\eta^{\mathrm{R}}\sqrt{n}\delta_{n,n'+1}$$

the three terms corresponds to the carrier ($n' = n$), the first order heating sideband ($n' = n+1$) and the first order cooling sideband ($n' = n-1$) with corresponding strength 1, $\eta^{\mathrm{R}}\sqrt{n+1}$ and $\eta^{\mathrm{R}}\sqrt{n}$. We can clearly see from this approximation that the coupling to other motional state is stronger for a larger η^{R} and higher motional quantum number n. We will discuss this effect outside the LD regime and its implication on the cooling performance in more detail in section 3.5.

44

3.2.1.1 Scattering from Raman Beams

In additional to driving the Raman transition, the Raman beams can also cause scattering. The rate of the scattering is [*],

$$\Gamma = \sum_i \frac{\Gamma_{ei}\Omega_{1i}^2}{4\Delta_i^2}$$

where Γ_{ei} is the linewidth of the excited state $|e_i\rangle$. Together with Eq. 3.1, we see that approximately $\Gamma/\Omega_R \propto 1/\Delta$ so a larger detuning should be used in order to reduce the scattering during RSC.

3.2.2 Optical Pumping

Driving the system on a cooling sideband with Raman transition can reduce the motional energy of the atom. However, this is a fully coherent process that does not reduce the system entropy and is not really "cooling" the system or achieving better control on the quantum state of the system. Instead, quantum state control is achieved in the RSC via the OP pulse. The initial hyperfine state $|2, 2\rangle$ is a stretched state so it is the state the system naturally ends up in when σ^+ light is applied. However, if this is done using scattering from a $F = 2$ to $F' = 3$ transition, the OP beam will allow continuous photon cycle between the $|2, 2\rangle$ and the $|3', 3\rangle$ causing unnecessary motional heating during OP. Therefore, the OP must be done on a $F = 2$ to $F' = 2$ transition. Unfortunately, for Na, the corresponding transition from $3^2S_{1/2}$ to $3^2P_{3/2}$ that is used for the MOT is not useable due

---

[*]Here we assume that each Raman beam only couples to their respective ground states. Including coupling to the other ground state increases the scattering rate but does not change the scaling with detuning.

to the small energy difference of 60MHz (or 6 line widths) between the $F' = 2$ and $F' = 3$ states [2]. Instead, we must use the sodium D1 line, i.e. $3^2S_{1/2}$ to $3^2P_{1/2}$ transition, which lacks a $F' = 3$ excited state [5, 6]. We find a reduction in the scattering rate by a factor of $130(20)$, as compared to using an OP resonant with $3^2P_{3/2}$. The D1 light with σ^+ polarization is only used to pump atoms from $F = 2$ states (in particular $|2, 1\rangle$ which is populated during the OP process). Since the goal of the OP pulse is to clear the atom population in all states but $|2, 2\rangle$, the photon cycling is not a concern for $F = 1$ states and the D2 line is used for OP of $F = 1$ states instead. This also allow us to reuse the MOT light source and simplifies our setup.

3.3 Raman Sideband Thermometry

From the discussion in section 3.2.1, we see that the strength of the sideband transition depends on the initial motional state as well as the Lamb-Dicke parameter η^R of the atom. This dependency allows us to infer the motional state of the atom by measuring the sideband height, i.e. the so-called sideband thermometry [5, 7].

In particular, for atom with temperature T, the probability for the atom to be in motional state $|n\rangle$ is,

$$p_n = \left(1 - e^{-\hbar\omega/k_B T}\right) e^{-n\hbar\omega/k_B T}$$

for a Raman pulse with full Rabi frequency Ω_R^0 and time t, the peak height for the first order heat-

ing (+) and cooling (-) sidebands,

$$h_{\pm} = \sum_{n=0}^{\infty} p_n \sin^2\left(\frac{\Omega_R^0 t}{2} M_{n,n\pm 1}\right)$$

note that $p_{n+1} = p_n e^{-\hbar\omega/k_B T}$, $M_{n,n'} = M_{n',n}$ and $M_{n,-1} = 0$, we have

$$
\begin{aligned}
h_- &= \sum_{n=0}^{\infty} p_n \sin^2\left(\frac{\Omega_R^0 t}{2} M_{n,n-1}\right) \\
&= e^{-\hbar\omega/k_B T} \sum_{n=1}^{\infty} p_{n-1} \sin^2\left(\frac{\Omega_R^0 t}{2} M_{n-1,n}\right) \\
&= e^{-\hbar\omega/k_B T} h_+
\end{aligned}
$$

Therefore, if we measure the ratio of the cooling and heating sideband heights $\alpha \equiv h_-/h_+$, we can calculate the temperature of the atom with $e^{-\hbar\omega/k_B T} = \alpha$. The corresponding ground state probability is,

$$
\begin{aligned}
p_0 &= 1 - e^{-\hbar\omega/k_B T} \\
&= 1 - \alpha
\end{aligned}
\tag{3.2}
$$

Figure 3.2: Geometry and polarizations of the Raman and optical pumping beams relative to the optical tweezer and bias magnetic field. Raman beams R1 and R4 address the radial x-mode. R1 and R2 address the radial y-mode. R3 and R4 address the axial z-mode, where the beams also couple to radial motion, but this coupling can be neglected when the atoms is cooled to the ground state of motion.

and the average motional state

$$\bar{n} = \sum_n n\alpha^n$$

$$= \frac{\alpha}{1-\alpha} \tag{3.3}$$

We will use these to experimentally characterize the performance of the cooling sequence in the following sections.

The geometry of all the beams and field involved is shown in Fig. 3.2. In order to make the cooling more efficient and simplify the sideband thermometry, we address the motion along the three principle axis of the tweezer using different pairs of Raman beams. In order to maximize the beam intensity so that a larger single photon detuning can be used while maintaining the same Raman Rabi frequency, we focus the Raman beam onto the single atom with a waist of $\approx$ 100 μm. The maximum powers within each Raman beam are between 1 and 6 mW which give us a maximum Raman Rabi frequency of 50 to 200 kHz.

We apply an external bias magnetic field of 8.8 G parallel to the polarization of the tweezer beam (and orthogonal to the tweezer beam propagation direction). This makes the field orthogonal to the effective magnetic field of the tweezer, which minimizes the vector light shifts [8, 9]. Since the optical pumping beam requires σ^+ polarization, it is setup to propagate parallel to the applied magnetic field.

3.5 Cooling Performance and Challenge with Large Lamb-Dicke Parameter

RSC is typically performed in the LD regime where the coupling to other motional state is small. Due to the light mass, short wavelength, limitted trap depth and high initial temperature of the sodium atom however, we have to start our RSC sequence outside the LD regime. This creates unique challenges to our experiment. A detailed understanding of the cooling performance is required to understand and overcome these challenges.

The simplest way to estimate the effectiveness of RSC is by keeping track of the average energy of the atom during the cooling sequence. For a typical RSC sequence in the LD regime, all the cooling are done on the strongest first order cooling sideband. The energy removed for atom driven in one Raman pulse is therefore, $\Delta E_- = \omega$. In order to reinitialize the hyperfine state, the sodium atom needs to scatter on average 2 photons from the OP pulse which increases the average energy of the driven atom by $\Delta E_+ = 4\omega_{\mathrm{recoil}}$ * where $\omega_{\mathrm{recoil}} \equiv \hbar k^2/2m$ is the recoil energy [2] and k is the OP light wave vector. The heating to cooling ratio in one RSC pulse cycle is therefore,

$$\frac{\Delta E_+}{\Delta E_-} = \frac{2\hbar k^2}{m\omega} = 4k^2 x_0^2$$
$$= 4\left(\eta^{\mathrm{OP}}\right)^2$$

where $\eta^{\mathrm{OP}} \equiv kx_0$ is the Lamb-Dicke parameter for OP. Therefore, in order to achieve net cooling, we need $\left(\eta^{\mathrm{OP}}\right)^2 < 0.25$. In 3D with cooling along multiple axis with different trapping frequency, and therefore different η^{OP}, the $\left(\eta^{\mathrm{OP}}\right)^2$ in the requirement is replaced by a weighted average of different axis depending on the frequency each axis is cooled in the sequence.

In our experiment, the OP Lamb-Dicke parameters are $\eta_x^{\mathrm{OP}}, \eta_y^{\mathrm{OP}}, \eta_z^{\mathrm{OP}} = 0.25, 0.25, 0.55$. Based on the metric above, any cooling sequences that have fewer than 78 % cooling pulse for z (axial) axis, which is generally the case, should have a net cooling effect. This, however, does not guarantee cooling into the ground motional state, nor does it fully characterize the efficiency of the cooling sequence since the averaging hides a few critical aspect of having a large Lamb-Dicke parameter.

---

*The factor of 4 comes from 2 absorbed photons and 2 reemitted photons.

Figure 3.3: Optical pumping motional-state redistribution and Raman coupling for large LD parameters for the axial direction (z) [10]. The range plotted covers 95% of the initial thermal distribution. (A) Motional state distribution after one OP cycle for different initial states motion, n_init. Due to photon-recoil and the large LD parameter, $\eta_z^\text{OP} = 0.55$, there is a high probability of n changing. (B) Matrix elements for Raman transition on the first order cooling sideband deviate from $\sqrt{n}$ scaling with multiple minima.

One of the important effects can be seen in Fig. 3.3A showing the motional state distribution after one OP cycle for different initial motional states n_init [10]. Although the average heating is fixed at $4\omega_\text{recoil}$, independent of n_init, the spread or the uncertainty of n after the OP is significantly higher for high n_init. This effect significantly increases the difficulty in controlling the state during the RSC sequence. It can negatively impact the cooling performance and may lead to increased loss during cooling due to atom escaping to higher motional states.

The other important effect is the dependency of matrix element $M_{n,n+1}$ on the motional level n. While this dependency is not a new effect, since the $\sqrt{n}$ dependency on the cooling sideband strength exist even in the LD regime and must be taken into account with pulse time variation [4, 11] to achieve efficient cooling, the high Lamb-Dicke parameter adds even more complications. As shown in Fig. 3.3B, rather than a simple $\sqrt{n}$ dependency, it is a non-monotonic function and more importantly has multiple minima, so-called "dead-zone", within the range of motional states we are

Figure 3.4: Matrix elements for Raman transition including high order sidebands. During cooling, we utilize the fact that high motional states couple most effectively to sidebands with large $|\Delta n|$ in order to overcome the issue with variation and dead zone in the coupling strengths.

interested in [10]. The coupling strength for states in the dead-zones can be reduced by more than ten times which can significant affect the efficiency of the cooling pulse and even makes it virtually impossible to drive Raman transitions on atoms in these states in order to cool them further. A cooling sequence can therefore accumulate pupolations in the dead-zones rather than the ground state. Their small coupling strength also reduce their signal level during Raman sideband spectroscopy making these states nearly invisible to sideband thermometry which further complicates the optimization of the cooling sequence.

3.6   Solution: High Order Sidebands

The main solution to the issues related to the large Lamb-Dicke parameter is in fact the large Lamb-Dicke parameter itself. The increased coupling to other motional state for large Lamb-Dicke parameter and high motional states applies not only to $|\Delta n| = 1$ but to higher Δn as well. Fig. 3.4 shows

the coupling to higher order cooling sidebands which all have comparable strengths as the first order sidebands in different ranges of motional states.

Because of this, it is now possible, and in some cases preferred, to apply Raman cooling pulse on the higher order sidebands instead of only the first order one. These pulses reduce more energy from the system per pulse which directly improves the cooling to heating ratio and allows better control on the motional state given the uncertainty after an OP pulse. More importantly, depending on the motional level, there is always a sideband order with significant coupling strength that can be used to cool it, therefore completely removing the coupling dead-zones. Moreover, by using each sideband orders only near their coupling maxima, the coupling strength variation is also greatly reduced which removes the need to vary the pulse times for all but the pulses on the first order sideband.

3.7   Solution: Simulation Based Optimization

The change in cooling technique by including higher order sidebands, however, does not remove the effect of coupling variation on the sideband thermometry. If a non-thermal distribution of motional states is produced by the cooling sequence, the ratio of the first order sideband height still cannot be trusted to calculate the temperature or the ground state probability. Including higher order sidebands in the sideband thermometry could in principle give us enough information about the state distribution but doing so for a non-thermal distribution is not easy or reliable. We therefore use a Monte-Carlo simulation to guide our search for the optimal sequence [13]. The simulation includes accurate scattering rate and branching ratios from the tweezer, Raman and OP beams. For

53
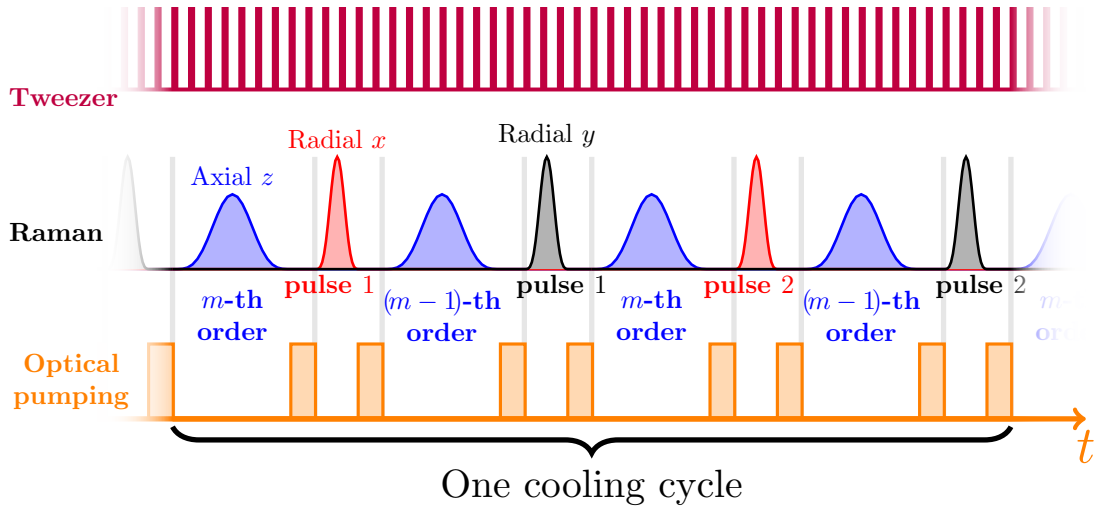
Figure 3.5: Schematic of the cooling pulse sequence. The tweezer is strobed at 3 MHz to reduce light shifts during optical pumping [3]. Each cooling cycle consists of 8 sideband pulses. The four axial pulses address two sideband orders. The two pulses in each radial direction either address $\Delta n = -2$ and $\Delta n = -1$ or have different durations to drive $\Delta n = -1$, at the end of the cooling sequence when most of the population is below $n = 3$. The Raman cooling and spectroscopy pulses have Blackman envelopes [12] to reduce off-resonant coupling, while the measurement Rabi pulses in Fig. 3.7 have square envelopes to simplify analysis.

best simulation performance, the atom is assumed to be in a single motional state, i.e. with a certain n_x, n_y and n_z, after each Raman or OP step [*]. It is also assumed that each Raman pulse drives only the intended sideband order, which is a property that needs to be ensured in the experiment (section 3.9.1). For each cooling sequence simulated, the Raman beam power and frequency, and the OP beam power and polarization purity are varies slightly around the respective expected values in order to confirm the robustness of the sequence against fluctuation in the experiment. Fig. 3.5 demostrate the resulting optimal sequence from the simulation. In particular, we find that alternating the cooling pulses between two neighboring orders for the axial direction and $\Delta n = -2$ and $\Delta n = -1$ for the radial directions eliminates the accumulation of population in motional states

---

[*]This assumes no coherence between different motional state, which is the case as long as each Raman pulses are separated from each other by OP pulses.

with small Raman coupling. The simulation also confirms that setting the coupling strength of each sideband to drive a Rabi π-pulse corresponding to the maximum matrix element motional state (i.e. the maxima in Fig. 3.4) yields efficient cooling, initially, as we expected from section 3.6. The efficiency of cooling on higher-order sidebands diminishes as the atom approaches the ground state, so the final cycles utilize only the $\Delta n = -1$ sideband while alternating between the three axes.

3.8   Alignment of Raman and OP Beams

Due to small waist of the Raman beam, it is important to align the Raman beam to the single atom with high precision in order to maximize the Raman Rabi frequency as well as minimizing the intensity fluctuation of the Raman beam experienced by the atom due to pointing instability. Such precision cannot easily be achieved using external reference and must be done by using the single atom itself as the alignment target.

In our experiment, we have developed two different methods to align or verify the alignment of the Raman beams, both relying on the scattering from the Raman beams. For initial alignment, or when the beam position is off-center by more than a beam waist, we couple resonant Sodium D2 light into the Raman beam path in order to enhance the scattering rate. The course alignment is done based on maximizing depleting and displacement of the MOT due to radiation pressure. After that, the fine alignment of the Raman beam is done by reducing the power in the Raman beam path and maximizing the heating effect on the single atom. When the Raman beam is focused on the tweezer position, we can observe a depletion of the single atom live loading signal while the MOT

is not affected as significantly. This process is then repeated with lower power in the Raman beam path until the desired position sensitivity is reached.

In order to verify the alignment of the tweezer without any physical change to the beam path, we use a second method to calibrate the single photon Rabi frequency of the Raman light. This method requires a working OP to initialize the spin state of the atom so it is less convenient for aligning from scratch. To use this method, the atom is first loaded in the tweezer and initialized in the $|2, 2\rangle$ state. We then turn on a single Raman beam at maximum power for a variable length of time. The off resonance scattering from the Raman beam will cause the spin state of the atom to change and the population in $F = 1$ state is measured by removing the $F = 2$ population using a pushout pulse. The rate of the spin change is fitted to a theory model to derive the Rabi frequency of the Raman light. This measurement shows that the Rabi frequencies for the Raman beams are ... . We can also calculate the scattering rate from the Raman beams to be ... which corresponds to a total of ... scattering event on average during the whole cooling sequence and should not be a limiting factor for the cooling performance.

The OP beam has a much larger waist ($\approx$ 1 mm) and therefore require less alignment in the beam position. However, in order to take advantage of the dark state optical pumping and minimize unnecessary scattering for atoms in the $|2, 2\rangle$ state, the OP beam need to have a pure σ^+ polarization. This requires the OP beam to propagate parallel to the magnetic field in additional to having the currect circular polarization. The alignment is done by minimizing "depumping" of the atom spin state caused by the OP beam, similar to the technique we used to calibrate the Raman beam Rabi frequency. After the atom is initialized in the $|2, 2\rangle$ state, we turn on the D1 OP light for a

certain time which should not address the atom when perfectly aligned. The misalignment of the beam, however, will cause the atom to scatter from the OP beam and change to $F = 1$ state, i.e. "depumped", with certain probability. We then change the alignment of the beam an minimize the depumping rate. Due to a similar requirement for Cesium OP, the probagation direction of the OP beam for Sodium and Cesium are aligned to each other by overlapping them using mechanical target to better than $0.08°$ first before the magnetic field direction is aligned to the OP beams by minimizing depumping. For polarization alignment, we first clean up the linear polarization of the light using a Thorlabs nanoparticle linear film polarizer with better than $100,000 : 1$ extinction ratio. After that we use both a half waveplate and a quater waveplate to generate a circularly polarized light. We observed that both the polarization cleanup and the half waveplate is necessary to obtain the best polarization alignment in order to compensate for the polarization fluctuation caused by the fiber as well as the birefringence of the optics and windows within the OP beam path. After alignment, the OP intensity is calibrated by measuring the OP rate for atom prepared in $|2, 1\rangle$ state using Raman transitions[*]. From this measurement we determined that the purity of the OP polarization to be ...

.

Other than the alignment procedure above, we have also observed that reflection of the OP beam can contribute significantly to the polarization impurity and must be avoided. In particular, since the Raman beam R1 counter propagate with the OP beam, it is possible for the OP beam to be coupled into the Raman fiber and then retro-reflected to be focused onto the atom through the Raman beam path at a wrong polarization. Since the Raman beam size is much smaller, we have observed as

---

[*]One from $|2, 2\rangle$ to $|1, 1\rangle$ and a second one from $|1, 1\rangle$ to $|2, 1\rangle$.

much as 3 % polarization impurity caused by this mechanism despite only a small amount of power being reflected. This issue, along with other reflections, are reduced by avoiding optics with normal incident on the exit path of the OP beam as well as changing the propagation direction of the R1 Raman beam to have a small angle with the OP beam which reduces the OP power coupled into the Raman beam fiber.

3.9 Implementing Optimized RSC Sequence

In order to achieve the optimal cooling performance, a few more considerations are important for implementing the sequence from section 3.7.

3.9.1 Pulse shaping

In order to achieve optimal performance from the cooling sequence, it is important to accurately drive the intended sideband order. In fact, in the absense of undesired scattering, the frequency resolution of the Raman transition limits the lost achievable temperature. This is particularly important when driving the first order cooling sidebands since any coupling to the carrier may change the spin state of the atom without removing any motional energy therefore causing a net heating effect after the OP pulse.

The obvious way to achieve this is to narrow the linewidth of the Raman transition, e.g. by using a lower power or Raman Rabi frequency. However, reducing the lineiwth of the transition also increase the susceptibility to resonance fluctuation. Therefore the desired solution is to reduce the off-resonance coupling of the Raman beam for large detuning while increasing or maintaining the

coupling for small detuning. We achieve this by using a Blackman pulse shape for the Raman transition [12]. *

3.9.2 Calibration

The Raman sideband frequencies are calibrated by measuring the Raman spectrum before cooling (an example of which is shown in the initial spectrum in Fig. 3.6). However, since high sideband orders are mainly used to cool atoms in high motional state, the resonance frequency for these sideband are not equal spacing anymore due to the anharmonicity of the trap. In order to estimate the effect on the sideband frequencies, we can define anharmonicity as $A_{i,n} = (E_{i,n+1} - E_{i,n})/h - \omega_i/(2\pi)$ for each trap axis i, and calculated from the quartic term of the optical tweezers via perturbation theory. In the paraxial approximation, we find $A_{i,n} = \frac{-3n\hbar}{4\pi m d_i^2}$, where d_i equals the beam radius for the radial directions and $d_z \approx \pi w_{0,x} w_{0,y}/\lambda_{\text{trap}}$. Numerically, $\{A_{x,n}, A_{y,n}, A_{z,n}\} = \{-1.4, -1.4, -0.16\}n$ kHz. For the states addressed by high order sidebands, this broadens and shifts high-order sidebands due to the n-dependence of the transitions.

To mitigate this, we calibrate the frequency of each sideband order individually at the initial temperature. However, since the first order sideband is mainly used to cool atoms that are closed to the ground state, their resonance frequency is recalibrated using partially cooled atoms after the initial calibration. The use of high Rabi frequency and Blackman pulse shape also reduces the effect of anharmonicity by broadening the spectrum as much as possible.

---

*While more complex pulses can be constructed to achieve a even sharp detuning cutoff, such pulses generally significantly increases the pulse time and can cause more heating during cooling due to scattering and other heating mechanisms. The Blackman pulse we use offers a balance between the pulse time and off-resonance coupling reduction.

Although we can calibrate the single photon Rabi frequency of the Raman beams from the scattering rate (section 3.8), we also calibrate the Raman Rabi frequency on the carrier and different sideband orders. This offers a more direct and sensitive measurement for the cooling sequence parameter. Unlike resonance frequency, the anharmonicity only has a second order effect on the Rabi frequency and is therefore ignored. The calibration measures only the carrier and first order heating sideband which has the highest signal after cooling (an example of which is shown in the cooled Rabi flopping signal in Fig. 3.7). The Raman Rabi frequencies measured on these two transitions are used to calculate the full Rabi frequency Ω_R^0 and the Lamb-Dicke parameter, which are in-turn used to calculate the Rabi frequency on other sideband orders.

Since the final calibration of both the Raman Rabi frequency and resonance requires a working cooling sequence, when optimizing the sequence from scratch, the calibration process is applied iteratively as the cooling performance is improved.

3.10   COOLING PERFORMANCE

Our final cooling results are shown in Fig. 3.6 and 3.7. In total, 540 cooling pulses (total duration 53 ms) are applied along three axes with cooling beginning on the radial second order and axial fifth order. The full sequence including calibrated parameters can be found in appendix B.

For the more tightly confined radial directions, we observe clear $\Delta n = 1$, $\Delta n = -1$, and $\Delta n = -2$ sidebands before RSC, as is shown in Fig. 3.6A and B. After RSC, the $\Delta n = -1$ and $\Delta n = -2$ sidebands on both radial axes are strongly reduced. Using Eq. 3.2 and 3.3, we obtain $\bar{n}_x = 0.019(4)$
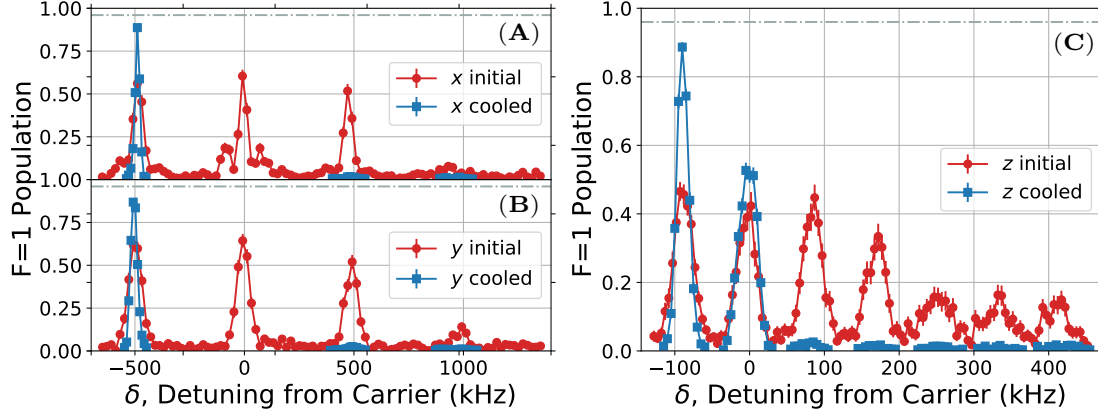
Figure 3.6: Raman sideband spectra for (A) x, (B) y, (C) z axis before (red circle) and after (blue square) applying Raman sideband cooling sequence. The height of the cooling sidebands (positive detuning) are strongly suppressed after cooling which suggests most of the atoms are cooled to the motional ground state in the trap.

Figure 3.7 (*following page*): Rabi flopping on radial axis x (A) carrier and (B) $\Delta n_x = 1$ sideband, radial axis y (C) carrier and (D) $\Delta n_x = 1$ sideband, axial axis z (E) carrier and (F) $\Delta n_x = 1$ sideband, before (red circle) and after (blue square) Raman sideband cooling.

Solid lines (both red and blue) in all plots are fits to a Rabi-flopping that includes a thermal distribution of motional states [7] as well as off-resonant scattering from the Raman beams.

The blue lines correspond to a ground state probability of (A-D) $98.1\,\%$ along radial axis and (E-F) $95\,\%$ along the axial axis after cooling. The red lines correspond to a thermal distribution of $80\,\mu\mathrm{K}$ before RSC. The horizontal dashed lines in all the plots correspond to the $4\,\%$ probability of imaging loss.

The green dashed line in (F) includes the additional decoherence due to a fluctuation of the hyperfine splitting of magnitude $3\,\mathrm{kHz}$. We see that the decoherence effect is strongest for the post-cooling data on the axial $\Delta n_z = 1$ sideband where the Rabi frequency is the lowest.
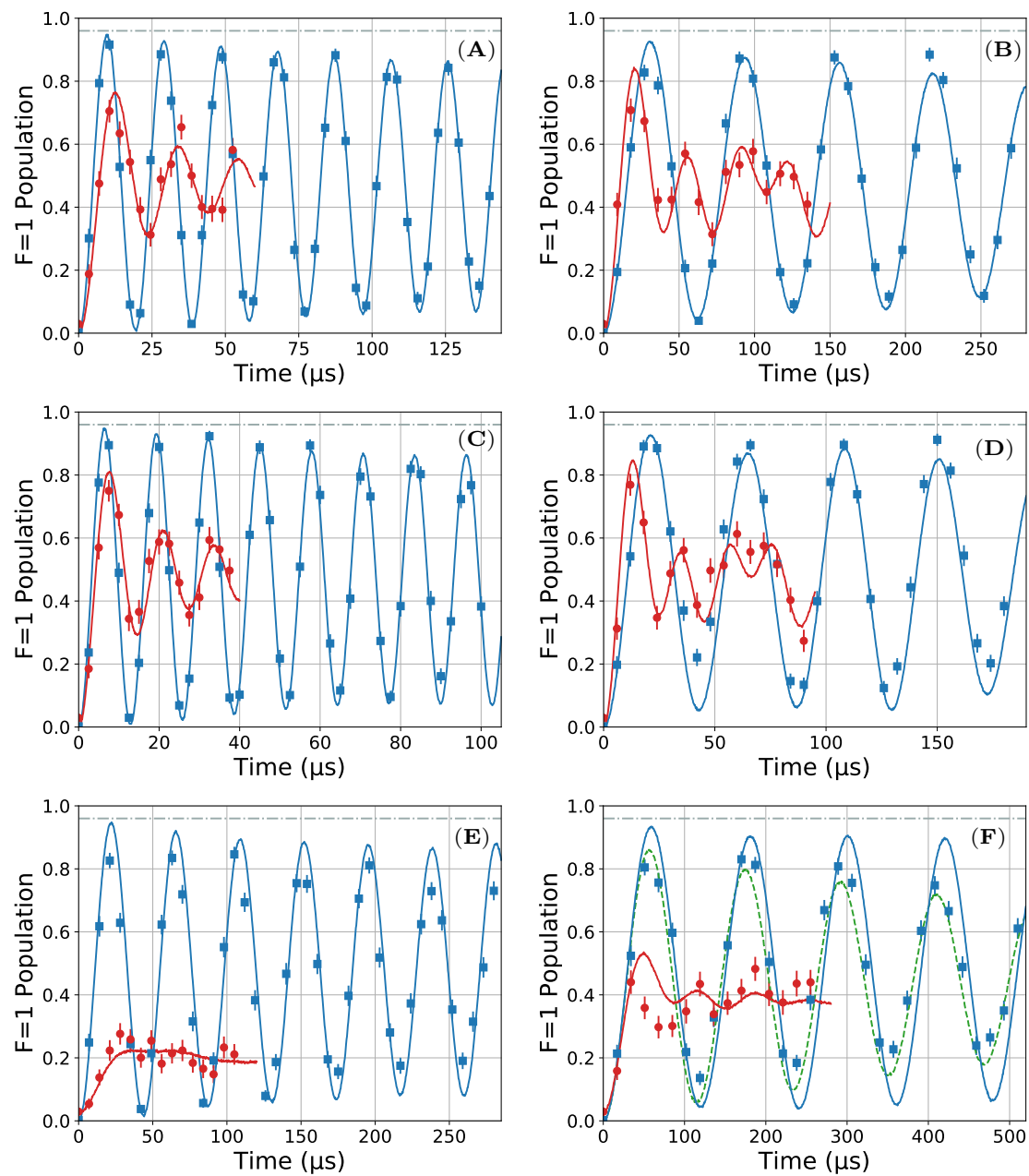
and $\bar{n}_y = 0.024(3)$ from the spectrum which correspond to ground-state fractions of 98.1(5) %
and 97.6(3) %, in agreement with fitted values of 98(1) % and 95(3) % from the Rabi flopping
curves [7] in Fig. 3.7A-D. The initial temperature of 80 μK before RSC is obtained from similar fits.

For the weak axial direction where cooling is challenging because the atom starts outside the
LD regime, we observe up to 5th-order Raman cooling sidebands initially, which indicates pop-
ulation in highly-excited motional states. Nevertheless, our cooling sequence works efficiently as
all the $\Delta n < 0$ sidebands are reduced after RSC (Fig. 3.6C). Using the ratio of first-order side-
band heights, we obtain $\bar{n}_z = 0.024(5)$, which corresponds to a ground state population of
97.6(5) %, in agreement with a ground state population of 95(4) % extracted from Rabi flopping
when $\Delta n = 0$ (Fig. 3.7E). For the $\Delta n = 1$ sideband (Fig. 3.7F), we observe additional decoherence
that is more pronounced due to the slower Rabi frequency. The decoherence rate is consistent with
magnetic field fluctuations of 1.5 mG measured independently in the lab, which would produce a
Zeeman shift of ~ 3 kHz.

Combining the axial and radial cooling results, a single Na atom is in the 3D ground state with
a probability of 93.5(7) % after RSC. The cooling efficiency is limited by spontaneous scattering
rate $(0.1 - 0.2$ kHz) from the Raman beams, as well as spectral broadening from magnetic field
fluctuations.

We measure a heating rate that corresponds to decreasing 3D ground state population at a rate of
~ 0.9 %/ms. The rate is consistent with off-resonant scattering of the trapping light [14], and is
predominantly in the axial direction where the trapping beam propagates.

Monte-Carlo simulations show that the ground state probability after RSC could be enhanced

by increasing the detuning of the Raman beams and implementing better control of the magnetic field. Another improvement could come from grey molasses cooling, to achieve a lower starting temperature before RSC [15].

3.11 Summary and Outlook

We have shown that despite the difficulty in achieving a low optical cooling temperature of low mass sodium atoms, three dimensional cooling with significant ground state population can be achieved by using high-order Raman sidebands in an optimized cooling sequence. The challenges we face with the cooling of Na atom is shared with a large variety of other systems including exotic atoms and molecules, where the initial temperature and available trapping potential may be limited. The techniques we used are well-suited for these systems and open up a route to ground state cooling.

In our experiment, the RSC step concludes our full control of the atom quantum states. The atoms are then merged into the same trap adiabatically so that they remains in a single quantum state [11]. This is the starting point for our study of the atom-atom interaction and molecular potentials, as well as the coherent formation of molecules. These will be the focus of the following chapters.

4

Interaction of Single Atoms

4.1 Introduction

4.2 Two Interacting Atoms in Optical Tweezer

The Hamiltonian for two atoms in an harmonic potential with interaction is,

$$H = \sum_{i=x,y,z} \left(\frac{m_1 \omega_{1,i}^2 r_{1,i}^2}{2} + \frac{p_{1,i}^2}{2m_1} \right) + \sum_{i=x,y,z} \left(\frac{m_2 \omega_{2,i}^2 r_{2,i}^2}{2} + \frac{p_{2,i}^2}{2m_2} \right) + V_{\text{int}}(\mathbf{r}_1 - \mathbf{r}_2) \qquad (4.1)$$

where m_j is the mass of the j-th atom, $r_{j,i}, p_{j,i}, \omega_{j,i}$ are the coordinate, momentum and trapping frequency for the j-th atom along the i-th axis. V_{int} is the interaction potential between the two atoms which is only a function of the relative coordinate between the atoms $\mathbf{r}_1 - \mathbf{r}_2$.

Since the two atoms experience the same trapping light field, their trapping potential has the same center and the same shape. However, due to the difference in the polarizability between the atoms, the trap depth can be different. Nevertheless, in our experiment, depending on the trapping wavelength, we have $\omega_{1,i} \approx \omega_{2,i}$ to within 10 % to 20 % and this is the regime we will mainly focus on in this section.

In order to calculate the interaction term, we can change from the coordinates for the two indi-

vidual atoms to the center of mass (COM) and relative coordinates.

$$R_i = \frac{m_1 r_{1,i} + m_2 r_{2,i}}{m_1 + m_2} \qquad\qquad r_{\text{rel},i} = r_{1,i} - r_{2,i}$$

$$P_i = p_{1,i} + p_{2,i} \qquad\qquad p_{\text{rel},i} = \frac{m_2 p_{1,i} - m_1 p_{2,i}}{m_1 + m_2}$$

The corresponding masses and trapping frequencies are,

$$M = m_1 + m_2 \qquad\qquad \mu = \frac{m_1 m_2}{m_1 + m_2}$$

$$\Omega_i^2 = \frac{m_1 \omega_{1,i}^2 + m_2 \omega_{2,i}^2}{m_1 + m_2} \qquad\qquad \omega_{\text{rel},i}^2 = \frac{m_2 \omega_{1,i}^2 + m_1 \omega_{2,i}^2}{m_1 + m_2}$$

and the Hamiltonian can be expressed as,

$$H = \sum_{i=x,y,z} \left(\frac{M\Omega_i^2 R_i^2}{2} + \frac{P_i^2}{2M} \right) + \left[\sum_{i=x,y,z} \left(\frac{\mu \omega_{\text{rel},i}^2 r_{\text{rel},i}^2}{2} + \frac{p_{\text{rel},i}^2}{2\mu} \right) + V_{\text{int}}(\mathbf{r}_{\text{rel}}) \right]$$

$$+ \sum_{i=x,y,z} \mu \left(\omega_{1,i}^2 - \omega_{2,i}^2 \right) R_i r_{\text{rel},i} \tag{4.2}$$

The first term and the second term only relies on the COM motion and relative motion respectively

and can be solved independently. The third term mixes the COM and relative motion and is pro-

portional to the trapping frequency difference. If the trapping frequencies are the same for the two

atoms, the third term is 0 and the solution is fully separateable. As mentioned above, since the trap-

ping frequencies for the two atoms are similar, we will assume the mixing term is small and treat it as

a small correction in the calculation.

The interaction potential V_{int} is the original for the molecular bound states and its exact form will be discussed in chapter 5, 6 and 7. However, since the range of the potential is much smaller than the size of the atomic wavefunction, we can ignore the short range details of the potential and treat it as a contact interaction characterized only by the scattering length a [16],

$$V_{\text{int}}(\mathbf{r}) = \frac{2\pi\hbar^2 a}{\mu} \delta_{\text{reg}}(\mathbf{r})$$

where $\mu = m_1 m_2/(m_1 + m_2)$ is the reduced mass and $\delta_{\text{reg}}(\mathbf{r}) \equiv \delta^{(3)}(\mathbf{r})(\partial/\partial r)r$ is the regularized delta-function. The validity of the pseudo-potential is characterized by the ratio of the van der Waals length $\beta_6 = (2\mu C_6/\hbar^2)^{1/4}$ to the relative harmonic oscillator lengths $\beta_{\text{rel},i}$ [17, 18]. In our experiment, these are $\beta_6 \approx 6$ nm, $\beta_{\text{rel},x} \approx \beta_{\text{rel},x} \approx 66$ nm for the radial axes, and $\beta_{\text{rel},z} \approx 158$ nm for the axial axis.

4.2.1 Perturbative Calculation

For weak interaction, i.e. a small scattering length a, the effect of the interaction on the energy level can be calculated perturbatively. The result from this calculation is useful for checking the validity of the full calculation, as well as providing an intuitive understanding of the shift and its dependency on different parameters.

For simplicity, we will assume all the trapping frequencies are the same, i.e. $\omega_{1,i} = \omega_{2,i} = \omega_{\text{rel},i} =$

$\Omega_i = \omega_i$, so that we only need to consider the relative motion,

$$H_{\text{rel}} = \sum_{i=x,y,z} \left(\frac{\mu \omega_i^2 r_{\text{rel},i}^2}{2} + \frac{p_{\text{rel},i}^2}{2\mu} \right) + V_{\text{int}}(\mathbf{r}_{\text{rel}})$$

When treating the interaction as perturbation, the base solution is the harmonic oscillator states for the relative motion $|n_{\text{rel},x}, n_{\text{rel},y}, n_{\text{rel},z}\rangle$. The energy level pertubation is then,

$$
\begin{aligned}
\Delta_{n_{\text{rel},x},n_{\text{rel},y},n_{\text{rel},z}} &= \langle n_{\text{rel},x}, n_{\text{rel},y}, n_{\text{rel},z} | V_{\text{int}}(\mathbf{r}_{\text{rel}}) | n_{\text{rel},x}, n_{\text{rel},y}, n_{\text{rel},z} \rangle \\
&= \frac{2\pi\hbar^2 a}{\mu} \langle n_{\text{rel},x}, n_{\text{rel},y}, n_{\text{rel},z} | \partial_{reg}(\mathbf{r}_{\text{rel}}) | n_{\text{rel},x}, n_{\text{rel},y}, n_{\text{rel},z} \rangle \\
&= \frac{2\pi\hbar^2 a}{\mu} \left| \psi_{n_{\text{rel},x},n_{\text{rel},y},n_{\text{rel},z}}(0) \right|^2
\end{aligned}
\tag{4.3}
$$

where $\left| \psi_{n_{\text{rel},x},n_{\text{rel},y},n_{\text{rel},z}}(0) \right|^2$ is the probability density for zero distance between the atoms.

For the motional ground state, the shift is,

$$\Delta_{0,0,0} = a \frac{2\hbar^2}{\mu\sqrt{\pi}} \prod_{i=x,y,z} \frac{1}{\beta_{\text{rel},i}}$$

where $\beta_{\text{rel},i} \equiv \sqrt{\hbar/\mu\omega_{\text{rel},i}}$ is the relative motion oscillator length along the i-th axis. The shift is proportional to the strength of the interaction a, and is also stronger for stronger confinement where the wavefunction density is higher.

We can see from Eq. 4.3 that the shift is only non-zero when all of $n_{\text{rel},i}$'s are even. The shift is also smaller for higher motional excited state with smaller wavefunction density. This means that

69

the shift will only be observable if the atom is cooled to closed to the motional ground state and will be small or zero for hot atoms.

4.2.2 Non-perturbative Calculation

The first order perturbative result breaks down for large a when the energy shift approaches the motional energy scale $\omega_{\mathrm{rel},i}$. Moreover, due to the divergence nature of the delta-function in the contact interaction potential, higher order perturbative calculation does not converge. It is therefore necessary to use a non-perturbative solution of the interacting atoms in order to interpret measurement of the shift for strong interaction. To do this, we first ignore the last term in the Hamiltonian 4.2 so that it is fully separable into COM and relative motion.

For the relative Hamiltonian, we use the analytic cylindrical solutions from Ref. [19]. These solutions require the potential to be cylindrically symmetric and that the ratio between the radial trapping frequency and the axial trapping frequency $\eta \equiv \omega_{\mathrm{radial}}/\omega_z$ to be an integer. We therefore define $\eta = 6$, which is close to the actual values of 5.6 and ignores the 7 % difference between the two radial trapping frequencies in order to use these solutions. These differences from the real Hamiltonian will be included later, together with the mixing term, as a correction [20, 21]. The analytic solutions are only given for the interacting states, but there also many relative states which have zero wavefunction at the ∂-function, and therefore are unaffected. We have identified these states from the perturbative calculation in section 4.2.1 which are states with $l \neq 0$ or odd m_z after transforming to the cylindrical coordinate used by the analytic solution, where l is the angular momentum quantum numbers for the radial part, and m_z is quantum number for 1D harmonic

oscillator for the axial part. The complete basis includes both the interacting states from Ref. [19] as well as all of the non-interacting states. The non-interacting states are solutions to the cylindrical harmonic oscillator, and so are just cylindrical harmonic oscillator wavefunctions with eigenenergies

$$\frac{E_{n,l,m_z}}{\hbar\omega_z} = (2n + |l| + 1)\eta + (m_z + 1/2) \tag{4.4}$$

where n is the principle quantum number for the radial part. In order to find the non-interacting wavefunction, we need to remove the interaction wavefunction from the cylindrical harmonic oscillator wavefunctions. The complication in this process is that when η is an integer, as is required by the solution of the interaction, there is a subspace of cylindrical harmonic oscillator states with $l = 0$ and even m_z that are degenerate from Eq. 4.4. In each degenerate subspace with N_{deg} states, the non-interacting states $\psi_{\text{non-int}}$ are a linear superposition of the degenerate eigenstates ψ_i that satisfies the condition $V_{\text{int}}\psi_{\text{non-int}} = 0$ or $\psi_{\text{non-int}}(\mathbf{r}_{\text{rel}} = 0) = 0$. We find these amplitudes c_i using a Gram-Schmidt procedure, which from the requirement $\sum_{i=1}^{N_{\text{deg}}} c_i \psi_i(\mathbf{r}_{\text{rel}} = 0) = 0$. In each subspace, there is only one interacting state, for which the analytic solution is used, and $N_{\text{deg}} - 1$ non-interacting states.

For the interacting states, the energies are given by the transcendental equations [19]

$$\mathcal{F}\left(-\frac{(E - E_0)}{2}, \eta\right) = -\frac{\sqrt{2\pi}}{a}$$

where $\mathcal{F}(x, \eta)$ is given by

$$\mathcal{F}(x, \eta) = \frac{\sqrt{\pi}\Gamma(x)}{\Gamma(x + \frac{1}{2})} \sum_{m=1}^{n-1} F\left(1, x; x + \frac{1}{2}; e^{i(2\pi m/\eta)}\right) - \frac{2\sqrt{\pi}\Gamma(x)}{\Gamma(x - \frac{1}{2})}$$

Here $F(a, b; c, x)$ denotes the hypergeometric function and $\Gamma(x)$ is the Euler gamma function. The energy E and E_0 are in units of the axial trapping frequency ω_z, and so the ground state energy $E_0 = \eta + 1/2$.

The COM Hamiltonian is a cylindrical harmonic oscillator and the energies is given by Eq. 4.4.

Now that we have the solution in the separable and cylindrical case, the next step is to include the non-separable and asymmetric correction terms by diagonalizing the total matrix in the combined COM and relative cylindrical bases. Compared to treating the interaction term in Eq. 4.1 as a perturbation, the correction terms included here all have the form of harmonic potentials and therefore have much better convergence behavior. We include all states with energies up to $20\omega_{\mathrm{rel},z}$ in the calculation. The matrix elements are calculated numerically using the cylindrical wavefunctions, which for completeness are given here:

$$\Psi_{n,l,m_z}(\rho, \theta, z) = \Psi_{n,l}^{\mathrm{radial}}(\rho, \theta)\Psi_{m_z}^{\mathrm{axial}}(z)$$

with the normalized radial harmonic oscillator wavefunction,

$$\Psi_{n,l}^{\mathrm{radial}}(\rho, \theta) = \sqrt{\frac{2n!}{a_\perp^2 (n + |l|)!}} e^{-r^2/(2a_\perp^2)} \left(\frac{r}{a_\perp}\right)^{|l|} L_n^{|l|}\left(\frac{r^2}{a_\perp^2}\right) \frac{e^{il\theta}}{\sqrt{2\pi}}$$

Figure 4.1: Energy levels as a function of scattering length (in unit of the axial relative motion oscillator length $\beta_{\mathrm{rel},z}$) from the non-perturbative calculation. The dashed straight light is the result from first order perturbation for the motional ground state which shows good agreement with the exact calculation at small scattering length. Only states that are in the radial motional (both relative and COM) ground state are shown because of the high radial motional energy scale ($100\,\mathrm{kHz}$). The states are labeled with their relative and COM axial motional quantum numbers $m_{\mathrm{rel},z}$ and $m_{\mathrm{COM},z}$. Due to the relative and COM motion mixing term and the resulting avoided crossings in the energy levels, these are not true quantum number and are not constants along the same line. The number shown in the plot are for the state at large negative scattering length. States with even total parity, i.e. $m_{\mathrm{rel},z} + m_{\mathrm{COM},z}$, are plotted in solid lines whereas ones with odd total parity are plotted in dashed lines. Since the Hamiltonian conserves total parity, there is no coupling between the between the two sets of states which results in the level crossing shown in the plot.

and the normalized 1D harmonic wavefunction,

$$\Psi_{m_z}^{\text{axial}}(z) = \frac{1}{\sqrt{2^{m_z} m_z!}} \frac{1}{\sqrt{a_z}(\pi)^{1/4}} e^{-z^2/(2a_z)} H_{m_z}(z/a_z)$$

Here the radial and axial oscillator lengths are defined as $a_\perp = \sqrt{\hbar/(\mu\omega_\perp)}$ and $a_z = \sqrt{\hbar/(\mu\omega_z)}$. H_{m_z} are the Hermite-Gaussian functions, and $L_n^{|l|}$ are the generalized Laguerre polynomials.

The eigenenergies of the matrix are calculated as a function of the scattering length. The results for the lowest energy ones are shown in Fig. 4.1.

4.3   Interaction Shift Spectroscopy

4.3.1   Experiment Sequence

The absolute energies shown in Fig. 4.1 have an arbitrary global offset and are therefore not directly measurable. Instead, the measurable quantities are the energy differences between different states, which can be done either by changing the scattering length, i.e. moving along the x axis, or by changing the motional state of the atoms, i.e. moving along the y axis.

In our experiment, we measure the interaction shifts by flipping the spin state of one but not the other atom using Raman transition. Since the scattering length depends on the spin state, this allow us to measure the difference between energy levels for different scattering lengths by comparing the resonance frequency in the absence of the other atom (Fig. 4.2). The spin flip is done in the same 8.8 G we use for Raman sideband cooling (section 3.4). We drive the transition using two Raman beams that are co-propagating which imprints no phase gradient on the atomic wavefunction (sec-

Figure 4.2: Schematics of interaction shift spectroscopy using Raman transitions. Left: Raman resonance for atomic spin flip with only one atom in the tweezer. Right: The energy shifts by a spin state dependent amount with the present of the second (red) atom. This causes a shift in the spin flip resonance frequency for the first (green) atom compared to the one atom case. The shift corresponds to the difference in the interaction shift between the two spin states.

tion 3.2.1). This reduces the number of observable resonances and provides a cleaner spectrum since,

1. Parity is conserved during the transition.
   Starting from the motional ground state, this means that all dashed lines in Fig. 4.1 are uncoupled.

2. Coupling to different motional states are surpressed.
   In particular, this reduces the coupling to COM motional excitation in the strong interaction limit. Note that since the interaction between the atoms modifies the wavefunction, there is still non zero overlap between different motional states especially for the relative motion.

Figure 4.3: Interaction shift measurement for (A) $\left|\mathrm{Na}(2,2),\mathrm{Cs}(4,4)\right\rangle \rightarrow \left|\mathrm{Na}(2,2),\mathrm{Cs}(3,3)\right\rangle$ and (C) $\left|\mathrm{Na}(2,2),\mathrm{Cs}(3,3)\right\rangle \rightarrow \left|\mathrm{Na}(1,1),\mathrm{Cs}(3,3)\right\rangle$ with the corresponding transition shown on the energy map from theoritical calculation in (B) and (D) respectively. The orange line shows the bare resonance with only one atom in the trap and the blue line shows the spectrum including interaction shift. A resonance appears at positive frequency shift corresponds to the final state having a more positive energy (more repulsive interaction or higher motional energy). More than one shifted peaks can be observed due to the motional state mixing caused by the interaction. The corresponding motional state is marked as $\left|m_{\mathrm{rel},z},m_{\mathrm{COM},z}\right\rangle$ on the resonance. For the $\left|\mathrm{Na}(2,2),\mathrm{Cs}(3,3)\right\rangle \rightarrow \left|\mathrm{Na}(1,1),\mathrm{Cs}(3,3)\right\rangle$ transition (C and D), the states with two quanta of total axial excitation are unresolved. Since the Raman transition preserves parity, only states with even parity are shown in (B) and (D).

76

Table 4.1: Interaction shift and scattering lengths for different spin states. The number for the $|\mathrm{Na}(2,2),\mathrm{Cs}(4,4)\rangle$ is computed from the binding energy of the molecular state whereas the other numbers are measured by the interaction spectroscopy.

Spin state	Interaction Shift (kHz)	Scattering Length
$|\mathrm{Na}(2,2),\mathrm{Cs}(4,4)\rangle$	1.40	$30.4a_0$
$|\mathrm{Na}(2,2),\mathrm{Cs}(3,3)\rangle$	-30.7	$-693.8a_0$
$|\mathrm{Na}(1,1),\mathrm{Cs}(3,3)\rangle$	0.62	$13.7a_0$

4.3.2 RESULTS

The spectrum for the $|\mathrm{Na}(2,2),\mathrm{Cs}(4,4)\rangle$ to $|\mathrm{Na}(2,2),\mathrm{Cs}(3,3)\rangle$ transition is shown in Fig. 4.3A.

The orange line shows the bare $|\mathrm{Cs}(4,4)\rangle$ to $|\mathrm{Cs}(3,3)\rangle$ resonance without the present of the Na

atom whereas the blue line shows the resonances including the interaction with the Na atom. The

largest peak on the left is the shifted ground motional state $|m_{\mathrm{rel},z},m_{\mathrm{COM},z}\rangle = |0,0\rangle$ and the

smaller peak on the right corresponds to the $|2,0\rangle$ state (Fig. 4.3B). A even smaller resonance for

$|4,0\rangle$ is also visible further right (not shown in Fig. 4.3B). The $|0,0\rangle$ resonance gives the difference

of the interaction shifts of the initial and final spin states, $E(\mathrm{Na}(2,2),\mathrm{Cs}(3,3))-E(\mathrm{Na}(2,2),\mathrm{Cs}(4,4)) =$

$-32.1(2)\mathrm{kHz}$. The peak near zero frequency corresponds to the initial Na and Cs population

that is not prepared in the motional ground state or an interacting state. The fitted height 0.46

of the $|0,0\rangle$ peak serves as a lower bound for the relative motional ground-state population. Sim-

ilarly, Fig. 4.3C shows the result for the $|\mathrm{Na}(2,2),\mathrm{Cs}(3,3)\rangle$ to $|\mathrm{Na}(1,1),\mathrm{Cs}(3,3)\rangle$ measured by

driving a Na Raman transition. Two interaction shifted resonances were observed which corre-

sponds to the motional ground state and unresolved states with two total Na and Cs motional ex-

citation (Fig. 4.3D).

Since the measurement only give the energy difference between different scattering lengths, we determine an absolute interaction shift of the $|\text{Na}(2,2), \text{Cs}(4,4)\rangle$ using the binding energy of the least bound state $v'' = -1$ (section 6.2.2). The absense of spin mixing for this state allows its binding energy to be related to the scattering length directly through the single-channel quantum defect theory (QDT) [22, 23, 24] but extended to two-scale by including the $-C_8/r^8$ potential. For the van der Waals coefficients, we use $C_6 = 3227$ a.u. and $C_8 = 3.681 \times 10^5$ a.u. from Refs. [25, 26, 27]. From here, we can use the result of the calculation above to obtain all the absolute interaction shifts and scattering lengths. The final result for all the spin states is summarized in table 4.1.

4.4   Summary and Outlook

Optical tweezer provides a clean platform to study the interaction between exactly two atoms. Here, we started our exploration of the interaction by measuring the most important quantity for s-wave scattering process at ultracold temperature, the scattering length a. The results from these measurement can be used to refine theory model of the NaCs molecule, including predictions of the molecule binding energy and Feshbach resonances [28]. More properties of the interaction will be studied in the following chapters.

Additionally, the combination of the tight confinement from the optical tweezer and the interaction between the atoms also give us further control on the motional states of the atom. As we have seen in this chapter, the degeneracy of carrier Raman transition for different motional state is lifted by the interaction. As a result, driving on the $|0,0\rangle \rightarrow |0,0\rangle$ interaction shifted resonance allow us

to prepare a system that is completely in the ground state of the relative motion. This will be used when we coherently create the molecules (chapter 7) to lower the requirement for the cooling and reduce the background caused by hot atoms.

5

Photoassociation of Single Atoms

5.1 INTRODUCTION

The method we use to coherently create a single molecule from atoms uses two-photon optical transition (chapter 7). Before we can drive such a transition, however, we must locate and characterize the intermediate excited states of the molecule to be used in the two-photon transition. This can be measured using photoassociation (PA) spectroscopy where two atoms are driven from the atomic

state to an excited molecular state via an optical transition. The flexibility of the optical tweezer plat-

form allows us to prepare a clean initial state with only two atoms as well as accurately detect when

PA has happened with high signal to noise ratio (section 5.3.2).

In this chapter, we describe the molecular energy structure (section 5.2) and how we use PA spec-

truscopy to locate and identify the molecular excited states (section 5.3). We also details the beam-

path for the measurement (section 5.3.1) including the alignment procedure for the PA beam and

discussions about factors that can affect the PA linewidth (section 5.3.3).

5.2 Energy Levels

First we will discuss the energy levels in a diatomic molecule as well as the labeling system for the

states. We will focus mainly on the electronic excited states measured in this chapter but most of the

discussion here applies to ground electronic states as well and will be useful for chapter 6 and 7.

5.2.1 Angular Momentums

Compared to an atom, a diatomic molecule has many more degrees of freedoms. In additional to

the quantum numbers for each atom in the molecule, molecules also have nuclear motion. In or-

der to reduce the complexity, it is therefore very important to consider the symmetry of the system,

and in particular the angular momentums, which corresponds to rotation symmetry, and the cou-

pling between them. The angular momentums in a diatomic molecule includes electron orbit $\mathbf{L}$ [*],

---

[*]There are $\mathbf{L}_1$ and $\mathbf{L}_2$ for the two electron but since we only consider states with at most one $\mathbf{L}_i \neq 0$ we will only use one quantum number here
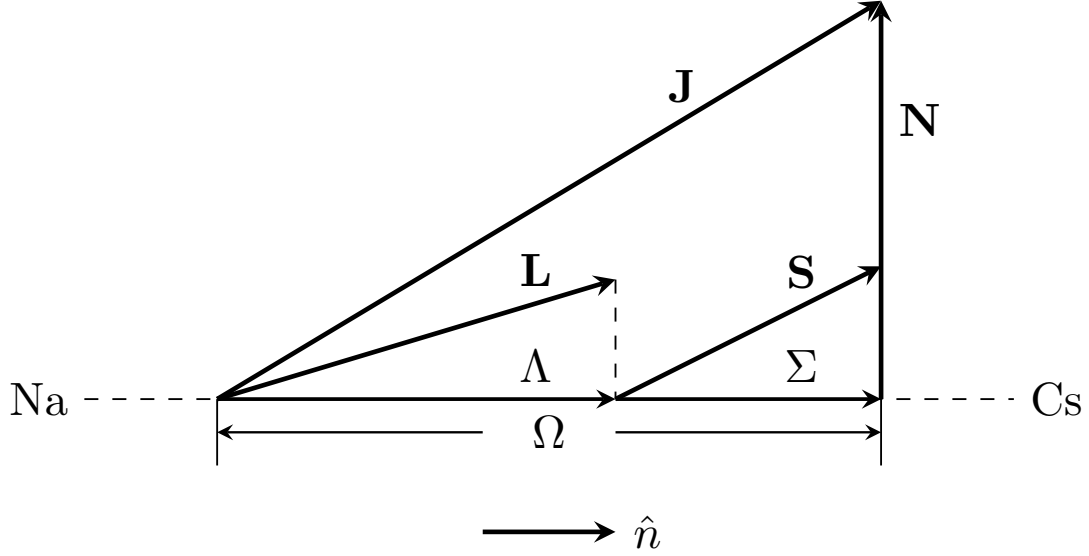
Figure 5.1: Angular momentum coupling for *Hund's case (a)*. $\mathbf{L}$ and $\mathbf{S}$ are coupled to the internuclear axis $\hat{n}$ and the sum of the projections $\Omega = \Lambda + \Sigma$ is then added with the orthogonal compoment $\mathbf{N}$ to form $\mathbf{J}$.

electron spin $\mathbf{S}_1$ and $\mathbf{S}_2$, nuclear orbital $\mathbf{N}$ and nuclear spin $\mathbf{I}_1$ and $\mathbf{I}_2$. Although the total angular momentum $\mathbf{F} \equiv \mathbf{L} + \mathbf{S}_1 + \mathbf{S}_2 + \mathbf{N} + \mathbf{I}_1 + \mathbf{I}_2$ is the only true conserved quantity in the absence of external field, depending on the coupling strengths between the angular momentums, there are additional approximately conserved quantity in the molecule.

For the NaCs molecule and our experiment, there are two important regimes where the coupling strength can be easily ordered.

5.2.1.1   Deeply Bound States

This is described by the *Hund's case (a)* [29, p. 523-626]. Molecular states with large binding energies mostly experience interactions between the atoms at short range where the electric static interaction is very strong. This couples the the two electron spins into a total electron spin $\mathbf{S} \equiv \mathbf{S}_1 + \mathbf{S}_2$ via

a very strong effective interaction of the form $\mathbf{S}_1 \cdot \mathbf{S}_2$ which originates from the resulting symmetry of the electron orbital wavefunction. Similar to atoms, the nuclear spin interaction is also very week compared to other energy scales so we can ignore the hyperfine structure and only need to consider $\mathbf{J} \equiv \mathbf{L} + \mathbf{S} + \mathbf{N}$.

The strong electrostatic interaction also creates an effective coupling between the $\mathbf{L}$ and $\mathbf{S}$ with the internuclear axis $\hat{n}$ causing $\mathbf{L}$ and $\mathbf{S}$ to process rapidly around $\hat{n}$. This creates two new conserved quantity Λ and Σ as the projection of $\mathbf{L}$ and $\mathbf{S}$ along $\hat{n}$ respectively. The total angular momentum along $\hat{n}$ is therefore $\Omega \equiv \Lambda + \Sigma$ and it is added to the $\mathbf{N}$ which is orthogonal to $\hat{n}$ to form the total angular momentum $\mathbf{J}$ (Fig. 5.1).

The angular momenum state of the molecule is therefore fully characterized by $|L, \Lambda, S, \Omega, J\rangle$. Λ can be $0, 1, \ldots, L$, Ω ranges from $|\Lambda - S|$ to $\Lambda + S$ and $J \geqslant \Omega$. The L quantum number is specified by the electronic state and will be discussed in section 5.2.2 and the rest of the angular momentum quantum numbers are represented by the *Hund's case (a)* term symbol,

$$^{2S+1}\Lambda_\Omega$$

similar to the atomic term symbol $^{2S+1}L_J$. Just as the use of capital English letters $S, P, D, \ldots$ to represent $L = 0, 1, 2, \ldots$, capital Greek letters $\Sigma, \Pi, \Delta, \ldots$ are used to denote $\Lambda = 0, 1, 2, \ldots$ in the term symbol. An additional symmetry to consider is the reflection about a plane that includes the internuclear axis. For $\Lambda > 0$ states, the reflection produces a new state at the same energy creating the so-called Λ-doubling. For $\Lambda = 0$ states, i.e. Σ states, the reflection produces the same state with

a phase of ± 1. This phase is also included in the term symbol to fully specify the symmetry of a Σ states as

$$^{2S+1}\Sigma_\Omega^\pm$$

Note the Σ state here should not be confused with the quantum number Σ.

From the angular momentum relation in Fig. 5.1, we can also determine the energies of different rotational states. The nuclear rotational energy is given by,

$$E_{rot} = B\langle \mathbf{N}^2 \rangle$$

where B is the rotational constant of the molecule. For *Hund's case (a)* this is,

$$\begin{aligned} E_{rot} &= B\langle \mathbf{J}^2 - \Omega^2 \rangle \\ &= B\langle \mathbf{J}^2 - \Omega^2 \rangle \\ &= B\big(J(J+1) - \Omega^2\big) \end{aligned}$$

For the last step, note that Ω is not an angular momentum vector but a projection. We can easily see that for a given Ω, we have $J \geqslant \Omega$. Unlike a rigid rotor where $E_{rot} = BN(N+1)$, the limit on the J means that the spacing between the rotational levels depend on Ω,

$$2\Omega + 2, \ 2\Omega + 4, \ 2\Omega + 6, \ \ldots$$

This allows us to determine the Ω of the state we are addressing by measuring the state spacing for the lowest few rotational states.

5.2.1.2 Near Threshold Bound States

For molecular states with small binding energy, the interaction between the two atoms is small compared to the internal coupling in the atoms and the angular momentum coupling is "atom like". In this limit, the total angular momentum $\mathbf{F}_1$ and $\mathbf{F}_2$ for the individual atoms forms $\mathbf{F}_{\text{atom}} = \mathbf{F}_1 + \mathbf{F}_2$ which is then coupled to the nuclear rotation $\mathbf{N}$ to form $\mathbf{F} = \mathbf{F}_{\text{atom}} + \mathbf{N}$. We will discuss this regime in more detail when we characterize the weakly bound ground states in chapter 6.

5.2.2 Potential Energy Surface

Due to the different angular momentum coupling in different regimes, there is not a consistent way to label the interaction between the two atoms at both short and long distance. Nevertheless, by convention, we use the *Hund's case (a)* term symbol since it more accurately represents the state when the interaction energy dominates.

The Hamiltonian (excluding spin for simplicity[*]) is,

$$H = H_e + T_n$$

<hr>

[*]Electron spin is implicitly included, however, via the symmetry of the electronic wavefunction.

where the electronic term H_e and the nuclear kinetic term T_n are given by

$$H_e = -\sum_i \frac{\hbar}{2m_e}\nabla_i^2 + \frac{e^2}{4\pi\varepsilon_0}\left(\sum_{i>j}\frac{1}{|\mathbf{r}_i - \mathbf{r}_j|} - \sum_{A=\text{Na,Cs}}\sum_i \frac{Z_A}{|\mathbf{r}_i - \mathbf{R}_A|} + \frac{Z_{\text{Na}}Z_{\text{Cs}}}{|\mathbf{R}_{\text{Cs}} - \mathbf{R}_{\text{Na}}|}\right) \quad (5.1)$$

$$T_n = -\sum_{A=\text{Na,Cs}}\frac{\hbar^2}{2m_A}\nabla_A^2$$

and the sum is over all the electrons in the molecule.

5.2.2.1 Born-Oppenheimer Approximation

The Hamiltonian is solved using the Born-Oppenheimer (BO) approximation. Because of the large mass difference between the nuclei and the electrons, we can assume that the electron motion follows the position of the nuclei instantaneously so that the motion of the nuclei and the elctrons can be treated separately. Formally, this mean that the electron wavefunctions is solved using the electrionic term H_e for a given nuclear position $\mathbf{R}_{\text{Na}}$ and $\mathbf{R}_{\text{Cs}}$. This results in an effective potential $V_{\text{eff}}(|\mathbf{R}_{\text{Na}} - \mathbf{R}_{\text{Cs}}|)$ called the potential energy surfaces (PES) for each electronic states. The solutions to the approximate Hamiltonians $T_n + V_{\text{eff}}$ provide the vibrational and rotational states of the molecule.

5.2.2.2 Franck-Condon Factor

In additional to the energy of the molecular bound state, the solution of the nuclear motion also provides information to the selection rules and coupling strength of transitions between the states. For an electronic electric dipole transition between state $|e_1, v_1, j_1\rangle$ and $|e_2, v_2, j_2\rangle$, where e_i, v_i and

j_i denotes electronic, vibrational and angular momentum states, the Rabi frequency under the BO approximation is,

$$\Omega = \langle e_1, v_1, j_1 | e\mathbf{r}_e \cdot \mathbf{E}e^{i\mathbf{k}\cdot\mathbf{r}} | e_2, v_2, j_2 \rangle$$

$$= \langle e_1(\mathbf{r}) | e\mathbf{r}_e \cdot \mathbf{E} | e_2(\mathbf{r}) \rangle \langle v_1, j_1 | e^{i\mathbf{k}\cdot\mathbf{r}} | v_2, j_2 \rangle$$

where $\mathbf{r}$ and $\mathbf{r}_e$ are the molecule and electron coordinates. For most of the transitions, we can treat the nuclear coordinate dependent transition dipole moment $\mathbf{D}(\mathbf{r}) \equiv \langle e_1(\mathbf{r}) | e\mathbf{r}_e | e_2(\mathbf{r}) \rangle$ as a constant $\mathbf{D}$. Since the size of the molecular wavefunction is also usually much smaller than the wavelength of the transition, we can also assume $e^{i\mathbf{k}\cdot\mathbf{r}} \approx 1$, we have,

$$\Omega = \mathbf{D} \cdot \mathbf{E} \langle j_1 | j_2 \rangle \langle v_1 | v_2 \rangle$$

The term $\langle j_1 | j_2 \rangle$ determines the angular momentum selection rule which is $\Delta\Lambda = 0, \pm 1, \Delta S = \Delta\Sigma = 0, \Delta\Omega = 0, \pm 1$ and $\Delta J = 0, \pm 1$ for *Hund's case (a)* [30, p. 14-15]. The term $\langle v_1 | v_2 \rangle$ gives the coupling strength between vibrational states [*]. This is called the Franck-Condon principle and the square of the wavefunction overlap is defined as the Franck-Condon factor (FCF),

$$\text{FCF} \equiv |\langle v_1 | v_2 \rangle|^2$$

---

[*]Note that $\langle v_1 | v_2 \rangle$ does not simplify to orthogonality relation when $e_1 \neq e_2$ since the vibrational wavefunctions belongs to different PES.

Figure 5.2: Potential energy surfaces of NaCs with *Hund's case (a)* labels. Due to spin-orbit coupling, the potentials are not independent of each other. The real energy eigenstates of the molecule may be a superposition of multiple electronic and spin states.

For incoherent transition, the transition rate is proportional to $\Omega^2 \propto$ FCF.

5.2.2.3 ENERGY LEVELS OF NACS

Fig. 5.2 shows the relevant PESs for NaCs. Although the spin-less electronic Hamiltonian 5.1 makes it easier to understand the molecule structure and provides good approximations for the transition dipoment and FCF, the absense of spin and the difficulty in exactly solving a multi-electron system makes it unsuitable to calculate energy levels for spectroscopy purpose. Because of this, prediction

of the molecular states energies are calculated using PESs fitted to experimental data [25, 31, 32, 33].

5.3 Photoassociation Spectroscopy

5.3.1 Beampath

The excited molecular state we would like to address has a bond length of $3 - 8$ Å. The initial atomic state, however, has an average inter-nuclear distance of ≈ 1000 Å. This size mismatch between the initial and final state wavefunctions means the transition typically have a very small FCF ($10^{-10} - 10^{-8}$). Because of this, we focus our PA beam onto the tweezer with a beam waist between 10 μm and 30 μm (Fig. 5.3) in order to increase the laser intensity and improve the signal contrast. The tight focus also increase the astigmatism when passing through the glass cell window at an angle which limits the minimum focus size we can achieve. Therefore, we added a correction glass plate to fix the astigmatism in order to minimize the focus size and maximize the beam intensity.

In order to align the PA beam to the tweezer, we use the following alignment procedure,

1. Light resonant with the Cs atomic transition is sent into the PA beam path. This allows us to do the alignment using the procedure we used to align the atomic Raman sideband cooling beams as described in section 3.8. However, unlike the alignment for the atomic Raman beams, due to the larger frequency difference between the PA transition and the Cs atomic transition as well as the smaller beamsize, we cannot use the alignment result from this step directly for the PA beam due to the chromatic aberration from the optics in the PA beam path.

2. In order to translate the alignment result from resonance Cs light to that of the PA light, we insert a mirror to reflect the PA beam after the last optics in the beam path and place a beam profiler at the equivalent location of the tweezer (Fig. 5.3). This allow us to directly measure location of the focal point for the two wavelengths and correct for the chromatic aberration
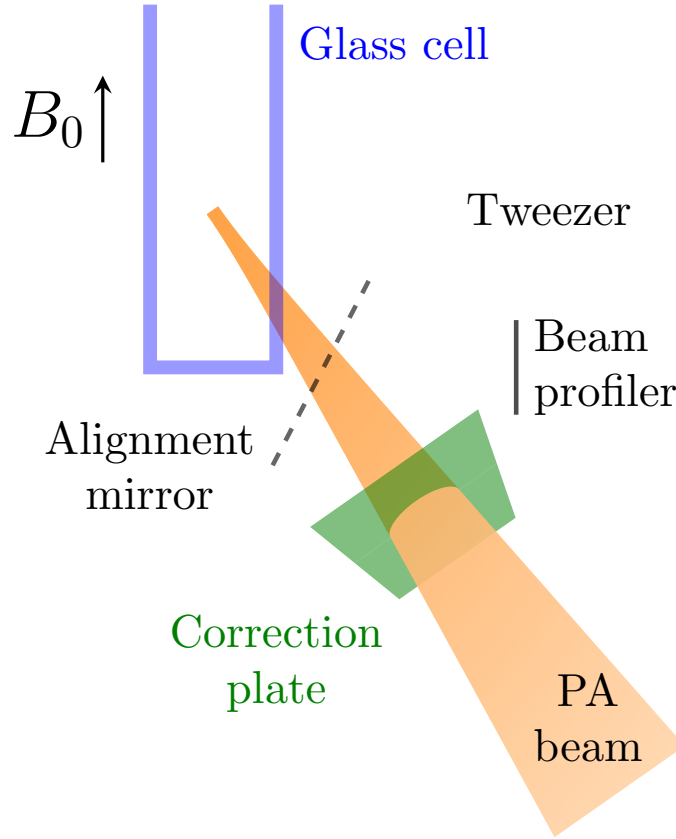
Figure 5.3: PA beampath including the relative geometry with the magnetic field the glass vacuum cell and the tweezer. In order to compensate for the astigmatism from pass through the glass cell window at an angle, we added an correction glass plate into the PA beam path. The correction plate has the same thickness and angle of incident with the glass cell window but is angled vertically instead of horizontally. The alignment mirro and the beam profiler can also be added to the beam path in order to measure the chromatic error during alignment.
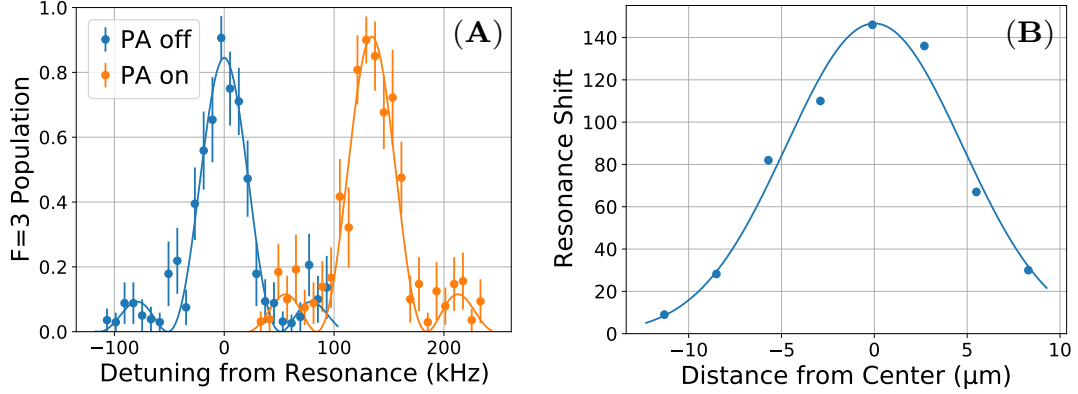
Figure 5.4: Measurement of Cs vector light shift from the PA beam for final alignment. (A) The effective magnetic field from the circularly polarized PA beam causes a shift on the Raman resonance between the $|4, 4\rangle$ and $|3, 3\rangle$ states. (B) Vector light shift as a function of PA beam position used to determine the beam center. The $1/e$ diameter of the beam is measured to be $13.40(72)$ µm.

by shifting the focus from the PA light to the original focus position from the resonance Cs light.

3. As the final alignment step and to correct for the chromatic aberration of the glass window that was not corrected for in the last step, we align the PA beam to the atom using signal directly from the atom. Due to the large detuning, the scattering rate from the PA beams is too low to be used for alignment. However, when the PA beam is set to circular polarization, it creates an effective magnetic field parallel to the beam propagation direction of the form [9],

$$B_{\text{eff}} = -U_0 \frac{\partial_2 - \partial_1}{\partial_2 + 2\partial_1} \mathbf{C}$$

where U_0 is the scalar light shift, ∂_1 and ∂_2 are the detuning from the D$_1$ and D$_2$ line respectively, ε is the polarization vector and $\mathbf{C} \equiv \Im(\varepsilon \times \varepsilon^*)$ qualifies the ellipticity of the polarization with $|C| = 1$ for pure circular polarization and $|C| = 0$ for linear polarization. This effective magnetic field causes a relative shift between the $|4, 4\rangle$ and the $|3, 3\rangle$ states which can be measured using a Raman transition (Fig. 5.4A). By measuring the shift as a function of the beam position, we can determine the size and the center of the PA beam and align the beam to the atom (Fig. 5.4B).

Table 5.1: Prediction of $|\mathrm{Na}(2, 2), \mathrm{Cs}(4, 4)\rangle$ PA resonance frequency based on Dunham expansion [32, 34].

Vibrational State	$v' = 0$	$v' = 12$	$v' = 13$	$v' = 14$
Resonance Prediction (GHz)	288722	306491	307876	309252

5.3.2 EXPERIMENT SEQUENCE AND RESONANCE FREQUENCIES

For the PA spectroscopy, we mainly focus on states with large binding energies which are expected to be good candidates as the intermediate state for Raman transfer (section 7.2). In particular, we scanned the PA light frequency around the $v' = 0$ and $v' = 12 - 14$ vibrational states in the $c^3\Sigma_{\Omega=1}$ potential. Table 5.1 shows the predicted resonance frequencies for the PA resonance from $|\mathrm{Na}(2, 2), \mathrm{Cs}(4, 4)\rangle$ based on fitting to previous measurement [32]. The frequencies are calculated from Dunham expansion [34] corrected for the hyperfine structure for the atoms.

In order to observe PA, we first prepare both the Na and Cs atoms in the motional ground states in the same tweezer [35]. We then turn on the PA beam for a set time followed by separating the atoms into their respective tweezers and image the atoms. When we hit a PA resonance, the excited molecular state will typically decay down to either a molecular ground state, which will remain in at most one of the tweezers after the separation, or an atomic state with high relative motional energy and escape the trap. In either case, this leads to at least one empty tweezer after the separation. By measuring the probability of having both the Na and Cs atoms after the PA pulse conditioned on both atoms being initially loaded, we can capture the probability of PA event and locate the resonances.

The initial atomic state we used is $|\mathrm{Na}(2, 2), \mathrm{Cs}(4, 4)\rangle$ which has $L = 0$ and $S = 1$. For atoms

Figure 5.5: PA spectrum for (A) $v' = 0$, (B) $v' = 12$, (C) $v' = 13$, (D) $v' = 14$. The PA frequency is shown in GHz with an offset. Multiple rotational states can be observed for $v' = 0$ and $v' = 12$. $v' = 0$ also shows multiple peaks that corresponds to the hyperfine structure of the molecule. The $v' = 13$ and $v' = 14$ transitions are relatively weak and only the strongest line is measured as a result.

in the motional ground state we also have $N = 0$ and therefore $J = 1$ which should be coupled to $J = 0, 1, 2$ excited states from the $\Delta J = 0, \pm 1$ selection rule. However, since the cooling is not perfect, we expect some atoms initially in the $N = 1$ state which can allow a weaker transition to the $J = 3$ states. Moreover, since the PA beam polarization is circular and has maximum overlap with the σ^+ polarization, the $J = 2$ is expected to have the strongest coupling.

Fig. 5.5 shows the PA spectra measured for different vibrational states with the frequencies sum-

Table 5.2: PA resonance frequencies for $v' = 0, 12 - 14$. The J numbers for $v' = 0$ and $v' = 12$ are assigned based on the rotational state spacing. For $v' = 13$ and $v' = 14$, we assume the observed line is $J = 2$ which is expected to be have the strongest coupling.

Vibrational State		$v' = 0$	$v' = 12$	$v' = 13$	$v' = 14$
Resonance (GHz)	$J = 1$	288693.3	306492.1	-	-
		288694.3	-	-	-
	$J = 2$	288698.0	306495.9	307879.8	309255.4
		288698.5	-	-	-
	$J = 3$	288705.4	306502.0	-	-

marized in table 5.2. The spectra for $v' = 0$ and $v' = 12$ shows three rotational states whereas only the strongest rotational state is measured for $v' = 13$ and $v' = 14$. The $v' = 0$ spectrum also shows the hyperfine structure for the lowest two rotational states.

The rotational states of the molecule can be determined from the energy gap between the states based on the discussion in section 5.2.1.1. The ratio of the spacing between the lowest J states we measured are 1.64 and 1.61 for $v' = 0$ * and $v' = 12$ respectively. This is very closed to the ratio of $3/2$ for $\Omega = 1$ states. The main source of the deviation is likely the hyperfine structure that was ignored in the discussion above.

5.3.3 LINEWIDTH

In additional to the energy, another property of the excited state that is important for driving a two-photon transition using the state is the linewidth. This determines the scattering or decoherence rate of the two-photon transition which then determines the transfer efficiency (chapter 7). The

---

*The energy of the strongest hyperfine line is used

linewidth, or decay rate, due to electric dipole transitions is [29, p. 197],

$$\Gamma = \sum_i \frac{\omega_i^3 d_i^2 \text{FCF}_i}{3\pi\varepsilon_0 \hbar c^3}$$

where ω_i is the decay frequency, d_i is the transition dipole moment, and the sum is over all the decay channels. Since the size of the excited state electron wavefunction is similar to that of the atom the molecule has a similar transition dipole moment as the corresponding atomic transition $d_i \approx d_{\text{Cs}}$. Moreover, since $\sum_i \text{FCF}_i = 1$ and $\omega_i \approx \omega_{\text{Cs}}$ we have

$$\Gamma \approx \frac{\omega_{\text{Cs}}^3 d_{\text{Cs}}^2}{3\pi\varepsilon_0 \hbar c^3}$$

$$= \Gamma_{\text{Cs}} \approx 2\pi \cdot 5 \text{ MHz}$$

Since the PA laser is locked using a wavemeter with a precision $\approx$ 20 MHz, we expect the PA linewidth we measured to be limited by our frequency resolution.

This is, however, not what is observed in the experiment. Fig. 5.6A shows the narrowest spectrum of the $v' = 12, J = 2$ PA line we measured when the tweezer frequency is set to 306344. GHz with 10 mW of power. The linewidth is determined to be 167(32) MHz which is much greater than the theory prediction.

Furthermore, the observed linewidth appears to be dependent on the tweezer power. The same PA line measured with 1 mW tweezer power is shown in Fig. 5.6B with a significantly narrower linewidth of 27.3(97) MHz. In fact, the linewidth appears to be proportional to the tweezer power

Figure 5.6: Fitting of PA linewidth for (A) $10\ \mathrm{mW}$, (B) $1\ \mathrm{mW}$ tweezer power, showing a broad linewidth and a significant difference between the two. (C) Fitting of the PA linewidth as a function of tweezer power suggests a proportional relation between the two.
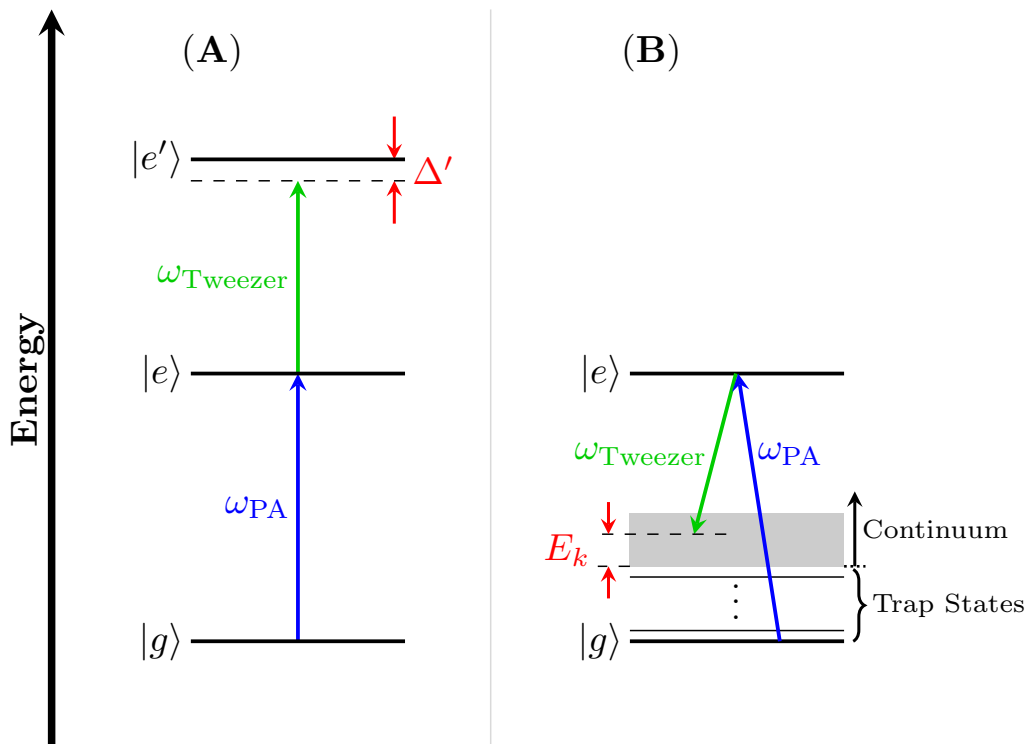
Figure 5.7: Potential two-photon broadening mechanism for PA by coupling the excited state $|e\rangle$ via the tweezer to (A) a higher excited state $|e'\rangle$ or (B) the atomic motional continuum. (A) For coupling to a higher excited state, the broadening depends on the two-photon detuning Δ' from $|e'\rangle$. (B) For coupling to the atomic motional continuum, the broadening is a function of the kinetic energy of the atomic state E_k.

as shown in Fig. 5.6C, which suggests that the linewidth may be broadened by a two-photon process.

We initially suspected that the source of this broadening is due to the tweezer light coupling the excited molecular state to another state at a higher energy (Fig. 5.7A). If this is the case, we would expect the broadening to be a function of the sum of the tweezer and PA light frequency depending on the detuning from the nearest two-photon excited state. However, the broadening does not change significantly when the tweezer frequency is changed by $\approx 10\,\mathrm{GHz}$ and is also observed for

other excited states including $v' = 0$ and $v' = 14$ which have very different resonance frequencies. It is therefore unlikely that this is the broadening mechanism we observe. Instead, we believe the effect is caused by a Λ type two-photon process coupling the excited state to the atomic ground states. In the following section, I will provide an estimation for such a broadening process.

5.3.3.1 Two-Photon Coupling to the Atomic Motional Continuum

The broadening of the PA line requires coupling the excited state to a continuum of states. For the ground atomic state, since the state is stable with repect to radiative decay, this continuum cannot be the photon continuum. Instead, the excited state is coupled to the relative motional continuum of the atoms. Physically, this corresponds to a photodissociation process where the atoms flies away with high kinetic energies corresponding to the detuning of the tweezer (Fig. 5.7B).

The photodissociation rate is determined by the Fermi's golden rule,

$$\Gamma = 2\pi \Omega_{if}^2 \rho_f$$

where Ω_{if} is the matrix element between the initial and final state and ρ_f is the density of state near the final state. We calculate this by first discretizing the continuum and the rate becomes

$$\Gamma = 2\pi \frac{\Omega_{if}'^{\,2}}{\partial}$$

where Ω_{if}' is the Rabi frequency between the initial and final state and ∂ is the spacing between the

discretized final states.

The Rabi frequency Ω'_{if} is proportional to the square root of FCF, which we calculate for the atomic ground motional states by exactly diagonalization of the atomic wavefunction. However, due to the high energy (> 10 GHz) of the final state, calculating FCF for the target state using this method requires an unrealiztic number of states to be included. Instead, we approximate it using the results for the atomic ground state by assuming the FCF to be proportional to the probability density of non-interacting atomic wavefunction at zero relative distance so that,

$$\Omega'_{if} = \Omega_0 \frac{\psi_f(r_{rel} = 0)}{\psi_0(r_{rel} = 0)}$$

where Ω_0 is the Rabi frequency between the excited state and the atomic motional ground state and ψ_f and ψ_0 are the wavefunctions of the final and ground motional atomic state without the molecular potential. This approximation is justifed because,

1. The molecular potential is short ranged and the excited molecular state is small.

2. Only the final atomic wavefunction within the molecular potential contributes to the FCF. For relatively low motional energy this wavefunction is proportional to the value of the wavefunction at the edge of the molecular potential which is well approximated by the atomic wavefunction without the molecular potential.

This approximation remains valid until the de Broglie wavelength for the atomic state is comparable to the size of the molecular potential which corresponds to a motional energy of ≈ 40 GHz and the result can still be used as order of magnitude estimation for higher motional energies.

For atomic motional ground state, we have,

$$\psi_0(r_{rel} = 0) = \prod_{i=1}^{3} \left(\frac{\mu\omega_i}{\pi}\right)^{1/4}$$

$$= \left(\frac{\mu^3 \omega_1 \omega_2 \omega_3}{\pi^3}\right)^{1/4}$$

where μ is the reduced mass $\mu \equiv m_{Na}m_{Cs}/(m_{Na} + m_{Cs})$, and ω_i's are the relative trapping frequencies along the three trap axis. We discretize the continuum state by adding an infinitely deep spherical potential well of radius R around the center. The radial wavefunctions of the eigenstates within the well with quantum number $n = 1, 2, \ldots$ is,

$$\psi_n = \frac{1}{\sqrt{4\pi}r_{rel}}\sqrt{\frac{2}{R}}\sin\left(\frac{\pi n r_{rel}}{R}\right)$$

and the corresponding energy,

$$E_n = \frac{\pi^2 n^2}{2\mu R^2}$$

The energy gap between neighboring states is

$$\delta_n \approx \frac{\pi^2 n}{\mu R^2}$$

and the wavefunction value at $r_{rel} = 0$ is,

$$\psi_n(r_{rel} = 0) = \sqrt{\frac{1}{2\pi R}} \frac{\mathrm{d}}{\mathrm{d}r_{rel}} \sin\left(\frac{\pi n r_{rel}}{R}\right)\Bigg|_{r_{rel}=0}$$

$$= \frac{\pi n}{\sqrt{2\pi R}R}$$

Substituting into Γ and taking the limit of $R \to \infty$ we have

$$\Gamma = 2\pi \frac{\Omega_0^2}{\delta} \frac{\psi_f^2(r_{rel} = 0)}{\psi_0^2(r_{rel} = 0)}$$

$$= 2\pi \Omega_0^2 \frac{\mu R^2}{\pi^2 n} \frac{\pi^2 n^2}{2\pi R^3} \sqrt{\frac{\pi^3}{\mu^3 \omega_1 \omega_2 \omega_3}}$$

$$= \Omega_0^2 \frac{n}{R} \sqrt{\frac{\pi^3}{\mu \omega_1 \omega_2 \omega_3}}$$

$$= \Omega_0^2 \sqrt{\frac{2\pi E}{\omega_1 \omega_2 \omega_3}}$$

For the condition in Fig. 5.6A we have $\Omega_0 = 2\pi \cdot ...$, $E = 2\pi \cdot ...$ and $\omega_{1,2,3} = 2\pi \cdot ...$ which predicts a broadened linewidth of $\Gamma = 2\pi \cdot ....$ This prediction is only an estimate due to the breakdown of the approximation we used and is in fact broader than the observed value. Nevertheless, it confirms that this broadening mechanism can explain the observed linewidth.

5.3.3.2   Eliminating the Broadening with Blue Detuned Tweezer

Another prediction from the theory is that if the tweezer light is blue detuned from the PA line, the two-photon process will not couple to the motional continuum anymore and there should be no
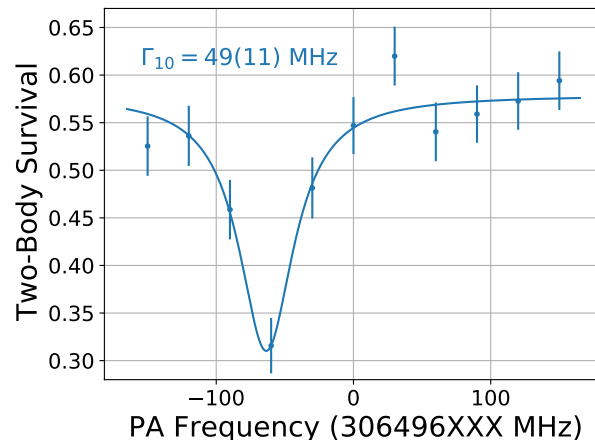
Figure 5.8: Fitting of PA linewidth for 10 mW tweezer power at 306612 GHz. The linewidth is significantly narrower than the value measured when the tweezer is red detuned from the PA resonance (Fig. 5.6).

broadening of the line [*]. We can confirm this by measuring the linewidth of the same PA line with the tweezer frequency set to 306612 GHz. The result shown in Fig. 5.8 confirms that the linewidth is indeed narrower for this tweezer frequency.

5.3.3.3   Implication on Two-Photon Transition to Ground Molecular States

Since the broadening is caused by two-photon coupling to high energy atomic motional states, the observed linewidth in a PA measurement cannot be directly translated to the scattering rate during a two-photon transition that uses different set of laser frequencies.

In fact, with a single ground atomic spin state, the scattering rate for the final molecular state during a two-photon transition is not affected by this effect. As shown in Fig. 5.9B-E, the molecular state cannot reach the atomic motional continuum via a two-photon transition. The atomic state,

---

[*]Note that the tweezer is still red detuned from the atomic state which provides most of the trapping potential

102
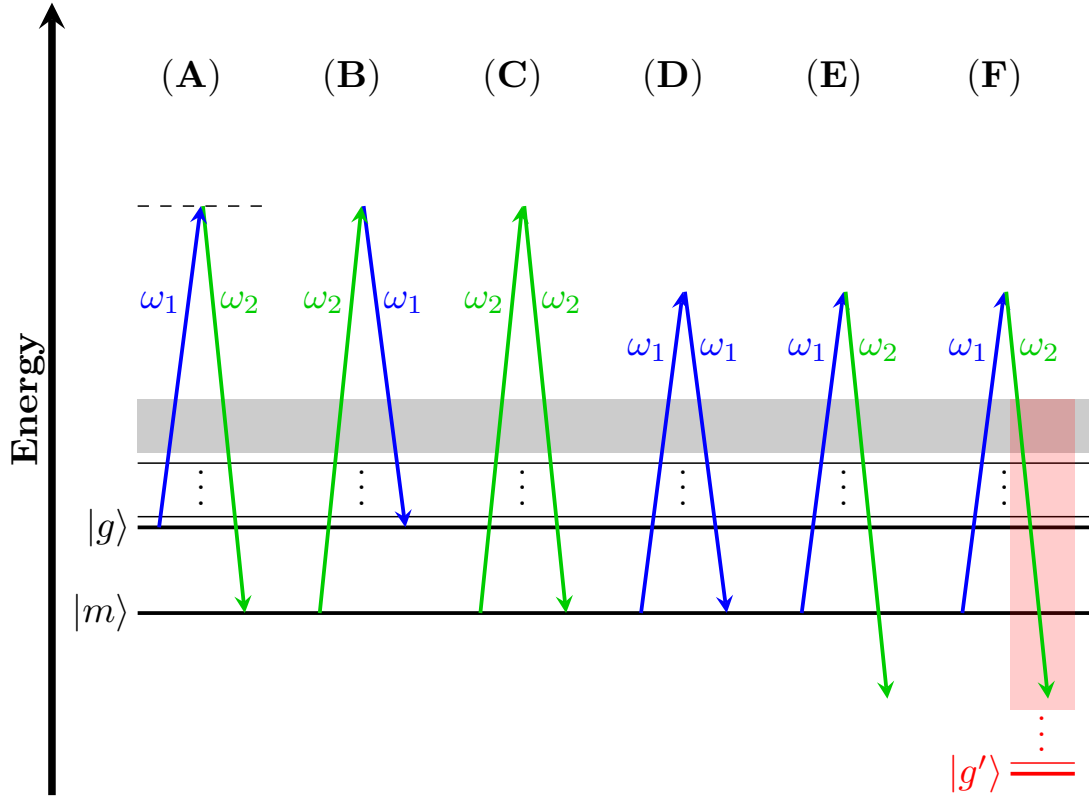
Figure 5.9: Effect of two-photon coupling to atomic contimuum on molecular state. (A) Raman transition from the atomic ground state $|g\rangle$ to the molecular bound state $|m\rangle$ using two Raman beams with frequencies ω_1 and ω_2. (B-E) Two photon transitions starting from the molecular state $|m\rangle$ with different frequency combinations without additional atomic spin states. (B) This is the reverse Raman transition and reaches the initial atomic state. (C,D) The frequency pairs couples back to $|m\rangle$. (E) This couples to an energy below $|m\rangle$. Note that none of the two-photon transitions from $|m\rangle$ in (B-E) ends up in the atomic motional continuum and therefore unaffected by the broadening mechanism discussed in this section. (F) The present of another atomic spin state $|g'\rangle$ with lower energy allows the two-photon transition from $|m\rangle$ to be coupled to the motional continuum corresponding to the new spin state. Note that only the frequency combination similar to (E) is shown for simplicity, other cases may also couple to the same continuum.

on the other hand, can reach the continuum though the loss rate is in general much lower than the molecular state and is usually not the limiting factor for the transfer efficiency.

The molecular state can also couple to a different motional continuum if there are other atomic spin state with lower energy (Fig. 5.9F). Since stable atomic state has the lowest energy amount all the ones with the same total m_F, such state must have a different total m_F than the initial state. Therefore, such coupling is forbidden if the two Raman beams both has π polarization, as is the case for the Raman transition in chapter 6 and 7, and will not cause any loss due to this mechanism. Polarization impurity, however, can allow such coupling and enable this loss process.

5.4   Summary and Outlook

We continued our study of the interaction between two atoms in the optical tweezer. We characterized the excited molecular potential by measuring the energy of bound states using photoassociation spectroscopy and identified the states based on their rotational structure. On the other hand, the high intensity of the optical tweezer also creates unique challenges that can lead to dissociation or loss of the atoms or molecules. We studied one of the effect and confirmed our model for the loss process with additional measurements and discussed its implication for future experiment. The identification of the excited molecular state opens up the pathway to formation of ground state single molecule via two-photon process and will be focus of later chapters.

6

Two-photon Spectroscopy of NaCs

Ground State

6.1 Introduction

The excited molecular states measured and characterized in chapter 5 provide us a pathway to couple to the ground electronic molecular states using two-photon transitions. While it is in principle

possible to drive from the atomic state to any desired molecular ground state for various applications, doing so directly has many technical challenges. We will cover these challenges as well as the considerations in selecting the molecule formation pathway in chapter 7, however, the difficulty, and the main difference from a pure atomic Raman transition, lies in the wavefunction size mismatch. As we have seen already in section 5.3.1, the size mismatch between the excited molecular states and the ground atomic state causes a very small FCF and requires a high PA intensity to improve the signal strength. This small FCF also reduces the Rabi frequency for the two-photon transition to the ground state. As a result, driving a two-photon transition to an arbitrary molecular ground state may require maintaining coherence between two different lasers over a relatively long time (milliseconds) which is very difficult to achieve.

Our solution to this challenge is to do the transfer via a two step process.

1. We drive a two-photon transition from the atomic state to a weakly bound ground state. The reduced energy difference allows the laser coherence to be maintained over a longer time easily. In the case of NaCs molecule, this also increases the FCF between the ground and excited molecular states which allows shorter pulse time and further reduces the coherence requirement.

2. The transfer to arbitrary molecular ground state will be done from the weakly bound state created in the first step. The strength of this transition can be much higher and only requires a relatively shorter laser coherence time. This step has already been demonstrated in other experiments [1] so in this thesis we will focus only on the first step transfer.

In this chapter, we will discuss the use of Raman spectroscopy to measure the properties of the weakly bound molecular ground states. In section 6.2 we will describe the states involved and the setup for the Raman spectroscopy as well as the measured binding energy for the $N = 0$ states. In

106

section 6.3 we study the coupling between angular momentums for near threshold molecular states by characterizing the $N = 2$ states.

6.2   Weakly Bound NaCs Ground States

As mentioned in section 5.2.1.2, the angular momentum coupling for weakly bound molecular state is similar to that of the atoms. Therefore, instead of using the term symbol for the *Hund's case (a)* to identify the molecular potential and bound states, we use the hyperfine state (F_{Na}, F_{Cs}) for the atoms instead. Similarly, since the vibrational states of the molecule does not always corresponds to a particular short range potential, we also label the vibrational states from the the atomic state threshold. Under this system, the atomic motional ground state is $v'' = 0$ and the first (lowest binding energy) molecular bound state is $v'' = -1$.

In order to measure the binding energy of a molecular state, we first prepare the atom in the corresponding hyperfine state and drive a Raman transition to the molecular state. We use a Raman transition that is detuned from the $c^3\Sigma(v' = 0)$ state measured in section 5.3 (Fig. 6.1). When the Na and Cs are in the same tweezer, they can undergo fast spin-exchange collision that changes the hyperfine state of the atom. This process can cause the hyperfine energy (> 1 GHz) of the atoms to be transferred to the motional energy and eject the atoms from the tweezer (< 100 MHz deep). As a result, the measurement can only be done when the spin-exchange collision is suppressed, which includes the following spin combinations,

1. $F_{Na} = 1$ and $F_{Cs} = 3$
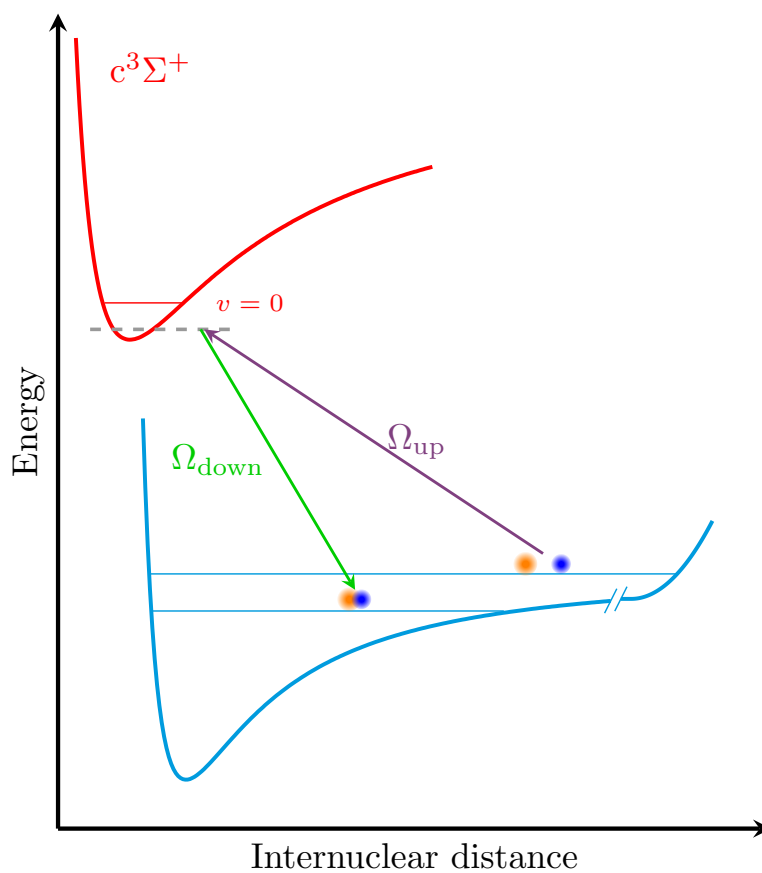   This is the spin state with the lowest energy and therefore the spin-exchange interaction is

Figure 6.1: States and beams in the Raman transition. From the initial atomic motional ground state, we drive a Raman transition to a weakly bound molecular ground state by detuning from the $c^3\Sigma(v' = 0)$ state.

energetically forbidden. In the experiment, we use the state $|\mathrm{Na}(1,1),\mathrm{Cs}(3,3)\rangle$ which can be prepared from the $|\mathrm{Na}(2,2),\mathrm{Cs}(4,4)\rangle$ state from OP easily by driving a Raman transition for both Na and Cs atoms. This state also remains the lowest energy atomic state in the present of a weak magnetic field.

2. $|\mathrm{Na}(2,2),\mathrm{Cs}(4,4)\rangle$ and $|\mathrm{Na}(2,2),\mathrm{Cs}(3,3)\rangle$ *

   These spin states are stable because the spin-exchange collision conserves total m_F of the two atoms and the two states are the lowest energy states that has the same total m_F. Inelastic collision that changes the total m_F can also happen but has a lower collision rate since it requires transferring angular momentum between the spin and motion of the atom.

6.2.1   Driving Raman Transition using the Optical Tweezer

In order to increase the intensity of the Raman beams to overcome the small FCF, we use the tweezer beam to drive the Raman transition (Fig. 6.2A). Not only does this maximizes the intensity due to the small focal size of the tweezer, since the atoms are trapped at the maximum of the tweezer beam, this also ensures that the Raman beam is aligned automatically to the atoms and suppresses sensitivity to mechanical fluctuation that is usually caused by a small beam size. Moreover, this also minimizes the number of beams the atoms experience during the Raman transition which, in turns, minimizes the scattering. As a result, the coherence of the transition is also improved which is important for achieving coherent creation of molecule (chapter 7).

The beampath to generate the required frequencies in the tweezer is shown in Fig. 6.3. The additional single pass AOM in the beampath avoids interference with AOM leak light causing power

---

*States with opposite m_F, i.e. $|\mathrm{Na}(2,-2),\mathrm{Cs}(4,-4)\rangle$ and $|\mathrm{Na}(2,-2),\mathrm{Cs}(3,-3)\rangle$ are also stable but are omitted here since these cannot be easily prepared in our experiment.
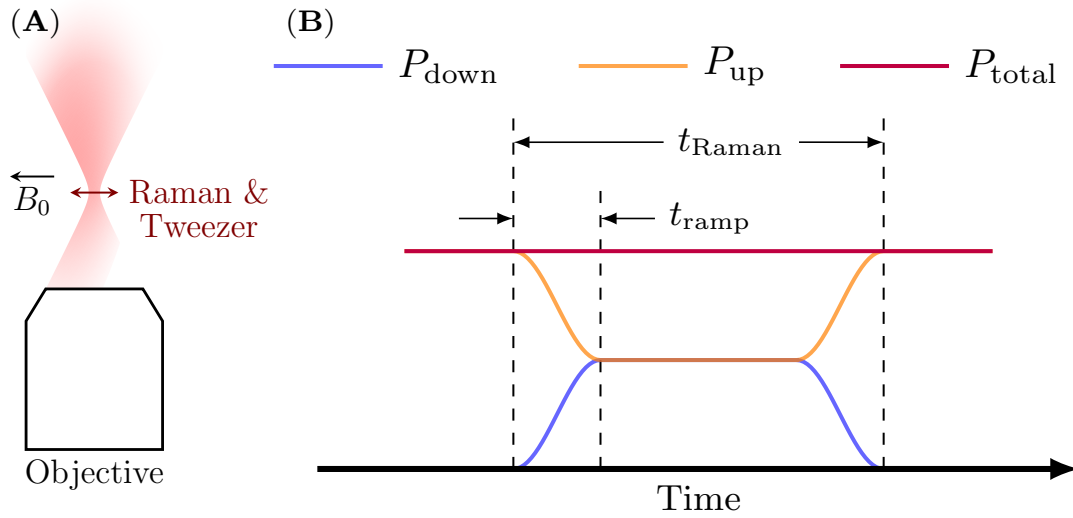
Figure 6.2: (A) Geometry and polarization of trap and Raman beam relative to the bias magnetic field. We use a bias B field of $B_0 = 8.8\,\mathrm{G}$ alone the tweezer polarization to define the quantization axis which is the same as the one used for Raman sideband cooling in Fig. 3.2. As a result, the atoms experiences predominately π polarization from the tweezer. (B) Raman transition pulse sequence. The tweezer initially consists of only up leg power. When driving the Raman transition, the up leg power is smoothly ramped down and the down leg power ramped up over $t_{\mathrm{ramp}} = 10\,\mu s$ while maintaining the total power of the tweezer. This minimizes the heating on the atoms due to power fluctuation while maximizes the time with maximum Raman Rabi frequency when the up and down leg powers are equal.
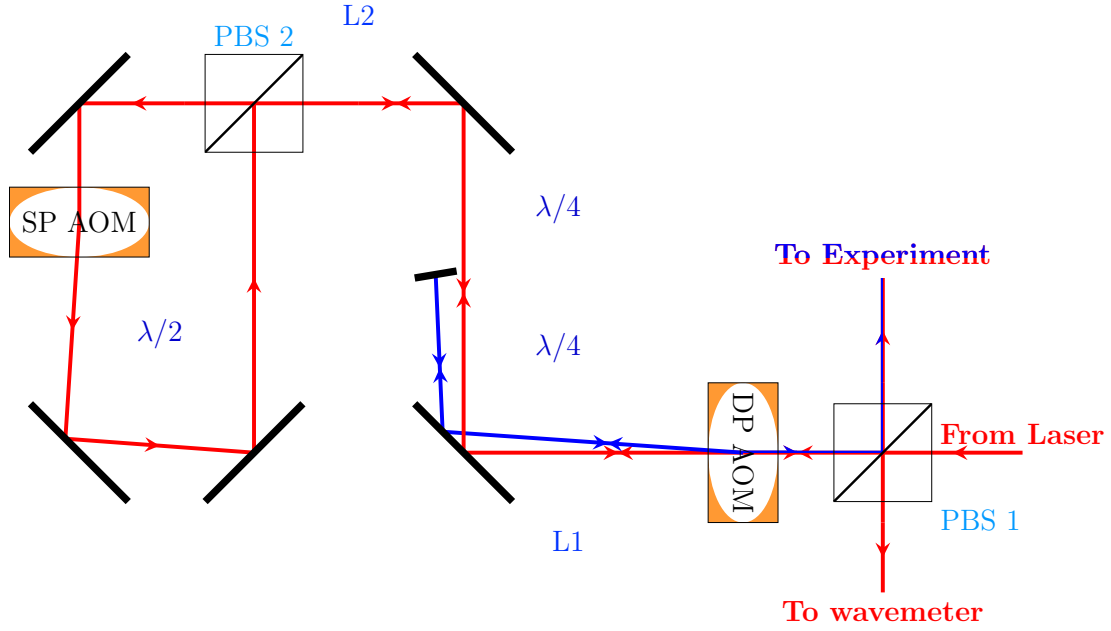
Figure 6.3: Beampath for generating the frequency for Raman transition in the tweezer. (Beampath for fiber coupling and overall power control is not shown.) The red beam path is the 0-th order of the double pass (DP) AOM which is used for the tweezer. When the DP AOM is turned on, some power is redirected to the first order (blue beam path) which generates the required frequency different to drive the Raman transition. The two frequencies are recombined on the DP AOM. The 0-th order light is shifted by another single pass (SP) AOM running on a different frequency before recombining. Without this AOM, the leak light from the DP AOM will be at the same frequency as the 0-th order light which can cause a significant power fluctuation due to interference. The SP AOM ensures that none of the leaking light frequency coincide with either intended frequencies therefore avoiding this issue. Different selection of the SP and DP AOM as well as their orders can be used to cover a wide range of two photon detuning for Raman transition. The experiment typically start with the SP AOM on and the DP AOM off. When driving the Raman transition, the powers on both AOMs are ramped simultaneously to achieve the desired power at both frequencies.
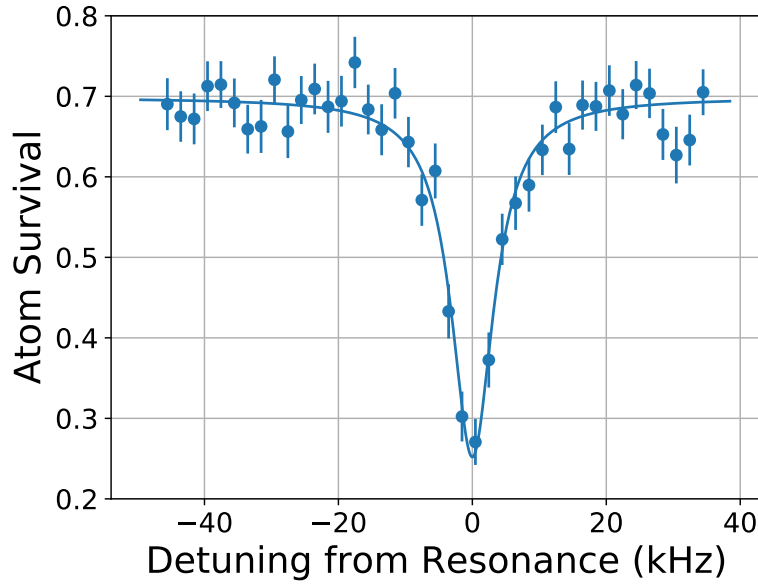
Figure 6.4: Raman resonance for $v'' = -1$, $N = 0$ state from $|Na(2,2), Cs(4,4)\rangle$.

fluctuation and also increases the frequency tuning range compared to using only one double pass

AOM. The powers at each frequencies are calibrated as a function of AOM powers so that we can

select the desired power ratio during the experiment. When driving the Raman transition, instead

of turning on separate beam, we ramp down the power at the original tweezer and ramping up

the power in the second frequency while maintaining the total power to minimize heating of the

atoms (Fig. 6.2B).

6.2.2 Raman Resonance on $N = 0$ Ground State

We first measure the binding energy for the $v = '' -1$, $N = 0$ state from the atomic states $|Na(2,2), Cs(4,4)\rangle$,

$|Na(1,1), Cs(3,3)\rangle$, and $|Na(2,2), Cs(3,3)\rangle$. Fig. 6.4 shows the measured Raman resonance from

$|Na(2,2), Cs(4,4)\rangle$ using 10 mW of tweezer power at a detuning of -100 GHz from the $v' = 0$

Table 6.1: Binding energies and Zeeman shift for $v'' = -1$, $N = 0$ states.

Spin state	Resonance (MHz)		Zeeman shift (kHz/G)
	8.8 G	0 G	
$|Na(2,2), Cs(4,4)\rangle$	297.8472(28)	297.8510(28)	$-0.43(10)$
$|Na(1,1), Cs(3,3)\rangle$	367.7892(25)	369.63(29)	$-209(33)$
$|Na(2,2), Cs(3,3)\rangle$	770.200516(24)	769.8294(22)	42.17(24)
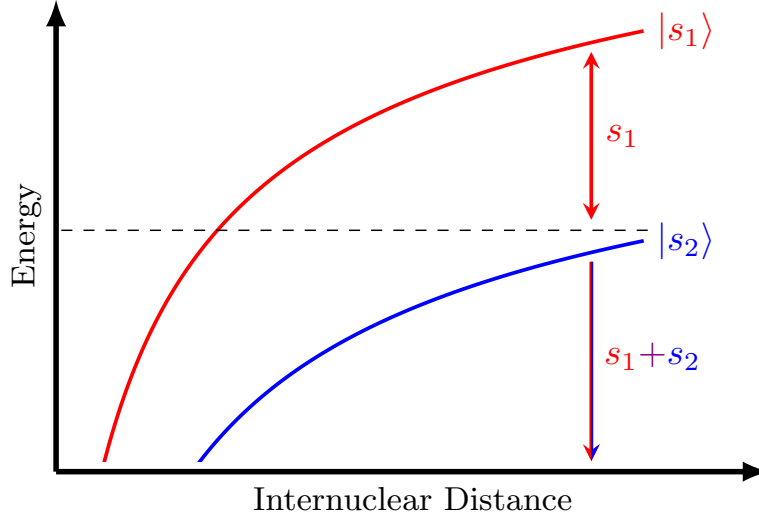
Figure 6.5: Spin state mixing near the atomic threshold. Energy above the s_2 threshold only supports one molecular spin state so the bound state within the s_1 potential in this region is almost purely s_1. Energy below the s_2 threshold supports both s_1 and s_2 molecular states so bound states in this region may have a mixture of s_1 and s_2 if the two spin states are coupled. This includes all the s_2 bound states and some of the s_1 bound states.

excited state and a 2 ms pulse time.

The tweezer also shifts the resonance frequency. We remove this effect by measuring the resonance at different tweezer power and extrapolate to zero trap powers. Similarly, we measure the Zeeman shift and the resonance frequency at zero magnetic field. The summary of the results are shown in table 6.1.

Note that the Zeeman shift for the $|Na(2,2), Cs(4,4)\rangle$ state is signicantly smaller than that

for other spin states. The reason for this is spin mixing due to magnetic coupling between states with the same total m_F[*]. The $|Na(2,2), Cs(3,3)\rangle$ spin state is coupled to the $|Na(2,2), Cs(4,3)\rangle$, $|Na(1,1), Cs(4,4)\rangle$ and $|Na(2,1), Cs(4,4)\rangle$ states whereas $|Na(1,1), Cs(3,3)\rangle$ is coupled to the $|Na(2,1), Cs(3,3)\rangle$, $|Na(1,1), Cs(4,3)\rangle$, $|Na(2,1), Cs(4,3)\rangle$, $|Na(2,2), Cs(3,2)\rangle$ and $|Na(2,2), Cs(4,2)\rangle$ states. All of these states listed above has higher energy so their bound states may cause spin mixing with the $|Na(2,2), Cs(3,3)\rangle$ and $|Na(1,1), Cs(3,3)\rangle$ bound states (Fig. 6.5) causing them to have a different magnetic field dependency from the corresponding atomic state resulting in a non-zero differential Zeeman shift. On the other hand, the $|Na(2,2), Cs(4,4)\rangle$ bound state is above all the other spin states and therefore has a mostly pure spin state and the transition has little Zeeman shift.

6.3   Rotational Excited NaCs Ground State

In additional to the $N = 0$ state, we also measure the energies of rotational excited states. Not only do these measurements allow us to verify the rotational state for our previous results, we can also take advantage of the precision of the Raman spectroscopy to study the rich interaction between the nuclear rotation and atomic spin.

Due to parity conservation in the Raman transition, the final molecular state must have an even N so the lowest rotational excited state we can address is $N = 2$. We use $|Na(2,2), Cs(4,4)\rangle$ as the initial state since, as we saw in the previous section, the corresponding molecular bound state has the least mixing other molecular potentials. Similarly, we select $F_{\text{atom}} = 6$ as the final total atomic spin state since this is the state we address in the corresponding $N = 0$ spectroscopy and it includes the

---

[*]The same coupling that leads to spin exchange collision.

$m_{F_{\text{atom}}} = 6$ state which has minimum Zeeman shift as discussed in the previous section.

6.3.1 Angular Momentum Coupling in $N = 2$ Ground State

Since the full Hamiltonian is rotaionally symmetric for rotation around the field direction, $m_F \equiv m_{F_{\text{atom}}} + m_N = 6$ is conserved in the Raman transition, which includes a total of three states. However, the exact states we are coupling to and the good quantum numbers depends on the strength of the external field.

At zero or very low external field, the good quantum numbers are F and m_F due to coupling between $\mathbf{F}_{\text{atom}}$ and $\mathbf{N}$. as discussed in section 5.2.1.2. In this basis, the three energy eigenstates are $|F = 6, m_F = 6\rangle$, $|F = 7, m_F = 6\rangle$ and $|F = 8, m_F = 6\rangle$.

External field, both magnetic and electric[*], couples mostly to the atomic spin $\mathbf{F}_{\text{atom}}$ [†] rather than the nuclear rotation $\mathbf{N}$. Therefore, at high field $\mathbf{F}_{\text{atom}}$ and $\mathbf{N}$ decouples and their projections become good quantum numbers individually. In this case, the three energy eigenstates are $|m_{F_{\text{atom}}} = 6, m_N = 0\rangle$, $|m_{F_{\text{atom}}} = 5, m_N = 1\rangle$ and $|m_{F_{\text{atom}}} = 4, m_N = 2\rangle$.

6.3.2 $N = 2$ Raman Resonances

Fig. 6.6 shows the Raman spectrum taken at 8.8 G of magnetic field and 10 mW of tweezer power where three resonances can be clearly seen as expected. This single measurement, however, does not allow us to directly identify the states that correspond to each of the resonances. Because of this, we

---

[*]Light field from the tweezer.
[†]More precisely the electron spin within $\mathbf{F}_{\text{atom}}$.

Figure 6.6: $N = 2$ Raman spectrum with $8.8\,\mathrm{G}$ of magnetic field and $10\,\mathrm{mW}$ of tweezer power. The three resonances corresponds to three $m_F = 6$ states.

measured the resonance at various tweezer powers and magnetic field as shown in Fig. 6.7. Each dot in the plot corresponds to an observed resonance frequency.

In order to understand the dependency of the resonances on the external fields we use the following phenomenological model. The Hamiltonian in the $m_F = 6$ subspace we coupled to can be expressed as,

$$H = H_0 + H_1$$

where H_0 is the zero field term due to the coupling between $\mathbf{F}_{\mathrm{atom}}$ and $\mathbf{N}$, and the H_1 term is due to the coupling to external fields. At zero external field, the eigenstates are the F and m_F basis and the

Figure 6.7: Dependency of $N = 2$ Raman resonances on the tweezer power at (A) $8.8\,\mathrm{G}$ and (B) $5.28\,\mathrm{G}$ magnetic field. The different colors shows the resonance frequency for the states with the lowest (blue), second lowest (orange) and highest (green) binding energies. All of the data are taken in the intermediate field regime and therefore in a mixture of different spin states. The lines are fits to the resonance frequencies using a field dependent Hamiltonian.

Table 6.2: Fitted parameters for the $N = 2$ Hamiltonian. Since the ΔE_Fs are not independent ΔE_8 is not a free parameter and is rather $-\Delta E_6 - \Delta E_7$. Also note that the fit is directly from the binding energy measured in Fig. 6.7 so the zero energy of the Hamiltonian is the atomic $\left|\mathrm{Na}(2,2),\mathrm{Cs}(4,4)\right\rangle$ state which also has non-zero Zeeman an AC Stark shifts.

H_0 parameters			
E_0 (MHz)	ΔE_6 (MHz)	ΔE_7 (MHz)	ΔE_8 (MHz)
$-99.196(89)$	$-0.146(87)$	$-0.652(78)$	$0.80(11)$
AC Stark shift parameters			
a_0 (MHz/mW)		a_1 (MHz/mW)	a_2 (MHz/mW)
$1.015(18)$		$0.721(21)$	$6.4(22) \times 10^{-2}$
Zeeman shift parameters			
b_0 (MHz/G)		b_1 (MHz/G)	b_2 (MHz/G)
$-0.237(22)$		$-0.222(22)$	$-0.947(23)$

most generic term is,

$$H_0 = E_0 + \sum_{F=6,7,8} \Delta E_F |F, m_F = 6\rangle\langle F, m_F = 6|$$

where E_0 is the "average" energy and ΔE_F are the shift for each F states with $\sum_{F=6,7,8} \Delta E_F = 0$. The term for coupling to the external fields couples to the $m_{F_{\text{atom}}}, m_N$ basis and the generic expression for such a term is,

$$H_1 = \sum_{i=0,1,2} (P_{\text{tweezer}} \cdot a_i + B \cdot b_i) |m_{F_{\text{atom}}} = 6 - i, m_N = i\rangle\langle m_{F_{\text{atom}}} = 6 - i, m_N = i|$$

where P_{tweezer} is the tweezer power, B is the magnetic field, and a_i and b_i are the state dependent AC Stark shift and Zeeman shift of the binding energies. We numerically diagnolize this Hamiltonian and fit to the experimental data as shown in the lines in Fig. 6.7. The free parameters of the Hamiltonian we obtained are shown in table 6.2.

6.4 Summary and Outlook

Based on the study of excited molecular states using photoassociation spectroscopy, we study the structure of the ground molecular state using Raman transitions. Compared to the excited states, the stability of the ground state molecules allows us to resolve single quantum states and control all degrees of freedoms within the molecule. The path to coherent optical formation of ground state molecule is now fully cleared and this will be the focus of chapter 7.

7

Coherent Optical Creation of NaCs

Molecule

7.1 Introduction

7.2 Raman Transition Beyond Three-Level Model

For a Raman transition with Raman Rabi frequency Ω_R and total scattering rate Γ, defined as the sum of the scattering rate for the initial and final states, the probability of scattering during a π pulse is,

$$
\begin{aligned}
p_s &= \frac{\Gamma t_\pi}{2} \\
&= \frac{\pi \Gamma}{2\Omega_R}
\end{aligned}
$$

which is proportional to the ratio Γ/Ω_R. In an ideal three-level system, this is the only source of decoherence which can be made arbitrarily small by using a large single photon detuning (section 3.2.1.1). However, in a real system, there are often other effects that increases the scattering and may also put a lower limit on the scattering probability during the transfer. Fig. 7.1 shows a generic model for a real Raman transition demostrating some of these effects. Additionally, other practical

Figure 7.1: Generic model for a real Raman transition. The initial state $|i\rangle$ and the final state $|f\rangle$ has a energy difference δ and are coupled by two Raman beams with frequencies and single photon Rabi frequencies of ν_1, Ω_1 and ν_2, Ω_2 respectively. The corresponding matrix elements (arbitrary unit) are M_1 and M_2. The Raman beams are detuned by Δ from the primary excited state $|e\rangle$, which has a decay rate of Γ_e. We also consider additional states near the initial ($|i'\rangle$), final ($|f'\rangle$) and intermediate excited $|e'\rangle$ states which are separated from the corresponding Raman transition states by ω_i', ω_f' and ω_e' respectively. Only one additional state of each kinds are included to simplify the discussion without loss of generality.

limitation in the system like stability of the laser power and frequency also needs to be taken into account.

In the experiment, we find the parameter range that gives the best transfer efficiency using numerical simulation (section 7.4). Nevertheless, in order to develop a general approach that can be applied to other systems, it is also important to understand the various physical mechanism that leads to the optimal parameters. Therefore, in this section, we will discuss some of the most impor-

tant effects on the transfer efficiency at qualitative and semiquantitative level. Due to experimental constraint, we will assume that the single photon detuning is much smaller than the frequency of each individual beams, i.e. $\Delta \ll \nu_1, \nu_2$.

7.2.1 Additional Initial and Final States

First, we will discuss the effect of $|i'\rangle$ and $|f'\rangle$ states near the initial and final states. These states can be coupled to the excited state $|e\rangle$ by the Raman beams, which can in tern be coupled to the initial and final states by an off-resonance Raman transition. The leakage is suppressed by the detuning from the Raman resonance, i.e. ω_i' and ω_f'. This puts a limit on the Raman Rabi frequency Ω_R to be smaller than the smallest energy gap, which in turns puts a limit on the minimum Raman transfer time. In our experiment, the minimum energy gap comes from axial motional excitation of the atomic initial states which is between $2\pi \times 10 - 30$ kHz depending on the trap depth used. The typical Raman π time we can realize is $0.5 - 5$ ms so this effect is not a major limiting factor for our transfer efficiency.

7.2.2 Additional Excited States

Next, we will consider the effect of the $|e'\rangle$ state near the excited intermediate state. These states can be coupled to the ground states, both $|i\rangle$ and $|f\rangle$, by the Raman beams and can cause a change in both the Raman Rabi frequency and the scattering rate. There are two relevant limiting cases that needs to be discussed separately.

Figure 7.2: Effect of additional excited states $\left|e'\right\rangle$ on the Raman transition efficiency. (A) Depending on the sign of the coupling, there could be constructive (blue) or destructive (orange) interference on the Raman Rabi frequency Ω_R. (B) Increased scattering rate Γ_s caused by $\left|e'\right\rangle$ with a minimal between the two states. (C) Optimal detunine exists between the two states with maximum transfer efficiency corresponds to a fraction of the state spacing.

7.2.2.1 EXCITED STATE SPACING LARGER THAN SINGLE-PHOTON DETUNING

In this case, the single photon frequency falls in between the two excited states $|e\rangle$ and $|e'\rangle$, which happens when $|e'\rangle$ is a different vibrational or electronic state. The total Raman Rabi frequency (Fig. 7.2A) is,

$$\Omega_R = \frac{\Omega_1\Omega_2}{2\Delta} + \frac{\Omega_1'\Omega_2'}{2(\Delta - \omega_e')}$$

where Ω_1' and Ω_2' are the single photon Rabi frequencies coupling $|e'\rangle$ to $|i\rangle$ and $|f\rangle$ respectively. Depending on whether $\Omega_1'\Omega_2'$ has the same (orange line) or different (blue line) sign as $\Omega_1\Omega_2$, the total Raman Rabi frequency may be cancelled or enhanced between the two excited states. On the other hand, the total scattering rate (Fig. 7.2B) is almost always increased due to the additional state, creating a local minimum between the excited states. Combining the two effects, the ratio between the Raman Rabi frequency and the scattering rate, which determines the transfer efficiency, always have local maximum between the excited states (Fig. 7.2C).

Despite the difference in the position and value of the maximum for different $|e'\rangle$ parameters, we can summarize the effect on the transfer efficiency as a limit on the maximum detuning Δ_{max} to a fraction of the spacing between the excited states (ω_e'). As an example, the blue and orange maxima in Fig. 7.2C corresponds to a limit on single photon detuning of $0.5\omega_e'$ and $0.15\omega_e'$. As one would expected, a larger excited state spacing usually result in a larger detuning limit and a better transfer efficiency.

Summarizing the effect of additional excited state as a single number Δ_{max} allows us to keep using

the equation for Raman transition with minor corrections and makes it easier to compare different

state selection and transition schemes. It is also worth noting that although only one additional

excited state $|e'\rangle$ is considered here, this result can be generalized when more excited states are taken

into account as well. These states introduces additional smooth variation in both the Raman Rabi

frequency and scattering rate and the effects on the final transition efficiency can be similarly treated

as a change in the maximum detuning.

7.2.2.2 Excited State Spacing Much Smaller than Single-Photon Detuning

This is typically the case when $|e'\rangle$ is a different rotational or hyperfine state. In this case, the Ra-

man transition is detuned from both $|e\rangle$ and $|e'\rangle$ at the same time and the two excited states behaves

similar to an effective state $|e''\rangle$ with modified coupling strengths and decay rate.

When the initial and final ground states have (nearly) identical spin and rotational state, which is

the case for the our transition to $N = 0$ states discussed in section 6.2.2, the new effective state will

behave very similar to the original ones. This is because the coupling between the ground states and

excited states is determined by,

$$\Omega_{1,2}^{i} = \Omega_{1,2}^{0} \langle \mathrm{F}_e^i | \mathrm{F}_g \rangle$$

where the superscript i represents different excited states, the subscript 1, 2 represents the initial (1)

and final (2) ground state, $\Omega_{1,2}^0$ is the reduced Rabi frequency without the angular momentum

projection, and F_e^i and F_g are the rotation and spin state for the excited and ground state respectively.

Note that the ground states $|i\rangle$ and $|f\rangle$ both have the same F_g. This means

$$\frac{\Omega_1^i}{\Omega_2^i} = \frac{\Omega_1^0}{\Omega_2^0}$$

which is a constant. Given that the excited state linewidth for different rotation and hyperfine states are very similar, we have the Rabi frequency to scattering rate ratio.

$$\frac{\Omega_R}{\Gamma_s} \approx \left(\sum_i \frac{\Omega_1^i \Omega_2^i}{2\Delta} \right) \Big/ \left(\sum_i \frac{\Omega_1^{i\,2} + \Omega_2^{i\,2}}{4\Delta^2} \right)$$
$$= \frac{\Omega_1 \Omega_2}{2\Delta} \Big/ \frac{\Omega_1^2 + \Omega_2^2}{4\Delta^2}$$

which is the same as the expression for a single excited state.

The properties of the effective state can be very different, however, when the initial and final spin and rotational states are different. Nevertheless, other than the special case of complete destructive interference on the Raman Rabi frequency, the new excited state will generally have a worse ratio Ω_R/Γ_s by a constant factor. The dependency of the ratio on the detuning is not changed significantly for large detuning.

7.2.3 Cross Coupling Between Light Addressing Initial and Final States

Due to the small energy separation between the initial and final state δ, the cross coupling of the laser addressing the initial/final state on the final/initial state is another important effect in our experiment. Without the cross coupling, the total off resonance scattering rate for the initial and the

final states is

$$\Gamma_{s0} = \frac{\Gamma_e \left(\Omega_1^2 + \Omega_2^2 \right)}{4\Delta^2}$$

For a given Raman Rabi frequency $\Omega_R \propto \Omega_1 \Omega_2$, this is minimized when $\Omega_1 = \Omega_2$.

When cross coupling is taken into account, however, the total scattering rate becomes, [*]

$$\Gamma_s = \frac{\Gamma_e \Omega_1^2}{4M_1^2} \left(\frac{M_1^2}{\Delta^2} + \frac{M_2^2}{(\Delta + \delta)^2} \right) + \frac{\Gamma_e \Omega_2^2}{4M_2^2} \left(\frac{M_2^2}{\Delta^2} + \frac{M_1^2}{(\Delta - \delta)^2} \right) \tag{7.1}$$

$$\propto \frac{\Gamma_e P_1}{4} \left(\frac{M_1^2}{\Delta^2} + \frac{M_2^2}{(\Delta + \delta)^2} \right) + \frac{\Gamma_e P_2}{4} \left(\frac{M_2^2}{\Delta^2} + \frac{M_1^2}{(\Delta - \delta)^2} \right) \tag{7.2}$$

where $P_{1,2} \propto \Omega_{1,2}^2/M_{1,2}^2$ are the powers of the laser beams 1 and 2. When $\delta \ll \Delta$ such as our experiment,

$$\Gamma_s \approx \frac{\Gamma_e \left(M_1^2 + M_2^2 \right)}{4\Delta^2} \left(\frac{\Omega_1^2}{M_1^2} + \frac{\Omega_2^2}{M_2^2} \right)$$

$$\propto \frac{\Gamma_e \left(M_1^2 + M_2^2 \right)}{4\Delta^2} \left(P_1 + P_2 \right)$$

For a given Raman Rabi frequency $\Omega_R \propto \Omega_1 \Omega_2 \propto \sqrt{P_1 P_2}$, this is minimized when $P_1 = P_2$.

Hence, due to the strong cross coupling, we need to use the same power in both Raman beams rather than adjusting the powers to match their single photon Rabi frequencies.

Moreover, at the minimum scattering rate, we have $\Omega_2 = \Omega_1 M_2/M_1$ and the ratio between

---

[*]Here we assume that the matrix elements are the same for the two beams. This is the case when the two beams have the same polarization as in our experiment. This effect can be minimized or eliminated by selecting different polarizations for the two laser frequencies that does not couple to the other initial/final state. This would also require choosing an excited state with the same or lower angular momentum as the ground states in order to avoid cross coupling to different excited states.

Raman Rabi frequency and scattering rate is,

$$
\begin{aligned}
\frac{\Omega_R}{\Gamma_s} &= \frac{\Omega_1 \Omega_2}{2\Delta} \frac{4\Delta^2}{\Gamma_e \left(M_1^2 + M_2^2\right)} \Big/ \left(\frac{\Omega_1^2}{M_1^2} + \frac{\Omega_2^2}{M_2^2}\right) \\
&= \frac{2\Delta\Omega_1\Omega_2}{\Gamma_e \left(M_1^2 + M_2^2\right)} \Big/ \left(\frac{\Omega_1^2}{M_1^2} + \frac{\Omega_2^2}{M_2^2}\right) \\
&= \frac{\Delta\Omega_1^2 M_2}{\Gamma_e M_1 \left(M_1^2 + M_2^2\right)} \frac{M_1^2}{\Omega_1^2} \\
&= \frac{\Delta}{\Gamma_e} \frac{M_1 M_2}{M_1^2 + M_2^2}
\end{aligned}
$$

Therefore, for a given excited state linewidth Γ_e and maximum detuning (section 7.2.2) the transfer efficiency maximizes for the smallest $M_1 M_2 / (M_1^2 + M_2^2)$ which happens when the ratio M_1/M_2 is the closest to 1.

The light shift of the Raman resonance is similarly affected by the cross coupling. The differential light shift between the initial and the final state determines the resonance fluctuation as a function of light intensity fluctuation. The ration between the light shift and the Raman Rabi frequency, i.e. line width, determines the stability requirement of our laser indensity. With cross coupling, the differential shift is (assuming $\delta \ll \Delta$),

$$
\begin{aligned}
\Delta\delta &\approx \frac{\Omega_1^2}{4\Delta} - \frac{\Omega_1^2 M_2^2}{4\Delta M_1^2} - \frac{\Omega_2^2}{4\Delta} + \frac{\Omega_2^2 M_1^2}{4\Delta M_2^2} \\
&= \frac{M_1^2 - M_2^2}{4\Delta} \left(\frac{\Omega_1^2}{M_1^2} + \frac{\Omega_2^2}{M_2^2}\right) \\
&\propto \frac{M_1^2 - M_2^2}{4\Delta} (P_1 + P_2)
\end{aligned}
$$

which is also minimized when $P_1 = P_2$ at a given Raman Rabi frequency.

The ratio with the Raman Rabi frequency is,

$$
\begin{aligned}
\frac{\Delta\delta}{\Omega_R} &\approx \frac{M_1^2 - M_2^2}{4\Delta}\left(\frac{\Omega_1^2}{M_1^2} + \frac{\Omega_2^2}{M_2^2}\right)\frac{2\Delta}{\Omega_1\Omega_2} \\
&= \frac{M_1^2 - M_2^2}{2\Omega_1\Omega_2}\left(\frac{\Omega_1^2}{M_1^2} + \frac{\Omega_2^2}{M_2^2}\right) \\
&= \frac{M_1^2 - M_2^2}{M_1 M_2}
\end{aligned}
$$

the absolute value of which is also minimized when the ratio M_1/M_2 is the closest to 1.

Due to the coupling strength difference, we have $M_2 \gg M_1$ in our experiment, which means,

$$
\left|\frac{\Delta\delta}{\Omega_R}\right| \approx \frac{M_2}{M_1}
$$

In order to keep the resonance stable within the linewidth of the Raman resonance, i.e. Ω_R, we need to maintain a relative stability of $\Delta\delta$, therefore relative stability of the laser power to better than M_1/M_2.

7.3   STIRAP

An alternative method often used to create and prepare the internal states of ultracold molecule is stimulated Raman adiabatic passage (STIRAP) [36]. Compared to Raman transition, which uses detuning from the excited state to reduce scattering during the transfer, STIRAP relies on a superposition between the initial and final state as a dark state to achieve the same goal. The dark
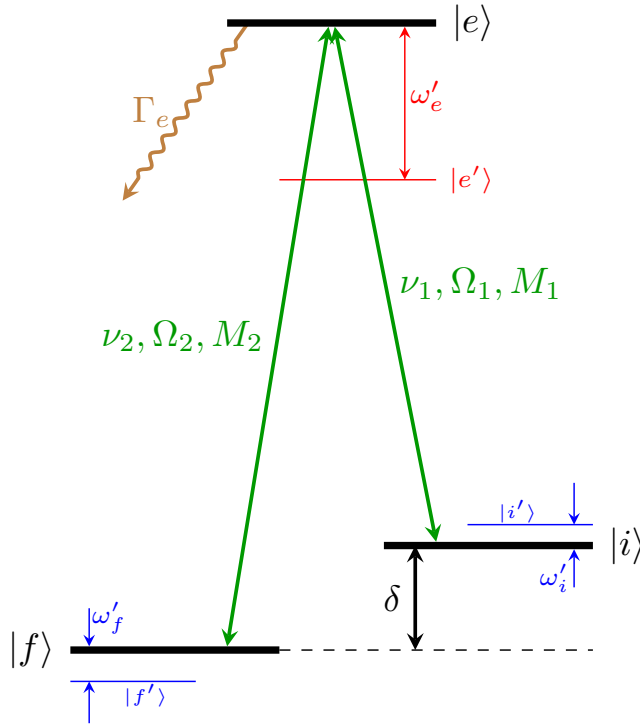
Figure 7.3: Generic model for a real STIRAP similar to Fig. 7.1. Differences are that the two beams are now on resonant with $|e\rangle$ and the Ω_1 and Ω_2 now represent the maximum single photon Rabi frequency during the STIRAP pulse for the two beams.

state in STIRAP is created due to a destructive interference of transition from the initial and final state to the excited state.

Similar to Raman transfer, STIRAP in an ideal three-level system can achieve full coherent transfer with arbitrarily small scattering probability when given unlimited time and power budget. However, in reality, states and coupling that exist outside the ideal three-level system always cause a nonzero probability of scattering loss (Fig. 7.3). In this section, we will apply the approach we took for Raman transition to STIRAP. We will then compare the loss caused by different practical limitations and discuss which approach should be taken under certain circumstance.

7.3.1 STIRAP for Ideal Three-Level System

During STIRAP, the system approximately remains in a dark state $|D(t)\rangle$

$$|D(t)\rangle = c_i(t)|i\rangle + c_f(t)|f\rangle$$

Since this state does not couple to the excited state, we have,

$$0 = \langle e|\mathbf{d} \cdot \mathbf{E}|D(t)\rangle$$

$$= c_i(t)\langle e|\mathbf{d} \cdot \mathbf{E}|i\rangle + c_f(t)\langle e|\mathbf{d} \cdot \mathbf{E}|f\rangle$$

$$= c_i(t)\Omega_1(t) + c_f(t)\Omega_2(t)$$

or

$$|D(t)\rangle = \frac{\Omega_2(t)|i\rangle - \Omega_1(t)|f\rangle}{\sqrt{\Omega_1^2(t) + \Omega_2^2(t)}}$$

In order to estimate the scattering rate, we use the fact that the wavefunction amplitude in the final state c_f is the integral of the excited state amplitude c_e and the down leg Rabi frequency Ω_2, i.e.,[*]

$$c_f(t) = \int_0^t \frac{i\Omega_2(t)}{2} c_e(t')dt'$$

---

[*]This equation and the lower bound on scattering probability applies generically to all two photon transfer process including Raman π pulse. The equation we used in section 7.2 is a refinement on this limit.

For a complete transfer of length T, we have $c_f(0) = 0$ and $c_f(T) = 1$, therefore,

$$\int_0^T \Omega_2(t) c_e(t) \mathrm{d}t = -2\mathrm{i}$$

Since Ω_2 is the upper bound of $|\Omega_2(t)|$ we have,

$$\left| \int_0^T c_e(t) \mathrm{d}t \right| \geqslant \frac{2}{\Omega_2}$$

The total scattering probability is,

$$\begin{aligned}
p_{s0} &= \int_0^T \Gamma_e |c_e^2(t)| \mathrm{d}t \\
&\geqslant \frac{\Gamma_e}{T} \left| \int_0^T c_e(t) \mathrm{d}t \right|^2 \\
&\geqslant \frac{4\Gamma_e}{\Omega_2^2 T}
\end{aligned}$$

From similar argument, we also have,

$$p_{s0} \geqslant \frac{4\Gamma_e}{\Omega_1^2 T}$$

which is the same as the previous result for a three-level STIRAP system where $\Omega_1 = \Omega_2$. In the generic case, these give us a lower bound on the scattering probability,

$$\min\left(p_{s0}\right) = \frac{4\Gamma_e}{\min\left(\Omega_1^2, \Omega_2^2\right) T}$$

whereas the full scattering is larger than this lower bound by a pulse shape dependent small constant factor. It is also easy to verify that this result agrees with the scattering probability for a optimal three-level Raman π with similar single photon Rabi frequency and pulse time. This confirms that without additional constraint from the real system or the experimental setup, neither Raman transfer or STIRAP offers a significant advantage over the other. As we will see in the following sections, other effects in the system can favor one approach over the other one.

7.3.2 Additional Initial and Final States

Similar to Raman transition (section 7.2.1), the additional initial and final states causes potential leakage out of the three-level system. This limits the minimum time of the transfer in a way similar to that of Raman transition.

7.3.3 Additional Excited States

For additional excited states that are farther away than the single photon Rabi frequency Ω_1 and Ω_2, the contribution to the coherent transfer is minimum. However, these states can still contribute to scattering during the transfer.

Excited state will only contribute significantly to the scattering if it causes scattering from the dark state, which happens if $\Omega_1(t)/\Omega_2(t) \neq \Omega'_1(t)/\Omega'_2(t)$, where $\Omega'_1(t)$ and $\Omega'_2(t)$ are the time dependent single photon Rabi frequencies coupling $|e'\rangle$ to $|i\rangle$ and $|f\rangle$ respectively. As discussed in section 7.2.2.2, this does not happen for excited state with the same vibrational and electronic states when the initial and final spin and rotational states are identical. Similar to Ω_1 and Ω_2, we can also define $\Omega'_1 \equiv \max\left(\Omega'_1(t)\right)$ and $\Omega'_2 \equiv \max\left(\Omega'_2(t)\right)$. Since $\Omega'_1(t)(\Omega'_2(t))$ and $\Omega_1(t)(\Omega_2(t))$ are generated from the same beam, we have $\Omega'_1(t) \propto \Omega_1(t)(\Omega'_2(t) \propto \Omega_2(t))$ and the condition can also be equivalently expressed as $\Omega_1/\Omega_2 \neq \Omega'_1/\Omega'_2$.

More quantitatively, the Rabi frequency coupling the dark state $|D(t)\rangle$ to the excited state $|e'\rangle$ is,

$$
\begin{aligned}
\Omega'(t) =& \langle e'|\mathbf{d}\cdot\mathbf{E}|D(t)\rangle \\
=& \frac{\Omega_2(t)\Omega'_1(t) - \Omega_1(t)\Omega'_2(t)}{\sqrt{\Omega_1^2(t) + \Omega_2^2(t)}} \\
=& \frac{\Omega_1(t)\Omega_2(t)}{\sqrt{\Omega_1^2(t) + \Omega_2^2(t)}}\left(\frac{\Omega'_1}{\Omega_1} - \frac{\Omega'_2}{\Omega_2}\right)
\end{aligned}
$$

The addtional scattering caused by this is,

$$
\begin{aligned}
p'_s =& \int_0^T \frac{\Gamma'_e\Omega'^2(t)}{4\omega_e'^2}\mathrm{d}t \\
=& \frac{\Gamma'_e}{4\omega_e'^2}\left(\frac{\Omega'_1}{\Omega_1} - \frac{\Omega'_2}{\Omega_2}\right)^2\int_0^T \frac{\Omega_1^2(t)\Omega_2^2(t)}{\Omega_1^2(t) + \Omega_2^2(t)}\mathrm{d}t \\
=& C'\frac{\Gamma'_e T}{4\omega_e'^2}\left(\frac{\Omega'_1}{\Omega_1} - \frac{\Omega'_2}{\Omega_2}\right)^2\frac{\Omega_1^2\Omega_2^2}{\Omega_1^2 + \Omega_2^2}
\end{aligned}
$$

which has the form of an off-resonance scattering probability. C' is a dimensionless number depending only on the pulse shape defined as

$$C' \equiv \frac{\Omega_1^2 + \Omega_2^2}{\Omega_1^2 \Omega_2^2 T} \int_0^T \frac{\Omega_1^2(t)\Omega_2^2(t)\mathrm{d}t}{\Omega_1^2(t) + \Omega_2^2(t)}$$

It is worth noting that although there aren't two different cases similar to the discussion for Raman transition in section 7.2.2 due to the lack of detuning in STIRAP, the difference between excited states with different spacings may still play an important role when comparing Raman transition to STIRAP. This is discussed breifly at the end of section 7.3.5.1.

7.3.4   Cross Coupling Between Light Addressing Initial and Final States

As is the case for Raman transition (section 7.2.3), the coupling of each beam on the other initial or final state can cause increased scattering. The total scattering probability caused by the cross coupling is [*],

$$
\begin{aligned}
p_s'' &= \int_0^T \frac{\Gamma_e \Omega_1^2(t)}{4M_1^2} \frac{M_2^2}{\delta^2} \left| c_f(t) \right|^2 + \frac{\Gamma_e \Omega_2^2(t)}{4M_2^2} \frac{M_1^2}{\delta^2} \left| c_i(t) \right|^2 \mathrm{d}t \\
&= \frac{\Gamma_e}{4\delta^2} \int_0^T \frac{M_2^2}{M_1^2} \frac{\Omega_1^4(t)}{\Omega_1^2(t) + \Omega_2^2(t)} + \frac{M_1^2}{M_2^2} \frac{\Omega_2^4(t)}{\Omega_1^2(t) + \Omega_2^2(t)} \mathrm{d}t \\
&= \frac{\Gamma_e T}{4\delta^2} \left(C_1'' \frac{M_2^2}{M_1^2} \frac{\Omega_1^4}{\Omega_1^2 + \Omega_2^2} + C_2'' \frac{M_1^2}{M_2^2} \frac{\Omega_2^4}{\Omega_1^2 + \Omega_2^2} \right)
\end{aligned}
$$

---

[*]Here we are making the same assumption of identical matrix elements for the two beams as the one we made for Raman transition in section 7.2.3.

where C_1'' and C_2'' are two dimentionless numbers depending only on the pulse shape defined as,

$$C_i'' \equiv \frac{\Omega_1^2 + \Omega_2^2}{\Omega_i^4 T} \int_0^T \frac{\Omega_i^4(t)\mathrm{d}t}{\Omega_1^2(t) + \Omega_2^2(t)}$$

7.3.5   RAMAN TRANSFER VERSUS STIRAP

As one may expect, the scattering probability and the efficiency of a STIRAP transfer depends on the precise pulse shape used. While it may be possible to construct a STIRAP pulse shape with significantly different constant values, we will focus our discussion on more traditional shapes and assume $C_1'' \approx C_2'' \approx C' \approx 1$.

We will compare the scattering probability during STIRAP to that of Raman π pulse in two limiting case depending on whether the contribution from the additional excited or ground state are more significant.

7.3.5.1   MORE SIGNIFICANT CONTRIBUTION FROM ADDITIONAL EXCITED STATE

This is the case where excited state separation ω_e' is significantly smaller compared to the ground state separation δ. By choosing an optimal pulse time, the minimum scattering probability for the

STIRAP is,

$$
\begin{aligned}
p_s^{\text{STIRAP}} &\approx 2\sqrt{\frac{4\Gamma_e}{\min\left(\Omega_1^2, \Omega_2^2\right)}\frac{\Gamma_e'}{4\omega_e'^2}\left(\frac{\Omega_1'}{\Omega_1} - \frac{\Omega_2'}{\Omega_2}\right)^2 \frac{\Omega_1^2\Omega_2^2}{\Omega_1^2 + \Omega_2^2}} \\
&= \frac{\sqrt{\Gamma_e\Gamma_e'}}{\omega_e'}\left|\frac{\Omega_1'}{\Omega_1} - \frac{\Omega_2'}{\Omega_2}\right|\frac{2\max\left(\Omega_1, \Omega_2\right)}{\sqrt{\Omega_1^2 + \Omega_2^2}} \\
&\geqslant \frac{\sqrt{\Gamma_e\Gamma_e'}}{\omega_e'}\left|\frac{\Omega_1'}{\Omega_1} - \frac{\Omega_2'}{\Omega_2}\right|
\end{aligned}
$$

For Raman π pulse,

$$
\begin{aligned}
p_s^{\text{Raman}} &= \frac{\pi\Gamma}{2\Omega_R} \\
&= \frac{\pi}{2}\frac{\Gamma_e\left(\Omega_1^2 + \Omega_2^2\right)}{4\Delta_{\max}^2}\frac{2\Delta_{\max}}{\Omega_1\Omega_2} \\
&= \frac{\pi\Gamma_e}{4\Delta_{\max}}\frac{\left(\Omega_1^2 + \Omega_2^2\right)}{\Omega_1\Omega_2} \\
&\geqslant \frac{\pi\Gamma_e}{2\Delta_{\max}}
\end{aligned}
$$

The last inequality for both take the equal sign when $\Omega_1 = \Omega_2$. Comparing the result and note that $\Delta_{\max}$ is a fraction of ω_e', we see that the two scales similarly to the excited state spacing. However, given that in the common cases we have $\Delta_{\max} < \omega_e'$ and $|\Omega_1'/\Omega_1 - \Omega_2'/\Omega_2| < 1$ using STIRAP can potentially reduce the total scattering in this case.

Note that the discussion above implicitly assumes that the relevant ω_e' is the same for Raman transition and STIRAP. However, as we saw in section 7.3.3 and 7.2.2.2, this may not be the case for hyperfine and rotational structure in the excited state when the initial and final states have different

spin states. The ω'_e for STIRAP in this case is the hyperfine or rotational splitting and may be significantly smaller compared to the ω'_e for Raman transition, which is the vibrational state spacing. As a result, STIRAP may not be as favorable compared to Raman anymore. The best option in this case would require more in-depth comparison of the different effects and will not be discussed here in more detail since it is not relevant in our experiment.

7.3.5.2 More Significant Contribution from Additional Ground State

With the assumption of $C''_1 \approx C''_2 \approx 1$ the scattering due to cross coupling for STIRAP is now,

$$
\begin{aligned}
p''_s &= \frac{\Gamma_e T}{4\delta^2} \left(\frac{M_2^2}{M_1^2} \frac{\Omega_1^4}{\Omega_1^2 + \Omega_2^2} + \frac{M_1^2}{M_2^2} \frac{\Omega_2^4}{\Omega_1^2 + \Omega_2^2} \right) \\
&\geqslant \frac{\Gamma_e T}{2\delta^2} \left(\Omega_1^2 + \Omega_2^2 \right) \frac{M_1^2 M_2^2}{\left(M_1^2 + M_2^2 \right)^2}
\end{aligned}
$$

and the minimum is taken when $M_2/M_1 = \Omega_2/\Omega_1{}^*$ The minimum total scattering rate for STIRAP is therefore,

$$
\begin{aligned}
p_s^{\mathrm{STIRAP}} &\approx 2 \sqrt{ \frac{4\Gamma_e}{\min\left(\Omega_1^2, \Omega_2^2\right)} \frac{\Gamma_e}{2\delta^2} \left(\Omega_1^2 + \Omega_2^2 \right) \frac{M_1^2 M_2^2}{\left(M_1^2 + M_2^2 \right)^2} } \\
&= 2\sqrt{2} \frac{\Gamma_e}{\delta} \frac{M_1 M_2}{M_1^2 + M_2^2} \frac{\sqrt{\Omega_1^2 + \Omega_2^2}}{\min\left(\Omega_1, \Omega_2\right)} \\
&= 2\sqrt{2} \frac{\Gamma_e}{\delta} \frac{\max\left(M_1, M_2\right)}{\sqrt{M_1^2 + M_2^2}} \approx 2\sqrt{2} \frac{\Gamma_e}{\delta}
\end{aligned}
$$

---

*Same as Raman transition.

For Raman transition

$$p_s^{\text{Raman}} = \frac{\pi\Gamma}{2\Omega_R}$$
$$= \frac{\pi\Gamma_e}{2\Delta} \frac{M_1^2 + M_2^2}{M_1 M_2}$$
$$\approx \frac{\pi\Gamma_e}{2\Delta} \frac{\max(M_1, M_2)}{\min(M_1, M_2)}$$

we can see that when the single photon Rabi frequency is changed to minimize cross coupling scattering, the Raman transition can be more strongly affected by the matrix element imbalance. However, if the Raman transition can use a detuning

$$\Delta > \frac{\max(M_1, M_2)}{\min(M_1, M_2)} \delta$$

then the scattering probability for a Raman transition can be made smaller than that of STIRAP.

7.3.5.3 CONCLUSION

In our experiment, we have an initial and final state separation of $< 1\,\text{GHz}$ and an matrix element ratio of < 30. This means that as long as we can use a single photon detuning of more than $\approx 30\,\text{GHz}$, the total scattering probability for Raman transition will be smaller than that of STIRAP. Since this detuning can be achieved easily, a Raman π pulse should be preferred in our experiment.

The comparison so far has been focused on the scattering probability from the Raman or STI-

RAP beams. There are also a few other more technical reasons we preferred Raman versus STIRAP in our experiment.

1. We use the tweezer beam as the Raman beam for transfer in order to reduce scattering from external sources (section 6.2). Doing this for STIRAP while optimizing the pulse shape for transfer is more challenging.

2. In additional to scattering, the additional excited and ground state also causes a power, and therefore time, dependent light shift. A STIRAP in the presence of these shifts must vary the frequency of the two beams in additional to the power in order to maintain the dark state. This is also technically challenging to do.

As a summary, for two photon transfer to a weakly bound molecular state, it is likely that Raman transition is the preferred technique. However, for transfering to a deeply bound molecular state, which is where STIRAP is used in previous experiments, STIRAP can have an advantage over Raman transition.

7.4   States Selection

From section 7.2 we see that the transfer efficiency is directly related to the excited state linewidth, the maximum usuable detuning and the matrix elements ratio (M_1/M_2). In this section, we will discuss how these, as well as other technical constraints affects the choices of states we use for the Raman transfer.

7.4.1   Initial Atomic State

The choice of initial state can affect the transfer efficiency by changing the matrix element M_1 and therefore the matrix elements ratio. Since for most choices of the atomic and molecular states we
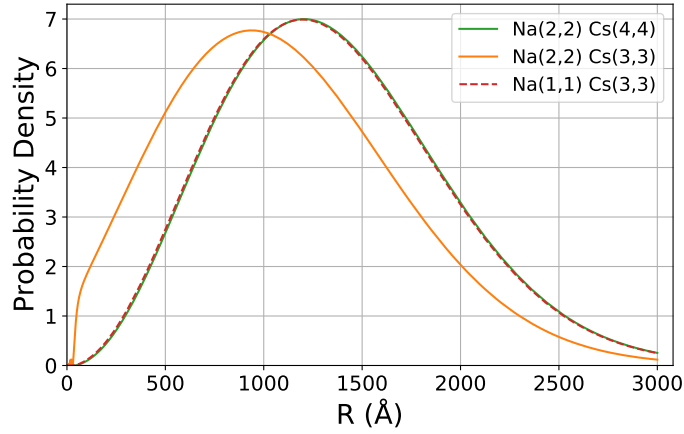
Figure 7.4: Enhancement of short range wavefunction. The large scattering length for the $\mathrm{Na}(2,2), \mathrm{Cs}(3,3)$ state creates an interaction shift comparable to the axial trapping frequency. This causes a significant change in the relative wavefunction especially at short intranuclear distance (R). Compared to other spin states with weaker interaction, the wavefunction at short distance $(R < 100$ Å$)$ is significantly enhanced.

have $M_1 < M_2$, we would like to choose an atomic initial state with the largest M_1 possible. Unlike the selection of final state (section 7.4.3) maximizing M_1 can improve the matrix element ratio as well as shortening the transfer time to decrease sensitivity to technical noise at the same time.

As discussed in section 5.3.3, M_1 is only sensitive to the wavefunction at a short inter-atomic distance that is comparable to the size of the molecule. Therefore, states with a large wavefunction value at short inter-atomic distance should generally have a larger M_1. In additional to the confinement potential and the motional state of the atoms, this is also affected by the interaction between the atoms. A strong interaction, either attractive or repulse, can significantly change the relative motional wavefunction of the atoms. This effect can be seen in Fig. 7.4 and is especially significant for the $|\mathrm{Na}(2,2), \mathrm{Cs}(3,3)\rangle$ state when the interaction energy scale is comparable to that of the motional energy as seen in section 4.3.2.
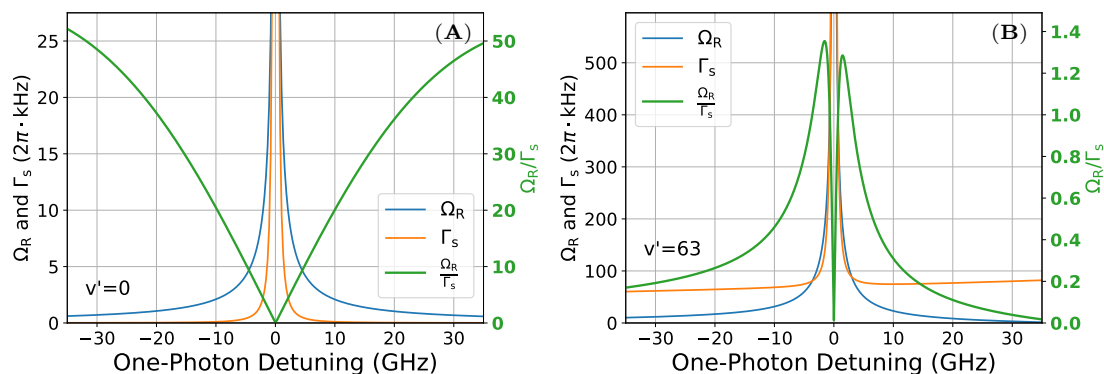
Figure 7.5: Comparison between using a weakly bound and a deeply bound excited state as intermediate state for the Raman transition. The (A) deeply bound excited state ($v' = 0$) has a smaller Raman Rabi frequency'(Ω_R) compared to the (B) weakly bound excited state ($v' = 63$) at a given detuning. However, the lower scattering rate (Γ_s) allows a much larger Δ_{max}, which results in a larger Raman Rabi frequency to scattering rate ratio.

7.4.2 Excited State

Based on theory calculation, most of the molecular excited states have a linewidth Γ'_e very similar to that of the Cesium D lines between $2\pi \times 5$ MHz to $2\pi \times 10$ MHz due to optical decay process. States above the Cesium $6^2P_{1/2}$ state, however, could non-radiatively decay to the Cs $6^2P_{1/2}$ and Na $3^2S_{1/2}$ states via pre-dissociation which significantly increases the linewidth and should be avoided.

The other factor that affects excited state selection is the maximum detuning. Due to larger FCF with the ground atomic and weakly bound molecular state, previous attempt at Raman spectroscopy typically use an excited state closed to the dissociative threshold as the intermediate state [37, 38]. However, the smaller inter-state spacing and the smaller detuning from the atomic excited state means that these state have a relatively small Δ_{max} and therefore a lower coherent transfer efficiency. On the other hand, a deeply bound excited state has a significantly higher Δ_{max} and is the preferred choice for coherent Raman transfer.

In the experiment, we use numerical simulation to calculate the Raman transfer efficiency for any given Raman beam wavelength. Fig. 7.5 shows the result near a deeply bound and weakly bound excited state. Despite having a lower Raman Rabi frequency, the deeply bound state has significantly higher transfer efficiency and is used as the intermediate state for coherent Raman transfer in our experiment.

7.4.3   Final Molecular State

In additional to the scattering and light shift considertions discussed above, the transition can also be affected by external magnetic field. We minimize the effect of magnetic field noise on the transition by using molcular and atomic states that are in the same molecular potential, i.e. molecular bound state in the potential that asymptote to the atomic state. For weakly bound molecular state, i.e. binding energy smaller than or comparable to the hyperfine energy scale, this ensures that the atomic and molecular states has maximally overlapping spin state and therefore a small differential Zeeman shift that can affect the Raman resonance frequency.

Because of the weak coupling between the atomic and molecular states, the Raman transition has a relatively low Rabi frequency. This also means a longer transfer time over which the Raman lasers must remain coherent. In order to lower the requirement on our Raman and tweezer laser, we select the first bound state, i.e. smallest binding energy, as the final molecular state. This ensures the maximum Raman Rabi frequency. Additionally, the typical binding energy for these states are $< 1\,\mathrm{GHz}$ which is a frequency difference that can be generated using AOM's so that the coherence between the two beams is greatly improved.

7.5 Raman Transfer Results

7.5.1 Scaling of Raman Transition Parameters

7.6 Summary and Outlook

(outlook:)

Since the final state is mainly selected based on technical considerations, there are other choices that can potentially improve the transfer efficiency. As an exmple, states with larger binding energies can have weaker coupling to the excited state therefore reducing the matrix elements ratio. Doing so would likely require locking two lasers with a coherence time longer than a few milliseconds.

A

Computer Control Hardware Specification

In this appendex we list the specification of the important hardware used in our computer control

system. See section 1.3 for the integration of these hardware into the system.

A.1 FPGA

We use the ZC702 evaluation board (part number EK-Z7-ZC702-G). The CPU has a maximum clock speed of 666.667 MHz and supports the VFPv3 and NEON extension for floating point and SIMD instructions. The FPGA is configured to run at 100 MHz which determines the highest timing resolution of 10 ns in our experiment.

A.2 DDS

A.3 NI DAQ Card

A.4 USRP

Full Raman Sideband Cooling Sequence

Each Raman pulse in the cooling sequence is followed immediately by an optical pumping pulse. The full parameters for the Raman pulses, including the cooling "axis", the sideband "order (Δn)", the cooling frequency "δ'", the carrier $(\Delta n = 0)$ frequency "δ'_0", the pulse "duration", the pulse strength in "Ω_0", and the beam of which a non-uniform "power ramp" is applied, are listed in 6 groups below. The applied cooling frequency, δ', is the two-photon detuning given relative to the

zero-field $F = 1$ and $F = 2$ hyperfine splitting of $1.7716261288(10)$ GHz [2]. Due to the Stark shifts of the Raman beams, the carrier transition, δ_0', varies with the power of the Raman beams. δ_0' is given also relative to the zero-field hyperfine splitting. The strength of the pulses given in Ω_0 determines the two-photon Rabi frequency, $\Omega_{n,\Delta n} = \Omega_0 \langle n|e^{i\vec{k}\cdot\vec{r}}|n+\Delta n\rangle$. We adopt the convention that a π-pulse between state n and $n + \Delta n$ requires a duration $\pi/\Omega_{n,\Delta n}$. The difference between δ' and δ_0' gives the motional sideband frequency, δ. Many Raman pulses include a "power ramp" with a Blackman envelope [12] to minimize off-resonant excitations. Because each Raman pulse is a product of two spatial- and temporal-overlapped laser beams, the "power ramp" is applied only to the beam that has the smaller light shift (we label the beam by the corresponding F number) while the other beam has a square-pulse shape. For a Raman pulse with a power ramp, the Rabi frequency gives the arithmetic mean over the duration of the pulse.

Group 1

This group is repeated 4 times.

Axis	Δn	δ' (MHz)	δ'_0 (MHz)	Duration (μs)	Ω_0 (kHz)	Power ramp
x	-2	19.625	18.649	44.1	$2\pi \times 23$	F1
y	-2	19.615	18.648	28.6	$2\pi \times 35$	F1
x	-1	19.130	18.649	36.9	$2\pi \times 23$	F1
y	-1	19.615	18.648	24.0	$2\pi \times 35$	F1

Group 2

This group is repeated 5 times.

Axis	Δn	δ' (MHz)	δ'_0 (MHz)	Duration (μs)	Ω_0 (kHz)	Power ramp
z	-5	19.030	18.605	81.5	$2\pi \times 16$	F2
x	-2	19.625	18.649	44.1	$2\pi \times 23$	F1
z	-4	18.940	18.605	76.3	$2\pi \times 16$	F2
y	-2	19.615	18.648	28.6	$2\pi \times 35$	F1
z	-5	19.030	18.605	81.5	$2\pi \times 16$	F2
x	-1	19.130	18.649	36.9	$2\pi \times 23$	F1
z	-4	18.940	18.605	76.3	$2\pi \times 16$	F2
y	-1	19.130	18.648	24.0	$2\pi \times 35$	F1

Group 3

This group is repeated 6 times.

Axis	Δn	δ' (MHz)	δ'_0 (MHz)	Duration (µs)	Ω_0 (kHz)	Power ramp
z	-4	18.940	18.605	76.3	$2\pi \times 16$	F2
x	-2	19.625	18.649	44.1	$2\pi \times 23$	F1
z	-3	18.858	18.605	70.2	$2\pi \times 16$	F2
y	-2	19.615	18.648	28.6	$2\pi \times 35$	F1
z	-4	18.940	18.605	76.3	$2\pi \times 16$	F2
x	-1	19.130	18.649	36.9	$2\pi \times 23$	F1
z	-3	18.858	18.605	70.2	$2\pi \times 16$	F2
y	-1	19.130	18.648	24.0	$2\pi \times 35$	F1

Group 4

This group is repeated 7 times.

Axis	Δn	δ' (MHz)	δ'_0 (MHz)	Duration (μs)	Ω_0 (kHz)	Power ramp
z	-3	18.858	18.605	70.2	$2\pi \times 16$	F2
x	-2	19.625	18.649	44.1	$2\pi \times 23$	F1
z	-2	18.773	18.605	62.7	$2\pi \times 16$	F2
y	-2	19.615	18.648	28.6	$2\pi \times 35$	F1
z	-3	18.858	18.605	70.2	$2\pi \times 16$	F2
x	-1	19.130	18.649	36.9	$2\pi \times 23$	F1
z	-2	18.773	18.605	62.7	$2\pi \times 16$	F2
y	-1	19.130	18.648	24.0	$2\pi \times 35$	F1

Group 5

This group is repeated 10 times.

Axis	Δn	δ' (MHz)	δ'_0 (MHz)	Duration (µs)	Ω_0 (kHz)	Power ramp
z	-2	18.773	18.605	62.7	$2\pi \times 16$	F2
x	-1	19.130	18.649	36.9	$2\pi \times 23$	F1
z	-1	18.685	18.605	52.5	$2\pi \times 16$	F2
y	-1	19.130	18.648	24.0	$2\pi \times 35$	F1
z	-2	18.773	18.605	62.7	$2\pi \times 16$	F2
x	-1	19.130	18.649	70.0	$2\pi \times 23$	F1
z	-1	18.685	18.605	52.5	$2\pi \times 16$	F2
y	-1	19.130	18.648	46.0	$2\pi \times 35$	F1

Group 6

This group is repeated 30 times.

Axis	Δn	δ' (MHz)	δ'_0 (MHz)	Duration (µs)	Ω_0 (kHz)	Power ramp
z	-1	18.683	18.605	78.7	$2\pi \times 11$	F2
z	-1	18.683	18.605	135.0	$2\pi \times 11$	F2
z	-1	18.685	18.605	78.7	$2\pi \times 11$	F2
x	-1	19.130	18.649	36.9	$2\pi \times 23$	F1
y	-1	19.130	18.648	24.0	$2\pi \times 35$	F1
z	-1	18.685	18.605	78.7	$2\pi \times 11$	F2
z	-1	18.685	18.605	135.0	$2\pi \times 11$	F2
z	-1	18.685	18.605	78.7	$2\pi \times 11$	F2
x	-1	19.130	18.649	70.0	$2\pi \times 23$	F1
y	-1	19.130	18.648	46.0	$2\pi \times 35$	F1

References

[1] K.-K. Ni, S. Ospelkaus, M. H. G. de Miranda, A. Pe'er, B. Neyenhuis, J. J. Zirbel, S. Kotochigova, P. S. Julienne, D. S. Jin, and J. Ye, "A High Phase-Space-Density Gas of Polar Molecules." Science **322**(5899), 231–235 (2008).

[2] D. A. Steck, "Sodium D Line Data," (2019).

[3] N. R. Hutzler, L. R. Liu, Y. Yu, and K.-K. Ni, "Eliminating Light Shifts for Single Atom Trapping," New Journal of Physics **19**(2), 023,007 (2017).

[4] D. Wineland, C. Monroe, W. Itano, D. Leibfried, B. King, and D. Meekhof, "Experimental Issues in Coherent Quantum-State Manipulation of Trapped Atomic Ions," J. Res. Natl. Inst. Stand. Technol. **103**(3), 259 (1998).

[5] C. Monroe, D. M. Meekhof, B. E. King, S. R. Jefferts, W. M. Itano, D. J. Wineland, and P. Gould, "Resolved-Sideband Raman Cooling of a Bound Atom to the 3D Zero-Point Energy," Physical Review Letters **75**(22), 4011–4014 (1995).

[6] M. Gröbner, P. Weinmann, E. Kirilov, and H.-C. Nägerl, "Degenerate Raman Sideband Cooling of $^{39}\mathrm{K}$," Physical Review A **95**(3), 033,412 (2017).

[7] D. M. Meekhof, C. Monroe, B. E. King, W. M. Itano, and D. J. Wineland, "Generation of Nonclassical Motional States of a Trapped Atom," Physical Review Letters **76**(11), 1796–1799 (1996).

[8] A. M. Kaufman, B. J. Lester, and C. A. Regal, "Cooling a Single Atom in an Optical Tweezer to Its Quantum Ground State," Physical Review X **2**(4), 041,014 (2012).

[9] J. D. Thompson, T. G. Tiecke, A. S. Zibrov, V. Vuletić, and M. D. Lukin, "Coherence and Raman Sideband Cooling of a Single Atom in an Optical Tweezer," Physical Review Letters **110**(13), 133,001 (2013). 1209.3028.

[10] D. J. Wineland and W. M. Itano, "Laser Cooling of Atoms," Physical Review A **20**(4), 1521–1540 (1979).

[11] L. R. Liu, J. D. Hood, Y. Yu, J. T. Zhang, K. Wang, Y.-W. Lin, T. Rosenband, and K.-K. Ni, "Molecular Assembly of Ground State Cooled Single Atoms," Physical Review X **9**(2), 021,039 (2019). 1902.03935.

[12] M. Kasevich and S. Chu, "Laser Cooling below a Photon Recoil with Three-Level Atoms," Physical Review Letters **69**(12), 1741–1744 (1992).

[13] J. Dalibard, Y. Castin, and K. Mølmer, "Wave-Function Approach to Dissipative Processes in Quantum Optics," Physical Review Letters **68**(5), 580–583 (1992).

[14] R. Grimm, M. Weidemüller, and Y. B. Ovchinnikov, "Optical Dipole Traps for Neutral Atoms," Adv. At. Mol. Opt. Phys. **42**, 95–170 (2000).

[15] G. Colzi, G. Durastante, E. Fava, S. Serafini, G. Lamporesi, and G. Ferrari, "Sub-Doppler Cooling of Sodium Atoms in Gray Molasses," Physical Review A **93**(2), 1–6 (2016).

[16] T. Busch, B.-G. Englert, K. Rza\.zewski, and M. Wilkens, "Two Cold Atoms in a Harmonic Trap," Found. Phys. **28**(4), 549–559 (1998).

[17] E. L. Bolda, E. Tiesinga, and P. S. Julienne, "Effective-Scattering-Length Model of Ultracold Atomic Collisions and Feshbach Resonances in Tight Harmonic Traps," Physical Review A **66**(1), 013,403 (2002).

[18] D. Blume and C. H. Greene, "Fermi Pseudopotential Approximation: Two Particles under External Confinement," Physical Review A **65**(4), 043,613 (2002).

[19] Z. Idziaszek and T. Calarco, "Analytical Solutions for the Dynamics of Two Trapped Interacting Ultracold Atoms," Physical Review A **74**(2), 022,712 (2006).

[20] J. F. Bertelsen and K. Mølmer, "Association of Heteronuclear Molecules in a Harmonic Oscillator Well," Physical Review A **76**(4), 043,615 (2007).

[21] F. Deuretzbacher, K. Plassmeier, D. Pfannkuche, F. Werner, C. Ospelkaus, S. Ospelkaus, K. Sengstock, and K. Bongs, "Heteronuclear Molecules in an Optical Lattice: Theory and Experiment," Physical Review A **77**(3), 032,726 (2008).

[22] B. Gao, "Quantum-Defect Theory of Atomic Collisions and Molecular Vibration Spectra," Physical Review A **58**(5), 4222–4225 (1998).

[23] B. Gao, "Angular-Momentum-Insensitive Quantum-Defect Theory for Diatomic Systems," Physical Review A **64**(1), 010,701 (2001).

[24] B. Gao, "General Form of the Quantum-Defect Theory for $\ensuremath{-}1/{r}{\ensuremath{\alpha}}$ Type of Potentials with $\ensuremath{\alpha}>2$," Physical Review A **78**(1), 012,702 (2008).

[25] O. Docenko, M. Tamanis, J. Zaharova, R. Ferber, A. Pashov, H. Knöckel, and E. Tiemann, "The Coupling of the X 1Σ + and a 3Σ + States of the Atom Pair Na + Cs and Modelling Cold Collisions," J. Phys. B At. Mol. Opt. Phys. **39**(19), S929–S943 (2006).

[26] B. H. McGuyer, M. McDonald, G. Z. Iwata, M. G. Tarallo, A. T. Grier, F. Apfelbeck, and T. Zelevinsky, "High-Precision Spectroscopy of Ultracold Molecules in an Optical Lattice," New Journal of Physics **17**(5), 055,004 (2015).

[27] S. G. Porsev and A. Derevianko, "Accurate Relativistic Many-Body Calculations of van Der Waals Coefficients C8 and C10 for Alkali-Metal Dimers," The Journal of Chemical Physics **119**(2), 844–850 (2003).

[28] J. D. Hood, Y. Yu, Y.-W. Lin, J. T. Zhang, K. Wang, L. R. Liu, B. Gao, and K.-K. Ni, "Multichannel Interactions of Two Atoms in an Optical Tweezer," Physical Review Research **2**(2), 023,108 (2020).

[29] B. Bransden, C. Joachain, and T. Plivier, *Physics of Atoms and Molecules*, Pearson Education, 2nd ed. (Prentice Hall, 2003).

[30] B. P. Straughan, ed., *Spectroscopy. Vol. 3: ...*, no. 122 in Science Paperbacks, 2nd ed. (Chapman and Hall, London, 1976).

[31] J. Zaharova, M. Tamanis, R. Ferber, A. N. Drozdova, E. A. Pazyuk, and A. V. Stolyarov, "Solution of the Fully-Mixed-State Problem: Direct Deperturbation Analysis of the A Σ + 1 – b Π 3 Complex in a NaCs Dimer," Physical Review A **79**(1), 012,508 (2009).

[32] A. Grochola, P. Kowalczyk, J. Szczepkowski, W. Jastrzebski, A. Wakim, P. Zabawa, and N. P. Bigelow, "Spin-Forbidden c 3Σ + $(\Omega = 1) \leftarrow$ X 1Σ + Transition in NaCs: Investigation of the $\Omega = 1$ State in Hot and Cold Environments," Physical Review A **84**(1), 012,507 (2011).

[33] A. Grochola, P. Kowalczyk, and W. Jastrzebski, "Investigation of the B1Π State in NaCs by Polarisation Labelling Spectroscopy," Chem. Phys. Lett. **497**(1-3), 22–25 (2010).

[34] J. L. Dunham, "The Energy Levels of a Rotating Vibrator," Physical Review **41**(6), 721–731 (1932).

[35] L. R. Liu, J. D. Hood, Y. Yu, J. T. Zhang, N. R. Hutzler, T. Rosenband, and K.-K. Ni, "Building One Molecule from a Reservoir of Two Atoms," Science **360**(6391), 900–903 (2018).

[36] N. V. Vitanov, M. Fleischhauer, B. W. Shore, and K. Bergmann, "Coherent Manipulation of Atoms Molecules By Sequential Laser Pulses," in *Advances In Atomic, Molecular, and Optical Physics*, B. Bederson and H. Walther, eds., vol. 46, pp. 55–190 (Academic Press, 2001).

[37] R. Wynar, R. S. Freeland, D. J. Han, C. Ryu, and D. J. Heinzen, "Molecules in a Bose-Einstein Condensate," Science **287**(5455), 1016–1019 (2000).

[38] T. Rom, T. Best, O. Mandel, A. Widera, M. Greiner, T. W. Hänsch, and I. Bloch, "State Selective Production of Molecules in Optical Lattices," Physical Review Letters **93**(7), 073,002 (2004).